

CORROSION ASSESSMENT IN REBARS OF REINFORCED CONCRETE STRUCTURES USING EQUIVALENT PARAMETERS EXTRACTED FROM PIEZO-PATCHES

TALAKOKULA VISALAKSHI



**DEPARTMENT OF CIVIL ENGINEERING
INDIAN INSTITUTE OF TECHNOLOGY DELHI**

October 2014

**CORROSION ASSESSMENT IN REBARS OF
REINFORCED CONCRETE STRUCTURES
USING EQUIVALENT PARAMETERS
EXTRACTED FROM PIEZO-PATCHES**

by

TALAKOKULA VISALAKSHI

Department of Civil Engineering

Submitted

in fulfilment of the requirements of the degree of

Doctor of Philosophy

to the



Indian Institute of Technology Delhi

October 2014

CERTIFICATE

This is to certify that the thesis entitled, "**CORROSION ASSESSMENT IN REBARS OF REINFORCED CONCRETE STRUCTURES USING EQUIVALENT PARAMETERS EXTRACTED FROM PIEZO-PATCHES**" submitted by Ms. Talakokula Visalakshi to Indian Institute of Technology Delhi, for the award of the degree of the **Doctor of Philosophy** is a record of bonafide research work carried out by her. She worked under our supervision for the submission of this thesis, which to the best of our knowledge has reached the requisite standard.

The research reports and the results presented in this thesis have not been submitted in parts or in full to any other University or Institute for the award of any degree or diploma.

(Dr. Suresh Bhalla)

Associate Professor

Department of Civil Engineering

Indian Institute of Technology Delhi

Delhi

(Prof. Ashok Gupta)

Professor

Department of Civil Engineering

Indian Institute of Technology

ACKNOWLEDGEMENTS

First and foremost, I would like to extend my sincere thanks and gratitude towards my supervisors, Dr Suresh Bhalla and Prof. Ashok Gupta. It is no overstatement to say that without the consistent guidance, tutelage, support, unparalleled knowledge, and encouragement of my supervisors, this thesis would never have existed. They truly exemplify the role of advisors. I am forever grateful for their kindness and contributions, not only towards my research, but towards my professional growth as well.

Thanks are also due to Prof B. Bhattacharjee, who had given valuable suggestions during the initial days of my research, which helped me a lot. I am grateful to my committee members Prof. K. S. Rao, Dr. A. K. Darpe and Dr G. S. Benipal, who provided useful suggestion and valuable advice regarding my research. Thanks to all the Civil Engineering faculty and other staff members, special thanks to Mr. Lal Singh, Mr. Vinod Sharma, Mr. Mansukh Sureen and other technicians for their keen support in my work. I am extremely grateful to the staff of Smart Structures and Dynamics Laboratory (SSDL), departmental and central libraries for providing books, journals etc., which made this research work possible.

Thanks are also due to Dr. R. J.Ball, Dr. G. L. Pesce, Prof. C. R. Bowen and Dr. K. Paine of University of Bath, UK and R. Kurchania of MANIT, Bhopal, India.

A special thanks goes to almighty God and my parents, Last but not least, I wish to express my gratitude to my family, and in particular to my supportive and patient husband Basa Kiran Kumar and to my lovely son Basa Chandraneil .

Talakokula Visalakshi

ABSTRACT

Reinforced concrete (RC) is an economical, versatile and successful construction material as it can be moulded to a variety of shapes and finishes. In most cases, it is durable and strong, performing well throughout its service life. However, in some cases, it does not perform adequately due to various reasons, one of which is the corrosion of the embedded steel bars used as reinforcement. Concrete provides an almost ideal environment for protecting the embedded steel from corrosion due to the passive film surrounding the steel rebars. However, the breakdown of this passive film, either due to chloride attack or due to carbonation, results in the corrosion of rebars. Thus rebar corrosion is one of the main causes of damage and premature failure of the RC structures worldwide, causing enormous costs for inspection, maintenance, restoration and replacement. Therefore, early detection of corrosion and timely remedial action on the affected portion can facilitate an optimum utilization of the structure, imparting longevity to it.

A large number of investigations have been conducted on the problems related to the deterioration of RC structures due to the corrosion of steel rebars. Usually, the condition of the structure is monitored by visual inspection and remedial measures are resorted to only when the condition becomes very serious. In order to prevent the deterioration levels reaching severe dimensions, it is desirable to monitor the condition of strategic structures right from the construction stage using structural health monitoring (SHM) techniques. The recent advent of the electro-mechanical impedance (EMI) technique for SHM has provided a new paradigm to the maintenance engineers to diagnose the onset of the damage at the incipient stage itself. The EMI technique utilizes the piezoelectric ceramic patches (PZT) as collocated actuators-sensors and employ ultrasonic vibrations (typically in 30-400 kHz

range) to acquire the characteristic ‘signature’ of the structure, which contains vital information governing the phenomenological nature of the structure, and can signal the onset of structural damages.

Although the EMI technique is well established for damage detection and quantification of various civil and aerospace structures, limited studies have been reported for its application in corrosion detection. This thesis presents a new corrosion assessment models based on the equivalent parameters extracted from the impedance spectrum of concrete-rebar system using the EMI technique via the PZT sensors. The corrosion assessment models are developed based on an accelerated corrosion study carried out on RC specimens covering both chloride and carbonation induced corrosion using PZT sensors that are surface bonded on rebars as well as using piezo-composite concrete vibration sensor (CVS) embedded in concrete near rebar. This is the first ever research reporting such extensive studies on the application of the equivalent parameters for corrosion assessment of rebars embedded in concrete.

Proof-of-concept experiments were performed extending up to 120 days to detect chloride induced corrosion using surface bonded PZT patches as well as CVS. Accelerated corrosion tests were performed in order to obtain the data in a reasonable time frame for a laboratory-based study. Firstly, the equivalent structural parameters were extracted from the admittance spectra of the PZT patches surface bonded to bare rebars for chloride induced corrosion and an empirical model was developed for correlating the actual mass and stiffness with the equivalent mass and stiffness identified by the PZT sensor. Further, the empirical model was extended to the RC specimens to determine the corrosion rates and identify various phases of corrosion using the PZT patches both surface bonded to rebar as well as CVS embedded near rebar. The experimental results indicate that the equivalent parameters and the

developed model are effective in detecting and quantifying the rebar corrosion in a realistic manner.

The research was further extended to the second type of corrosion i.e., carbonation induced corrosion through accelerated carbonation tests conducted on RC cylinders (with rebars surface bonded with PZT patches) in a carbonation chamber for a period of 250 days. The carbonation corrosion assessment models developed were correlated with the progress of depth of carbonation. Imaging techniques such as scanning electron microscopic images and Raman spectroscopy were also used to further establish the onset of carbonation corrosion and correlate with the signal provided by the PZT patches.

Finally, to enhance the efficiency of the proposed model in real life application, the empirical model developed for chloride induced corrosion under accelerated tests was validated by comparing the corrosion rates of RC specimens exposed to natural environment for a period of 420 days. In addition, the influence of mineral admixture, namely fly ash, on the corrosion performance of steel is also investigated non-destructively using the developed model.

The corrosion assessment models developed are empirical and non-destructive in nature. The stiffness model is used to determine the severity of corrosion damage during various phases and the mass model for determining the corrosion rates for both chloride induced and carbonation induced corrosion. These models can be used for non-destructive corrosion monitoring of RC structures in real life with no “a-prior” information regarding the structure and with no modelling required. It is expected that this research will provide a new alternative experimental technique to the researchers and diagnostic engineers working in the field of rebar corrosion.

TABLE OF CONTENTS

CERTIFICATE	ii
ACKNOWLEDGEMENTS	iii
ABSTRACT.....	iv
TABLE OF CONTENTS	vii
LIST OF FIGURES	xi
LIST OF TABLES	xvi
LIST OF ACRONYMNS	xvii
LIST OF SYMBOLS	xix
CHAPTER 1 : INTRODUCTION.....	1
1.1 Background	1
1.2 Research Hypothesis	3
1.3 Research Objectives and Scope	3
1.4 Research Significance	5
1.5 Outline of Thesis.....	6
CHAPTER 2 : LITERATURE REVIEW	8
2.1 Introduction.....	8
2.2 The Corrosion Process	9
2.3 Rebar Corrosion in Reinforced Concrete Structures	10
2.3.1 Chloride Induced Corrosion in Concrete	11
2.3.2 Carbonation Induced Corrosion in Concrete	13
2.4 Techniques for Corrosion Detection.....	14
2.4.1 Electro-Chemical Techniques	15
2.4.1.1 Potential Measurement Technique	15
2.4.1.2 Linear Polarization Resistance Technique	21
2.4.1.3 Alternating current Impedance Spectroscopy Technique	24
2.4.2 Gravimetric Measurement Technique	24

2.4.3 Corrosion Monitoring Using Sensors	25
2.5 Impedance Based Structural Health Monitoring.....	27
2.5.1 Piezoelectric Materials	27
2.5.2 Geometric Details of PZT patches	29
2.5.3 Diverse Applications of Piezoelectric Materials	29
2.6 Electro-Mechanical Impedance Technique Using PZT patches	30
2.6.1 Physical Principles	30
2.6.2 Frequency Range Selection	34
2.6.3 Effect of Temperature	35
2.6.4 Sensing Range and Optimal Placement of PZT Patches	36
2.6.5 Excitation Voltage and Signature Acquisition	36
2.6.6 Instrumentation and Other Considerations	36
2.7 Major Research in Electro-Mechanical Impedance Technique Since 1990's	37
2.8 Limitations in Application of PZT patches for Structural Health Monitoring	41
2.9 Summary: Critical Points of Review	42
2.10 Research Objectives	44
CHAPTER 3 : DIAGNOSIS OF CHLORIDE INDUCED CORROSION IN BARE STEEL REBARS	47
3.1 Introduction.....	47
3.2 Mechanical Impedance of Structures	47
3.3 Mechanical Impedance of PZT patches	50
3.4 Details of Accelerated Corrosion Study	51
3.5 Damage Quantification	56
3.5.1 Root Mean Square Deviation	56
3.5.2 Signature Assurance Criteria	57
3.5.3 Waveform Chain Code Technique	57
3.5.4 Adaptive Template Matching	58
3.6 Analysis of Structural Mechanical Impedance Extracted From Admittance Signature ...	60
3.7 Concluding Remarks	73

CHAPTER 4 :DEVELOPMENT OF CORROSION ASSESSMENT MODEL FOR REBARS EMBEDDED IN REINFORCED CONCRETE STRUCTURES	74
4.1 Introduction.....	74
4.2 Rebar Corrosion in Reinforced Concrete Structures	74
4.3 Specimen Preparation	77
4.4 Accelerated Corrosion Exposure on Conductance Signatures	78
4.5 Analysis Based on Equivalent Structural Parameters	85
4.6 Calibration of Extracted Equivalent Parameters	90
4.6.1 Development of Equivalent stiffness model	90
4.6.2 Development of Equivalent Mass Model for Corrosion Rates	94
4.7 Concluding Remarks.....	97
CHAPTER 5 : COMPARISON OF CORROSION ASSESSMENT CAPABILITY OF SURFACE BONDED AND EMBEDDED PIEZO SENSORS	99
5.1 Introduction.....	99
5.2 Advantages of Embedded Sensors.....	100
5.3 Configuration and Application of Embedded PZT Sensors	98
5.4 Experimental Details and Results	102
5.4.1 Comparison of Conductance Signatures	103
5.4.2 Comparison of Root Mean Square Deviation Index	105
5.4.3 Comparison of Equivalent Stiffness Parameters	106
5.5 Concluding Remarks.....	111
CHAPTER 6 : MONITORING AND ASSESSMENT OF CARBONATION INDUCED CORROSION IN REINFORCED CONCRETE STRUCTURES	113
6.1 Introduction.....	113
6.2 Accelerated Carbonation Study: Experimental Procedure	114
6.3 Analysis of Results	118
6.4 Correlation With Microscopic Image Analysis and Raman Analysis	123
6.5 Validation of Corrosion Rate Prediction Model	128
6.5 Concluding Remarks.....	129

6.6 Acknowledgements	129
CHAPTER 7 : APPLICATIONS OF THE PROPOSED CORROSION ASSESSMENT MODEL ON FLY ASH BLENDED CONCRETE AND ON NATURALLY CORRODED SPECIMENS	130
7.1 Introduction.....	130
7.2 Proof-of-Concept Validation 1: Corrosion Assessment in Fly Ash Blended Concrete ..	130
7.2.1 Details of Fly Ash utilized	134
7.2.2 Experimental Details (Concrete and Fly Ash)	136
7.2.3 Microstructural Analysis.....	138
7.2.4 Corrosion Assessment in Fly Ash Blended Concrete Using the Derived Model	139
7.3 Proof-of-Concept Validation 2: Corrosion Assessment in Naturally Corroded Specimens	142
7.4 Concluding Remarks	143
CHAPTER 8 : CONCLUSIONS AND RECOMENDATIONS.....	144
8.1 Introduction	144
8.2 Research Conclusions and Contributions	144
8.3 Limitations	147
8.4 Recommendations for Future	148
PUBLICATIONS BASED ON THIS RESEARCH.....	149
REFERENCES.....	153
CIRRICULAM VITAE	176

LIST OF FIGURES

	Page
Fig. 2.1 Tutti's model of corrosion initiation and propagation (Tutti, 1982)	12
Fig. 2.2 Schematic diagram of carbon dioxide ingress	14
Fig. 2.3 Schematic diagram of potential measurement set up	16
Fig. 2.4 Schematic diagram of LPR measurement set up	22
Fig. 2.5 Direct and converse effect of piezoelectric materials	28
Fig. 2.6 Typical Polarization observed in piezoceramic materials (Cook, 2001) (a) Unpolarized Ceramic Material (b) Polarized Ceramic Material	28
Fig. 2.7 Geometric details of a typical PZT patch (PI Ceramics 2012)	29
Fig. 2.8 Bonded PZT patch and its interaction (a) Modelling of PZT-structure interaction (1D) (Bhalla and Soh, 2003) (b) A PZT patch bonded to the host structure (2D)	31
Fig. 3.1 Experimental set up (a) Rebar specimen prepared for bonding PZT (b) Experimental set up	52
Fig. 3.2 Experimental admittance signature (a) Conductance (G) (b) Susceptance	53
Fig. 3.3 Accelerating corrosion set up	53
Fig. 3.4 Condition of specimens (a) Pristine specimen (b) Corroded specimen	54
Fig. 3.5 Variation of the conductance signature due to accelerated corrosion Exposure. (a) Specimen 1 (b) Specimen 2 (c) Specimen 3	55
Fig. 3.6 Variation of RMSD (a) Specimen 1 (b) Specimen 2 (c) Specimen 3	59
Fig. 3.7 Kelvin-Voigt system (Hixon 1998)	62
Fig. 3.8 Comparison of experimental plots x and y with those of identified system (a) Specimen 1 (b) Specimen 2 (c) Specimen 3	63
Fig. 3.9 Variation of 'y' with ω^I (a) Specimen 1 (b) Specimen 2 (c) Specimen 3	64

Fig. 3.10	Variation of extracted system parameters (stiffness and damping) (a) Specimen 1 (b) Specimen 2 (c) Specimen 3	66
Fig. 3.11	Equivalent System parameters (a) Equivalent system (series combination of spring-damper and mass) (b) x vs f of specimen1 (c) y vs f of specimen 1	68
Fig. 3.12	Variation of extracted system parameters (a) Equivalent damping of specimen 1 and 2 (b) Equivalent stiffness of specimen 1and 2 (c) Equivalent mass of specimen 1 and 2	69
Fig. 3.13	Variation of actual mass loss with accelerated corrosion exposure (a) Specimen 1 (b) Specimen 2	70
Fig. 3.14	Correlation between loss of actual mass with PZT identified mass loss (a) Specimen 1 (b) Specimen 2	72
Fig. 4.1	The anodic and cathodic reactions for corroding steel (Broomfield, 2007)	75
Fig. 4.2	Relative volume of iron and its oxides (Mansfield, 1981)	76
Fig. 4.3	Specimen preparation and data acquisition setup	79
Fig. 4.4	Baseline conductance signatures of PZT patches embedded in RC Specimens (a) Specimen 1 (b) Specimen 2 (c) Specimen 3 (d) Specimen 4	79
Fig. 4.5	Condition of reinforced concrete specimen 5 (a) Pristine state (b)After 45 days (c) After split open at 45 days	81
Fig. 4.6	Condition of specimen 1 after 120 days of accelerated corrosion (a) Cracked specimen (b) Cracked specimen after splitting (c) Corroded bar removed from specimen	81
Fig. 4.7	Variation of conductance signatures of specimen 1 during accelerated corrosion process	83
Fig. 4.8	Variation of conductance signatures of specimen 2 during accelerated corrosion process	83
Fig. 4.9	Variation of conductance signatures of specimen 3 during accelerated corrosion process	84
Fig. 4.10	Variation of conductance signatures of specimen 4 during accelerated corrosion process	84

Fig. 4.11	Variation of root mean square deviation index during accelerated corrosion process (a) Specimen 1 (b) Specimen 2 (c) Specimen 3 (d) Specimen 4	86
Fig. 4.12	Identified system (Parallel combination of spring-mass-damper)	86
Fig. 4.13	Experimental and analytical plots of ‘x’ and ‘y’ for baseline signatures (a) Specimen 1 (b) Specimen 2 (c) Specimen 3 (d) Specimen 4	88
Fig. 4.14	Variation of PZT identified stiffness with corrosion progression (a) Specimen 1 (b) Specimen 2 (c) Specimen 3 (d) Specimen 4	89
Fig. 4.15	Variation of PZT identified masswith corrosion progress (a) Specimen 1 (b) Specimen 2 (c) Specimen 3 (d) Specimen 4	90
Fig. 4.16	Variation of $\Delta k/k$ (PZT identified stiffness loss) with corrosion progress (a) Specimen 1 (b) Specimen 2 (c) Specimen 3 (d) Specimen 4	93
Fig. 4.17	Variation of ($\Delta m/m$) PZT identified mass loss with corrosion progress (a) Specimen 1 (b) Specimen 2 (c) Specimen 3 (d) Specimen 4	95
Fig. 5.1	Reinforced concrete cube specimen with embedded sensor	99
Fig. 5.2	Comparison of conductance signature of surface bonded piezo sensors and embedded concrete vibration sensor	103
Fig. 5.3	Variation of conductance signature of concrete vibration sensor during accelerated corrosion exposure	104
Fig. 5.4	Comparison of variation in conductance signature due to corrosion exposure of concrete vibration sensor and surface bonded piezo sensor	105
Fig. 5.5	Comparison of variation in root mean square deviation of concrete vibration sensor and surface bonded piezo sensor	106
Fig. 5.6	Experimental and analytical plots of embedded concrete vibration sensor (a) Variation of ‘x’(b) Variation of ‘y’	107
Fig. 5.7	Variation of identified stiffness with corrosion progress (a) Concrete vibration sensor (b) Surface bonded piezo sensor	107
Fig. 5.8	Comparison of variation of equivalent stiffness of concrete vibration sensor and Surface bonded piezo sensor	108

Fig. 5.9	Variation of $\Delta k/k$ with corrosion progress of concrete vibration sensor	108
Fig. 5.10	Comparison of variation in $\Delta k/k$ of concrete vibration sensor and surface bonded piezo sensor (a) Specimen 1 (b) Specimen 2 (c) Specimen 3	109
Fig. 5.11	Comparison of various phases of corrosion (a) Using concrete vibration sensor (b) Using surface bonded piezo sensor	111
Fig. 6.1	Carbonation chamber	116
Fig. 6.2	Baseline conductance signatures of PZT patch embedded in reinforced concrete cylindrical specimens	116
Fig. 6.3	Phenolphthalein (a) Schematic diagram representing the depths of carbonation (b) 5 mm slice sprayed with phenophthalein indicator	117
Fig. 6.4	Variation of conductance signatures during accelerated corrosion process (a) Specimen 1 (b) Specimen 2 (c) Specimen 3	118
Fig. 6.5	Variation of Variation of root mean square deviation index during accelerated corrosion process (a) Specimen 1 (b) Specimen 2 (c) Specimen 3	119
Fig. 6.6	Comparison of experimental plots of x and y with those of identified system for typical specimen 1	120
Fig. 6.7	Variation of equivalent stiffness during accelerated corrosion process (a) Specimen 1 (b) Specimen 2 (c) Specimen 3	120
Fig. 6.8	Variation of $\Delta k/k$ during accelerated corrosion process (a) Specimen 1 (b) Specimen 2 (c) Specimen 3	122
Fig. 6.9	Correlation of equivalent structural parameter values with scanning electron microscope and optical images	125
Fig. 6.10	SEM image showing fine interlaced silicate needles forming dense structure	126
Fig. 6.11	Raman spectrum of α -hematite (Fe_2O_3) oxide layer on steel rebar (Inset shows optical image of polished section and location of analysis)	127
Fig. 7.1	XRD spectrum of fly ash	136

Fig. 7.2	SEM images at different magnifications (20 μm and 2 μm) (a) Fly Ash (b) Ordinary Portland cement grade 43.	139
Fig. 7.3	Condition of the specimens (a) 0% FA specimen showing significant cracks (b) 25% FA specimen without any corrosion signs (c) 50% FA specimen showing rust on the surface	141
Fig. 7.4	RC specimen under natural environment (a) Specimen before split open (b) Condition of rebar after removing from the cube	143

LIST OF TABLES

		Page
Table 2.1	ASTM criteria for corrosion of steel in concrete for different standard reference electrodes	17
Table 4.1	Concrete mix design details	78
Table 4.2	Equivalent structural parameters identified by PZT patch in healthy state	87
Table 4.3	Initial and final stiffness (actual and PZT identified)	91
Table 4.4	Relation between non-dimensional actual stiffness loss and PZT identified stiffness loss	92
Table 4.5	Relation between non-dimensional actual mass loss and PZT identified mass loss	96
Table 4.6	Corrosion rate values (without considering Λ_m)	96
Table 4.7	Comparison of actual and PZT identified corrosion current rates (considering Λ_m)	97
Table 6.1	Details of specimens	115
Table 6.2	Phenolphthalein test results	117
Table 6.3	Corrosion rate values (without considering Λ_m)	123
Table 6.4	Corrosion rate values (considering Λ_m)	128
Table 7.1	Mix proportions for 25% fly ash concrete	137
Table 7.2	Mix proportions for 50% fly ash concrete	137
Table 7.3	Slump details of various fly ash mixes	138
Table 7.4	Corrosion rates of various fly ash mixes	141

LIST OF ACRONYMS

ATM	Adaptive template matching
AC	Alternating current
ASTM	American society for testing and materials
A/C	Anode-to-cathode area
CVS	Concrete vibration sensor
CTD	Cold twisted deformed bars
CDV	Curvature differential values
DC	Direct current
EMI	Electro-mechanical impedance
EIS	Electro-chemical impedance spectroscopy
Z	Electrical impedance
ESP	Equivalent stiffness parameter
FESEM	Field Emission Scanning Electron Microscopy
FBG	Fiber Bragg grating
FCS	Fiber composite sensor
FA	Fly ash
HYD	High yield deformed
LPR	Linear polarization resistance
LCR	Inductance Capacitance and Resistance
MFC	Macro fiber composite
NDE	Non-destructive evaluation
MFC	Macro-fiber composite

OCP	Open circuit potential
OPC	Ordinary Portland cement
PZT	Piezoelectric-ceramic
PFC	Piezoelectric fiber composite
PPC	Portland pozzolana cement
PSC	Portland slag cement
RC	Reinforced concrete
RMS	Root mean square
RMSD	Root mean square deviation
SEM	Scanning electron microscopy
SAC	Signature assurance criteria
SDV	Slope differential values
SHM	Structural health monitoring
SHE	Standard hydrogen electrode
SRPC	Sulphate-resisting Portland cement
SBPS	Surface Bonded Piezo Sensors
TMT	Thermo-mechanically treated
TTMT	Thermex thermo-mechanically treated
IR	Voltage drop through electrolyte
WCC	Waveform chain code
XRD	X-ray diffraction

LIST OF SYMBOLS

B	A constant (unit volts)
R_P	Polarization resistance (in ohms)
E_3	Electric field applied in the direction ‘3’
l	Patch half-length
h	Thickness of patch
S_I	Strain along axis ‘1’
D_3	Electric displacement over the surface of PZT patch
d_{3I}	Piezoelectric strain coefficient
T_I	Axial stress in the patch along the axis ‘1’
$\overline{Y^E}$	Complex Young’s modulus of elasticity of the patch at constant electric field
$\overline{\varepsilon_{33}^T}$	Complex electric permittivity at constant stress
η	Mechanical loss factors of the patch
δ	Dielectric loss factors of the patch
u	Displacement at any point on the patch in direction ‘1’
k	Wave number
ρ	Density
\overline{Y}	Electro-mechanical admittance
Z_a	Short-circuited mechanical impedance of the PZT patch
Z_{xx} and Z_{yy}	Direct impedances
Z_{xy} and Z_{yx}	Cross impedances
$Z_{a,eff}$	Short-circuited effective mechanical impedance of the structure

R	Resistance
X	Reactance
G	Conductance
B	Susceptance
ϕ	Angle
m	Mass
k	Spring constant
c	Damping constant
λ_{kb}	Constant relating the non-dimensional PZT based stiffness loss with actual stiffness loss for bare steel rebars
λ_{mb}	Constant relating the non-dimensional PZT based mass loss with actual mass loss for bare steel rebars
G_i	Conductance of the PZT patch at any stage during the test
G_i^0	Baseline conductance value
i	Frequency index
x	Real components of structural impedance
y	Imaginary components of structural impedance
ω	Angular frequency
m_0	Original mass of the specimen
δm	Loss of mass
λ_k	Constant relating the non-dimensional PZT based stiffness loss with actual stiffness loss for rebars embedded in concrete
λ_m	Constant relating the non-dimensional PZT based mass loss with actual mass loss for rebars embedded in concrete

CHAPTER- 1

INTRODUCTION

1.1 BACKGROUND

Concrete is a versatile, cost effective and easy to handle construction material, widely used next only to water. Its lack of adequate tensile strength is taken care by steel rebars making the combination reinforced concrete (RC). In most cases, RC structures are durable and strong, performing well throughout its service life. However, in some cases, they do not perform adequately due to various reasons and one of the reason being corrosion of steel rebars. In fact, corrosion of the steel rebars has become the major cause of deterioration of RC structures around the world (Hansson et al., 2007; Darek, 2012).

The corrosion of steel rebars embedded in concrete is most frequently the result of the breakdown of the passive film formed due to highly alkaline environment around steel rebars (Moreno et al., 2004). Two conditions can break down the passivating environment surrounding the rebar without attacking the concrete itself, one is the chloride attack and the other is carbonation (Broomfield, 2007). Rebar corrosion is generally accompanied by the loss of rebar cross section and accumulation of corrosion products, which occupy much larger volume than the original steel (Broomfield, 2007), thereby generating tensile stresses, which lead to cracking and spalling of concrete, commonly known as concrete cancer (Dehwah et al., 2002). Over the time, this problem reduces the strength capacity of the affected structure due to the loss of bonding action between steel and concrete, ultimately leading to loss of serviceability. It is reported that, the economic losses and damage caused by the corrosion of steel rebars in RC structures is the largest infrastructure problem faced by the industrialized countries (Broomfield, 2007). As a result, the repair costs constitute a

major part of the current spending on infrastructure. Corrosion consumes considerable portion of the budget of the country by way of either restoration measures or reconstruction. It is estimated that billions of dollars are spent annually on the maintenance and repairs of corroding RC structures in North America alone (Darek, 2012). India loses more than \$40 billion a year, (about 4 per cent of the size of the total economy) due to corrosion in infrastructure and industry segments (Financial Express, 2012). Quality control, maintenance and planning for the restoration of these structures need non-destructive inspections and monitoring techniques that detect the corrosion at an early stage. For detection of corrosion and for determining rebar corrosion rate, several electro-chemical and non-destructive techniques are available. Conventional corrosion detection techniques based on electro-chemical principles consists of potential measurements, alternating current impedance spectroscopy, gravimetric (mass loss) and linear polarization techniques. However these techniques are affected by a number of factors. Hence, there is a need for development of a sensing technique to inspect the structure in real-time (to supplement routine inspections) so that corrosion could be detected and treated before significant cracking develops.

The newest generation of autonomous structural health monitoring (SHM) systems with active sensors can possibly assess the current and the future performance of the structure subjected to corrosion. For this purpose, effective corrosion sensor technology is critical for ensuring safety of RC structures during life time. Several proof-of-concept experiments to detect corrosion using piezoelectric-ceramic (PZT) patches in metallic structures have been reported (Simmers, 2005; Park and Park, 2010; Rathod and Mahapatra, 2011). Extensive analytical and experimental works have been devoted to the detection of rebar corrosion in RC structures using fiber optic sensors also (Fuhr and Huston, 1998; Grattan et al., 2007,

2009; Zheng et al., 2009, 2010, Gao et al., 2011). However, these studies were preliminary in nature and did not provide any solid means of rigorous qualification of corrosion damage after its detection. This thesis is focused towards this goal.

1.2 RESEARCH HYPOTHESIS

Rebar corrosion in RC structures is a worldwide problem, SHM using PZT sensors via electro-mechanical impedance (EMI) technique can provide a new corrosion assessment technique non-destructively without any a-prior information regarding the structure . The equivalent parameters extracted from the admittance signatures of the PZT sensors such as equivalent stiffness parameter and equivalent mass parameter may provide a fairly good idea about the severity of corrosion during various phases and could determine the corrosion rate respectively as they have already proven their competence for bolted steel joints (Bhalla et al., 2012) and concrete (Soh and Bhalla, 2005).

1.3 RESEARCH OBJECTIVES AND SCOPE

Interest of the research community in the corrosion problem has been increasing for several years because of the severe durability problems faced by RC structures due to rebar corrosion. This research aims at developing a new corrosion detection and assessment approach, which can detect corrosion at initial stages before the signs of corrosion such as rust strains appear on the concrete and assess the severity of corrosion at different corrosion phases. The EMI technique has been utilized to develop the corrosion model for both chloride and carbonation induced corrosion of rebars in RC structures. This research encompasses the following specific objectives:

1. To carry out a thorough review of state-of-the-art in corrosion detection and monitoring, as well as SHM using PZT patches especially focussing on the EMI technique and its application.
2. To detect and quantify chloride induced corrosion through accelerated corrosion experiments in
 - a. Bare steel bars via equivalent structural parameters extracted from admittance spectrum of PZT patches surface bonded to the rebar.
 - b. Extend the experimental approach of bare bars to rebars embedded inside the concrete, as in real RC structures.
3. To develop corrosion assessment models for determining the severity of corrosion damage during various phases of chloride induced corrosion and the corrosion rates without the need of actual parameters.
4. To carry out the feasibility of utilizing piezo-composite concrete vibration sensors (CVS) which can be embedded inside the concrete while casting so as to diagnose the structure right from day one and compare its corrosion sensing abilities with the PZT sensors surface bonded to rebar.
5. To develop a similar corrosion assessment model like chloride induced for carbonation induced corrosion in RC structures through accelerated experiments. Correlate the impedance data acquired with micro structural imaging techniques to gain further insight into the changes developed in the microstructure with corrosion and fine tune the developed models.

6. To validate the proposed chloride corrosion assessment model developed under accelerated environment with the naturally corroded specimens and also to investigate the performance of fly ash (FA) blended concrete under corrosive environment.

1.4 RESEARCH SIGNIFICANCE

It is expected that the developed corrosion assessment models using PZT sensors will facilitate more realistic performance prediction of RC structures affected by corrosion over time. PZT patches can facilitate the development of non-obtrusive miniaturized systems with higher resolution, faster response and far greater reliability than the conventional non-destructive evaluation (NDE) techniques. These smart materials possess immense capabilities of damage diagnosis because of their inherent ‘stimulus-response’ and energy transduction capabilities. The PZT patches can be embedded or bonded unobtrusively on locations inaccessible for physical inspection of rebars. Due to self-sensing nature of the PZT patches, the number of sensors required are much less than the rival approach based on separate actuation and sensing. The assessment models are based on the equivalent structural parameters identified from the experimental data alone, thus circumventing any analytical/numerical model as a prerequisite. These models are more realistic and totally non-destructive compared to the conventional corrosion assessment techniques. It is believed that this thesis will make significant contribution to the state-of-the-art of corrosion diagnosis in RC structures as the developed model can determine the corrosion rates non-destructively and can assess the severity of corrosion. The Corrosion assessment based on these models can provide large saving to the society by detecting corrosion in early stages and providing timely remedial measures.

1.5 OUTLINE OF THE THESIS

This thesis has been organized into eight chapters. First chapter covers the background of corrosion of rebars in RC structures, research hypothesis, objectives, scope of the research and its significance. Chapter-2 outlines the literature review consisting of the working principle, applications of the EMI technique for health monitoring and a detailed review of state-of-art of corrosion detection in RC structures. The chapter begins with a brief overview of various conventional techniques for corrosion detection and quantification, their advantages and limitations, followed by the application of EMI technique in damage detection of various civil, mechanical and aerospace structures. Corrosion in metallic structures using the EMI technique is also summarized. The chapter closes with a discussion of the research gaps in the current state-of-the art.

Chapter-3 explores the basics of the occurrence of corrosion of steel rebars in concrete, covers detailed overview of chloride induced corrosion, corrosion mechanism and the reactions associated with it. The preliminary investigation of the EMI technique for corrosion assessment in bare steel bars via PZT patches bonded to the surface of the bar is also covered.

Chapter-4 presents the detailed development of corrosion assessment models for rebars embedded in concrete based on accelerated chloride induced corrosion experiments. The correlation of the developed equivalent stiffness model with the various phases of corrosion and the determination of corrosion rates with the developed equivalent mass model is also presented.

Chapter-5 covers the assessment of corrosion using embedded piezo-composite CVS (embedded near rebar). The main advantages and the limitations using embedded sensor for corrosion detection are deliberated upon.

Chapter-6 presents the diagnosis of carbonation induced corrosion studied by means of accelerated carbonation tests performed for over a period of 250 days. The correlation of the developed equivalent stiffness model with imaging techniques for studying the changes in the microstructure during the carbonation is also discussed.

Chapter-7 presents validation of the proof-of-concept of the corrosion assessment models developed in this research via accelerated tests, through its application on naturally corroded specimen and further extended to FA blended concrete subjected to accelerated corrosion.

Chapter-8 highlights the summary and conclusions of this research. Suggestions for further research are also included in this chapter, followed by a list of publications based on this research, a comprehensive list of references along with author's curriculum vitae.

CHAPTER- 2 **LITERATURE REVIEW**

2.1 INTRODUCTION

Rebar corrosion in RC structures has been widely reported in the literature over the last three decades. It is recognized as the predominant factor that reduces the service life of RC structures exposed to aggressive environment. In most cases, the total mass loss due to corrosion within the structure is trivial, but significant reductions in mechanical strength and fatigue life occurs in the localized corroded region of the rebar, leading to advanced crack growth with enhanced risk of the failure of the structure. Since the structural damage due to localized corrosion pitting is small and the crack growth rates are relatively large, early detection of the corrosion prior to local failure can prevent catastrophic collapse of the structures. The interest in the ability to monitor corrosion in a structure and detect damage at the earliest possible stage is pervasive throughout the civil, mechanical and aerospace engineering communities. A wide range of electro-chemical/non electro-chemical techniques and sensors based techniques have been reported in the literature for the purpose of diagnosing and quantification of the rebar corrosion.

The prime motivations behind the ongoing research on rebar corrosion in RC structures have been elaborately covered in Chapter 1. In this chapter, a thorough review of the literature on corrosion process and its monitoring techniques with emphasis on rebar corrosion is presented. A critical review of the SHM with regard to the EMI technique using PZT patches is also presented, since the aim of this research is to detect and quantify rebar corrosion in RC structures using PZT sensors via the EMI technique.

2.2 THE CORROSION PROCESS

American society for testing and materials (ASTM) terminology defines corrosion as “the chemical or electro-chemical reaction between a material, usually a metal, and its environment, that produces a deterioration of the material and its properties” (ASTM G193, 2012). Since corrosion has an adverse effect on structures, it is important to understand the mechanism and the associated effects. Metals are extracted from the ore through the application of a considerable amount of energy. With time, it reacts with the environment chemically and tends to return to its original lower energy level. Steel, like most metals (except gold and platinum), is thermodynamically unstable under normal atmospheric conditions and tends to revert back to its natural state i.e. iron oxide, or rust by releasing energy, this process is called corrosion. For corrosion to occur, three basic elements are essential. Firstly, there must be at least two metals or two locations on a single metal at different energy levels. Secondly, an electrolyte and finally a metallic connection are required. The absence of any one of these three would inhibit the process of corrosion.

In the electro-chemical corrosion of metals, the 'corroding' metal undergoes oxidation (the anodic reaction), whereas the 'corrosive' chemical species undergoes reduction (the cathodic reaction). Corrosion, is the sum of two half reactions, oxidation and reduction. Both half reactions must simultaneously exist at the same rate to ensure equitable production and consumption of electrons for the electro-chemical reaction to proceed without an external source and to maintain the charge balance (Hansson, 1984). The generic form of the oxidation of a metal (anodic reaction) is:



The most common cathodic or reduction reactions contributing to the corrosion of a metal are:



The possible cathodic reactions depend on the availability of oxygen and on the pH in the vicinity of the metal (Hansson, 1984).

2.3 REBAR CORROSION IN REINFORCED CONCRETE STRUCTURES

The three basic elements that are necessary for the corrosion process (see previous section) to occur are present in RC structures. Firstly, the rebar has many areas at different energy levels. Secondly concrete acts as the electrolyte and finally, metallic connection is provided by the rebar itself. However, the microscopic pores in concrete contain high concentrations of soluble calcium, sodium and potassium oxides, which form hydroxides when combined with water, creating a high alkaline environment of pH 12-13. This high alkalinity enables the formation of the passive layer over the rebar surface (Elsener et al., 2003; Poupard et al., 2006) providing a high degree of protection to the embedded steel rebars against corrosion. In addition, well compacted and properly cured concrete with low water-cement ratio has low permeability, which further minimizes the penetration of corrosion inducing agents such as chloride ions and carbon dioxide. Further, the high resistivity of concrete enables it to restrict the corrosion rate of the rebar by retarding the flow of the electric current. Hence, in a properly designed, constructed and maintained RC structure, there will hardly be any major problem of rebar corrosion during its design life (Broomfield, 2007). Unfortunately, this desirable condition is not always met in practice due to several reasons. Therefore, rebar

corrosion in concrete has become a commonly encountered cause of degradation of the RC structures.

The alkaline environment around the steel rebars protecting the steel is not always maintained, and can be destroyed either by chloride attack or carbonation attack which reduces the pH of the pore solution (Page et al., 1986; Poupart et al., 2006; Page et al., 2000). The four basic mechanisms for transport of these aggressive ions include capillary suction, permeation, diffusion, and migration. The rate at which these ions penetrate to breakdown the passive film is a function of the quality and quantity of the concrete surrounding the reinforcement and the internal and external environments. The time for the chloride ion concentration to reach a critical level for the onset of corrosion is known as the ‘initiation Period’. Once the protective layer around the reinforcement has been removed, corrosion can take place in the presence of moisture and oxygen. The time taken for corrosion to result in sufficient deterioration such that remedial action is required is known as the ‘propagation period’. Different conceptual models are proposed to describe the corrosion process of steel rebar in concrete (Tuutti, 1982; Cady and Wayers, 1983; Francois and Arliguie, 1999). The concept of Initiation and Propagation periods can be illustrated by famous Tuutti’s model (Tuutti, 1982). A schematic representation of Tuutti’s model illustrating the initiation and propagation periods is presented in Fig.2.1.

2.3.1 Chloride Induced Corrosion in Concrete

One of the most common causes for rebar corrosion in RC structures is the presence of chloride ions. They cause localized breakdown of the passive film that initially forms around steel as a result of the alkaline nature of the pore solution in concrete (Montemor et al., 2003

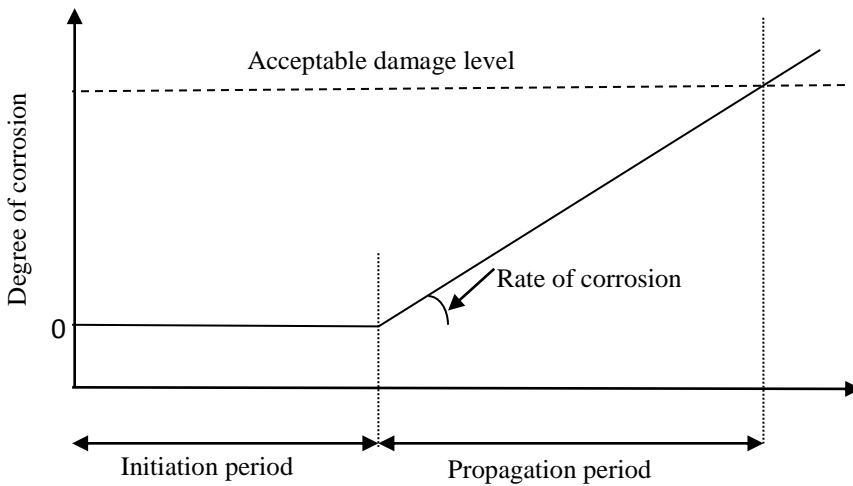


Figure 2.1 Tutti's model of corrosion initiation and propagation (Tutti, 1982)

and Moreno et al., 2004). The main corrosive agents, that is, the chlorides, can ingress into concrete from several sources. The aggressive chloride ions can originate either from the contaminated mixing ingredients (cast into the concrete as part of the ground water/seawater in the mix or contaminated aggregates or due to sea salt spray/direct wetting or deicing salts) in the fresh state or from the surrounding environment in the hardened state (Hussain et al., 1995; Dehwah et al., 2002; Broomfield, 2007). They can be. These chlorides, when diffused into concrete, reduce the alkalinity of the pore solution (from the original pH . 13 to below 7) thereby initiating corrosion.

It has been reported in the past that the corrosion initiation takes place when the chloride concentration at the rebar level reaches a critical level, which is also often referred to as the threshold level (Glass and Buenfeld, 1997; Alonso et al., 1998; Maheswaran and Sanjayan, 2004; Trejo and Monteiro, 2005). Mechanism of breakdown of the passive film was studied by a large number of researchers. Montemor and his co-researchers suggested that the

initiation of passive layer destruction takes place due to the adsorption of Cl^- with simultaneous displacement of O^{2-} from the passive layer. Hoar (1967) found that chloride ions lower the interfacial surface tension, thus weakening the passive film which results in the formation of cracks and flaws. Pradhan (2007) suggested the service life of RC structure exposed to chloride ions consists of two phases, namely the initiation phase and the propagation phase.

2.3.2 Carbonation Induced Corrosion in Concrete

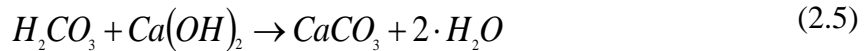
Carbonation is the result of the interaction of carbon dioxide gas in the atmosphere with the alkaline hydroxides in the concrete. Like many other gases, carbon dioxide (CO_2) dissolves in water to form carbonic acid. The carbonic acid does not attack the cement paste, but just neutralizes the alkalies in the pore water, mainly forming calcium carbonate that fills the pores (Parrot, 1987 and Bakker, 1988) as given by following equation



Calcium hydroxide is not the only substance that reacts with CO_2 , the other hydration products and even the residual unhydrated cement compounds also take part into carbonation reactions (Claisse et al., 1997). The formation of calcium carbonate requires three equally important substances: CO_2 , calcium phases (Ca), and water (H_2O). CO_2 is present in the surrounding air, calcium phases mainly calcium hydroxide (Ca(OH)_2) and calcium silicate hydrate (CSH) are present in the concrete, and water is present in the pores of the concrete. The process of carbonation is schematically illustrated in Fig. 2.2. The first reaction in the pores is the formation of carbonic acid (H_2CO_3) can be written as



The carbonic acid then reacts with the calcium phases



Once $Ca(OH)_2$ has been converted, hydrated CSH will liberate CaO which also undergoes carbonation:

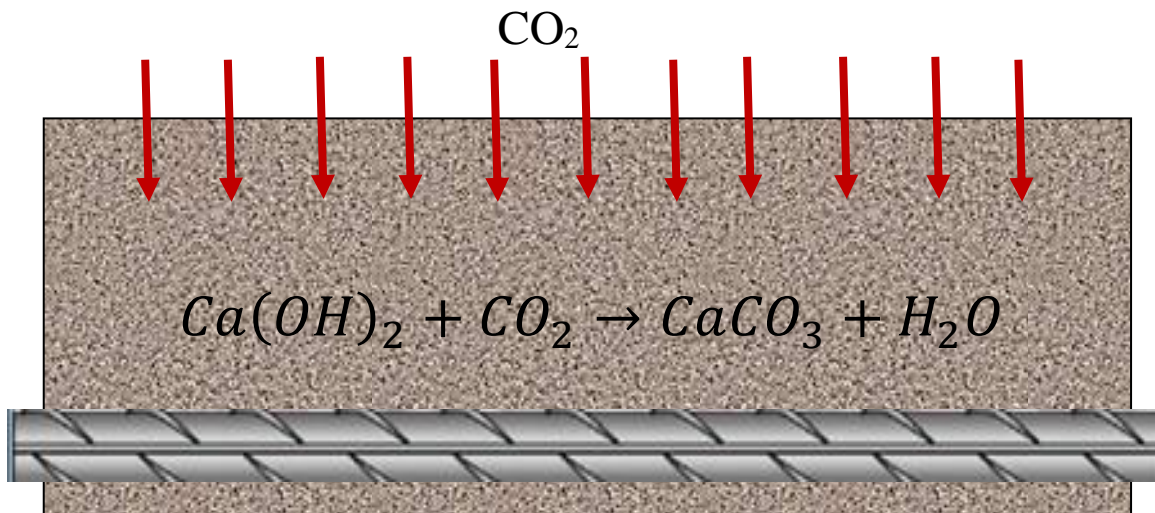


Figure 2.2. Schematic diagram of CO_2 ingress

During the occurrence of these reactions, there will be drastic decrease in the pH value from 12.6 to a value about of 8.0, a critical-value when the passive layer cannot protect the steel (Parrot, 1987) leading to corrosion.

2.4 TECHNIQUES FOR CORROSION DETECTION

Corrosion can cause serious failures, potentially causing irreparable economic losses. The most important step in order to hinder or reduce the extent of such failures is to detect the

corrosion as early as possible and adopt effective preventive measures. To detect and to measure the corrosion rate of rebars in the RC structures, several electro-chemical, destructive and non-destructive techniques are available, which are briefly described below.

2.4.1 Electro-Chemical Techniques

Traditionally, visual observation has been the common practice to detect corrosion. As the rebar corrodes, there are usually signs of rusting, cracking and spalling. However, due to the different degrees of aggressivity of concrete quality and of structural geometry, once the signs of deterioration are seen on the concrete cover (rust, cracking and spalling) it may be too late to prevent the advance of deterioration by repair works. Electro-chemical techniques have emerged as liable means for corrosion detection due to their potential non-destructive character. They are the most widely used techniques for the study of rebar corrosion process in laboratories and on-site applications (Andrade and Alonso, 1996). The commonly used electro-chemical techniques include potential measurement, polarization resistance measurement and electro-chemical impedance measurement. The following sub sections cover a detailed description of each technique.

2.4.1.1 Potential measurement technique

The most popular technique of monitoring reinforcement corrosion is by means of electrode potential measurements. As a corrosion detecting technique, it was first used by Stratful (1957). The application and the interpretation of this technique are described in ASTM C876 (1999). The potential measurements for determining the probability of corrosion in concrete has been extensively described by Flis et al. (1995), Grantham et al. (1997) and Zvica (2001).

The effectiveness of the test was thoroughly studied by Erdogdu et al. (2004). The basic measurement in this technique is the voltage of the electro-chemical cell formed between the embedded steel and a reference electrode (of which potential is constant) which is placed on the concrete surface, as shown in Fig. 2.3. These measurements can be performed on all kinds of real life RC structures. However, the identification of active corrosion of rebars embedded in concrete is delicate and depends on numerous factors related to the material and its environment such as concrete moisture, cement characteristics etc. It is essential to always quote the reference electrode being used for potential measurements.

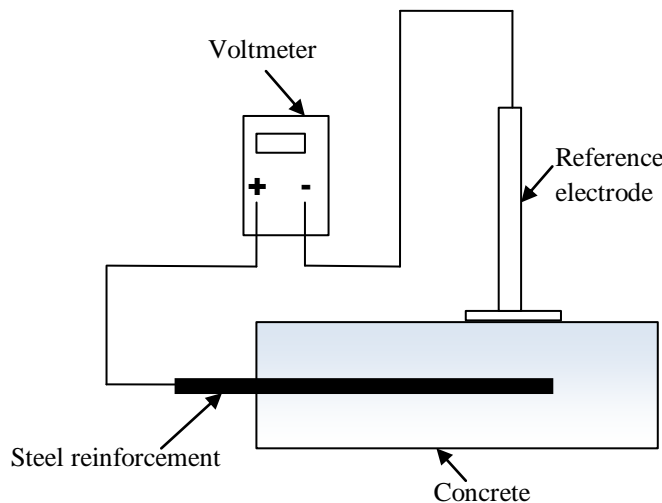


Figure 2.3 Schematic diagram of Potential measurement set

The standard reference electrode or half cell is a simple device, consisting of a piece of metal in a fixed concentration solution of its own ions (such as copper in saturated copper sulphate, silver in silver chloride, etc.). In practice, the most commonly used reference electrodes are Copper- copper sulfate (Cu/CuSO_4), Calomel ($\text{Hg}/\text{Hg}_2\text{Cl}_2$), Silver-silver chloride (Ag/AgCl), with a defined constant and reproducible potential versus the standard hydrogen electrode (SHE). The potential measurement using reference electrode gives an indication of the corrosion risk of the steel. The measurement is linked by empirical comparisons to the

probability of corrosion as listed in Table 2.1 (ASTM C 876, 1999). Several researchers have used the potential measurements for detection of rebar corrosion and contributed to new findings based on their measurements. Alonso et al. (1998) have reported that these values depend on the conductivity of the corrosion products formed and also on the age of concrete

Table 2.1 ASTM criteria for different standard reference electrodes

Potential	Silver/silver chloride	Standard hydrogen electrode	Saturated calomel electrode	Corrosion condition
>-200mV	>-100mV	+120mV	>-80mV	Low (10% risk of corrosion)
-200 to -350mV	-100 to -250mV	+120 to -30mV	-80 to -230mV	Intermediate corrosion risk
<-350mV	<-250mV	-30mV	<-230mV	High (>90% risk of corrosion)
<-500mV	<-400mV	-18-mV	<-380mV	Severe corrosion

Oh et al. (2003) measured the potential value, extent of the corroded areas of steel and determined the threshold free chloride, the total chloride and Cl^-/OH^- ratio in prismatic concrete specimens made with ordinary portland cement (OPC), sulphate-resisting Portland cement (SRPC), OPC blended with FA and OPC blended with slag. Their results showed that concrete made with SRPC exhibited relatively higher negative values of potentials at the same total chloride content as compared to other mixtures, implying greater susceptibility to corrosion.

Sakr (2005) studied the effect of the proportion of tricalcium aluminate (C_3A) on the corrosion of steel embedded in cement specimens. From the results of the potential

measurements along with other techniques, it was found that chloride ions are more aggressive for rebar corrosion than sulphate ions.

Nakamura et al. (2008) reported a practical application of the potential measurements for corrosion assessment on an existing prestressed concrete bridge near the coastline in Japan. Based on experimental observations, they concluded that the most negative potential area on the equipotential contour map corresponds to the point with high chloride content and localized corrosion. They also concluded that the potential gradient is a good indicator to select the position for further destructive tests if there are no signs of corrosion on the concrete surface. They also found that the measured values of the potential fluctuated due to various factors, such as the temperature, the type of reference electrode, and the pre-wetting time. However, the potential gradient pattern remained same for the structure. They further concluded that numerical values of the potential are not particularly suitable for assessing the corrosion risk of the existing concrete structures. The equipotential contour map is more reliable tool for detecting localized corrosion and deciding the position for further destructive tests.

Pradhan and Bhattacharjee (2009) demonstrated that potential measurements are stable indicators of rebar corrosion initiation based on their experiments conducted on RC beams. Their work also reconfirmed that the critical chloride level leading to corrosion initiation is not a unique value and varies with steel type, cement type, and water-cement ratio. Blended cements, i.e., Portland pozzolana cement (PPC) and Portland slag cement (PSC) both exhibited higher chloride tolerance and corrosion initiation period than those exhibited by OPC. Similarly, Tempcore thermo-mechanically treated (TMT) bars resulted in higher values

of chloride tolerance and longer corrosion initiation period than those exhibited by Thermex thermo-mechanically treated (TTMT) and cold twisted deformed bars (CTD).

Ghaz et al. (2009) modelled the potential measurements numerically by solving the Laplace's equation, considering the effect of resistivity, cover thickness, oxygen availability, and anode-to-cathode area (A/C) ratio on the potential mapping. Based on the results, they concluded that in low resistivity concrete, the potential distribution along the surface closely represents the potential distribution at the interface of steel/concrete. As the resistivity of concrete increases, the potential distribution at the surface tends to part noticeably from that of the steel/concrete interface. This difference was more significant at sections close to the transition zone between the anode and the cathode. They also found that with increase in cover thickness, the potential of the surface differed from that of the interface significantly. They further noticed that oxygen concentration in concrete is not a significant factor affecting potential measurement unless concrete is completely deprived of oxygen. A higher average potential value at the surface of concrete implies lower the probability of the corrosion as per ASTM (1999). However, the rate of such corrosion, if occurring locally, was found to be very high. On the other hand, at small values of average potential, the probability of the corrosion is higher, but such corrosion may proceed more uniformly. Accurate detection of localized corrosion, in which A/C ratio is small, may not be feasible with potential measurement method unless supplementary measurements are made.

Even though potential measurement technique is widely used, following points highlights some of its limitations.

1. The numerical value of the measured potential difference between the rebar in concrete and the reference electrode depends on the type of reference electrode used and on the corrosion condition of the rebar in concrete. In addition, potentials of rebar in concrete cannot be measured directly at the interface of steel/concrete due to the presence of the concrete cover (Fig. 2.3) and are thus influenced by voltage drop through electrolyte (IR drop) in the cover, the macrocell current and possibly the junction potentials (Elsener et al., 2003).
2. A simple comparison of the potential data with the ASTM guidelines on rebar corrosion probability could not be worthwhile, as, a more negative reading of potential, which is generally considered to indicate a higher probability of corrosion, may not always be valid as many factors can shift the potential readings towards more positive or negative values (Gu et al., 1996).
3. While carrying out the potential measurements, potential readings should be interpreted in accordance with the resistivity of the system. Otherwise, the results can be misleading, for the same corrosion rate, one can measure different potentials at the surface of concrete, corresponding to different values of resistivity, and thus have more than one probability for the same state of corrosion.

Owing to the above said limitations, The application of potential measurements is restricted to as the first approach for corrosion detection, and needs to be supplemented with other non-destructive testing methods for further diagnosis

2.4.1.2 Linear polarization resistance technique

Linear polarization resistance (LPR) monitoring is an effective electro-chemical technique for measuring rebar corrosion rates. The calculation of the corrosion rate using this technique is based on the relationship between the electro-chemical potential and the current generated between electrically charged electrodes.

The LPR technique (also known as polarization resistance) polarizes the rebar with an electric current and monitors its effect on the reference electrode potential. It is carried out with a sophisticated reference electrode (incorporating an auxiliary electrode) and a variable low voltage direct current (DC) power supply. The reference electrode potential is first measured and then a small current is passed from the auxiliary electrode to the reinforcement. The change in the reference electrode potential is simply related to the corrosion current (Stern and Geary, 1957) by the equation

$$i_{corr} = B/R_P \quad (2.7)$$

where B is a constant (unit volts) and R_P is the polarization resistance (in ohms). In concrete, the value of B is generally regarded within the range between 26mV to 52mV (Andrade et al., 2004). R_P is given by

$$R_P = \frac{\text{Change in potential}}{\text{Applied current}} \quad (2.8)$$

In a conventional LPR test, the perturbation is applied from an auxiliary electrode on the concrete surface as shown in Fig. 2.4. The surface area of steel assumed to be polarized is the area lying below the auxiliary electrode. However, the current flowing from the auxiliary

electrode is unconfined and can spread laterally over an unknown, larger area of steel (Feliu et al., 1989; 1994). This can lead to inaccurate information of the surface area of steel polarized and thus result in an error in the calculation of the corrosion current density, which, in turn, will lead to an inaccurate estimation of the extent of corrosion.

In order to overcome the problem of confining the current to a predetermined area, the use of a second auxiliary guard ring electrode surrounding the inner auxiliary electrode has been developed (Feliu et al., 1988; 1990; 1994; Broomfield et al., 1993 and Sehgal et al., 1992). The principle of this modified set up is that the outer guard ring electrode maintains a confinement current during the LPR measurement, which prevents the perturbation current from the main inner auxiliary electrode spreading beyond a known area.

In order to select an appropriate level for the confinement current, two sensor electrodes are placed between the inner and outer auxiliary electrodes. The potential difference between these sensor electrodes is monitored and a confinement current is selected to maintain this potential difference throughout the LPR measurement (Milliard et al., 2001).

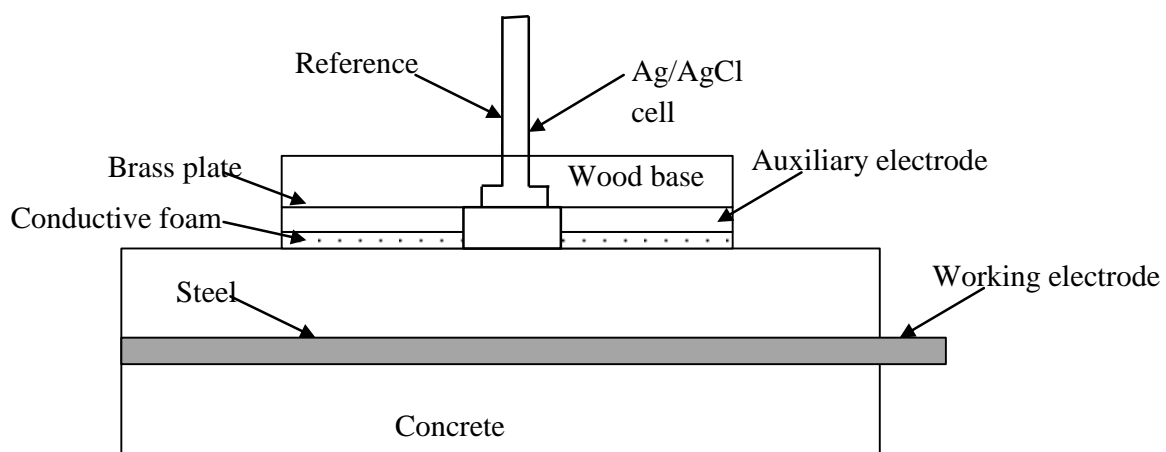


Figure 2.4 Schematic diagram of LPR measurement set up

In concrete, however, the main difficulty in the use of this technique arises from the irregular distribution of the electrical signal applied via the counter electrode of much smaller dimensions than the RC structure under test. Instead of a uniform distribution over the whole metallic system, the electrical signal tends to vanish with increasing distance from the counter electrode location.

To solve this problem, Gonzalez et al. (1991) and Feliu et al. (1998) developed an approach based on a “transmission line” model. They proposed an analytical solution for estimating the R_p and checked their validity by comparing the analytical solution with direct measurements of R_p obtained under conditions projected to achieve a uniform distribution of the signal applied to the reinforcement. Their model demonstrated that the response of a large RC structure to an electrical signal applied via a counter electrode of much smaller dimensions can be based on the response of a transmission line. Two approaches were derived from the model. The first one used the response in current resulting from the application of a potential step to the reinforcement with the aid of a smaller counter electrode, placed on the concrete beam. The second one is based on the decrease of the potential applied in this manner in terms of the distance from the referred counter electrode. The model clearly differentiated between the behaviour of the steel in the passive and the active states. This model has been adopted by a number of researchers as a way to estimate the corrosion rate (Ahmad and Bhattacharjee. 1995).

In spite of sophistications, the LPR measurements pose a number of difficulties in high resistivity media such as those encountered in large concrete structures. Notable amongst

such difficulties are the following, which may even render the in-situ measurement highly erroneous.

1. The high resistance of concrete between the rebar (i.e. working electrode) and the reference electrode, which offers a potential drop commonly referred to as an ohmic drop; must be either compensated externally or eliminated mathematically.
2. The sample being larger compared to the counter electrode, the distribution of the electrical signal applied for polarisation of the rebar is non-uniform throughout the cross-section of the beam.

2.4.1.3 Alternating Current Impedance Spectroscopy Technique

The AC impedance spectroscopy is also known as electro-chemical impedance spectroscopy (EIS). It involves the application of a series of small AC potential with different frequencies to the RC specimen, measuring the responses and analyzing them in the frequency domain. Due to sophistication of the measurement, this technique is more widely used in laboratory studies rather than in field. Further, it is often difficult to interpret and is time consuming in nature. Nevertheless, its use is nowadays a research tool to understand the behaviour and mechanism of the steel/concrete interface and to reveal information of the rebar corrosion kinetics (Gu et al., 2001).

2.4.2. Gravimetric Measurement Technique

Mass loss measurement is the most accurate and precise method for determining corrosion rate because the experimentation is easy to replicate. Although the method is destructive and long exposure times may be involved, the relatively simple procedure reduces the propensity

to introduce systematic errors. The main issues to consider while using this technique is that since mass can be measured easily only to about 0.1 mg, the sensitivity of mass loss measurements is limited. The mass loss measurements are usually performed after long exposure times, therefore they provide an average rate over time as well as over the exposed surface.

2.4.3. Corrosion Monitoring Using Sensors

The recent developments in the area of smart materials and systems have ushered new openings for SHM and NDE. Smart materials, such as the PZT, and the fibre-optic materials, have facilitated online monitoring with higher resolution and faster response as these materials possess immense capabilities of damage diagnosis. Recently, through the measurement of parameters related to the corrosion of rebars, sensors based on optical fibers and piezo ceramics have been investigated for corrosion assessment in RC structures. Gao et al. (2011) developed a fiber optic corrosion sensor comprising of a fiber bragg grating (FBG) sensor, twin steel rebar elements and some protectors to detect rebar corrosion. Through a series of accelerated corrosion experiments, a relationship between reflected wavelength change from the grating and the weight loss rate of rebar (by gravimetric loss method) was obtained. Using this relationship, it was observed that the larger the wavelength shift, the greater the weight loss rate in the rebar. Fuhr and Huston (1998) presented a multiple-parameter sensing fiber optic sensors, which may be embedded into the roadway and the bridge structures to provide an internal measurement and assessment of their health.

Lalande et al. (1996) used PZT sensors to detect abrasive wear (a type of corrosion) in complex precision parts like those found in gear sets. Simmers (2005) reported the

application of PZT sensors using the EMI technique to detect corrosion induced damage in plates and beams and found that the technique correlated well with the change in the corrosion pit depth and could reasonably detect and quantify the pre-crack surface corrosion, which often leads to shortened fatigue life in structures. Thomas and Welter (2004) used “Lamb” waves to detect material loss through corrosion in thin plate’s representative of aircraft skins using piezoelectric wafer sensors in pitch-patch configurations. They found that as the “Lamb” waves travelled through the simulated corrosion damage, the signal changed and correlated well with the magnitude of the damage. Park et al. (2007) employed PZT sensors using miniaturized impedance measuring chip (AD5933) and a self-sensing macro fiber composite (MFC) patch to detect and quantify corrosion in aluminium structures. Park and Park (2010) conducted an experimental study involving wireless monitoring of corrosion damage in metallic structures and found that the amount of resonant frequency shift increased with the increase in the extent of corrosion. Bedekar et al. (2008) noted a systematic variation in the conductance of the PZT patch as corrosion progressed in their aluminium test specimen. Their results also indicated an optimal distance between the piezoelectric sensor and the location of corrosion. Recently, Yang et al. (2013) conducted experimental study to monitor the local corrosion of a steel beam using the EMI technique and found that a quantitative relationship exists between the damage index and corrosion time, which can be used as a baseline reference for subsequent local corrosion monitoring.

The next section deals with the SHM techniques emphasizing on EMI technique.

2.5 IMPEDANCE BASED STRUCTURAL HEALTH MONITORING

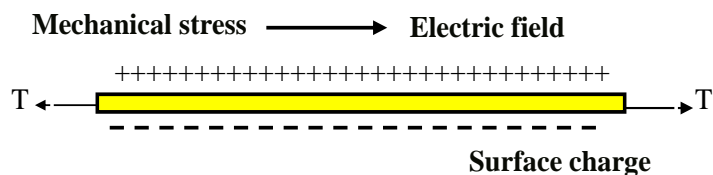
The advent of the EMI technique using PZT sensors has provided a new path forward for non destructive SHM, which can be possibly utilized for corrosion condition assessment. Furthermore, the large physical size of host structures may require innovative sensing technologies utilizing appropriate software and hardware systems for data acquisition/reduction for rational SHM/NDE applications. Over the past two decades, several SHM and NDE techniques have been reported in the literature, based on either the global or the local interrogation of structures. The EMI based SHM provides an interface between the global vibration techniques and the traditional ultrasonic techniques (Shanker et al., 2011). The PZT patches, owing to the inherent direct and converse mechatronic effects, can be utilized as impedance transducers for SHM using EMI technique, through the measurement of electrical admittance (consisting of real and imaginary parts, the conductance and susceptance) as a function of frequency. It has been demonstrated that the EMI-based SHM method is a practical powerful and innovative tool for local damage detection for a variety of structures.

2.5.1 Piezoelectric Materials

The piezoelectric materials have a unique property of generating electric dipoles (opposite surface charges) when subjected to mechanical stress (see Fig. 2.5 a) and conversely they undergo mechanical deformations when subjected to electric fields as shown in Fig. 2.5 (b). The piezo materials are commercially available as ceramics and polymers. Lead zirconate titanate oxide or PZT, which has a chemical composition ($Pb[Zr(x)Ti(1-x)]O_3$), is the most widely used type piezoceramic. It is light weight, low-cost, small size and has good dynamic

performance, high elastic modulus, high rigidity, brittleness and low tensile strength. Besides, it exhibits large range of linearity, fast response, long term stability and high energy conversion efficiency (Sirohi and Chopra, 2000a). On the other hand piezopolymers are characterized by low charge characteristics and low stiffness. Due to their flexibility, they can be formed into thin sheets and can be adhered to any curved surfaces. However, piezopolymers are more sensitive to mechanical loads over a larger range, which renders them to be better sensors. The most commonly available form of piezopolymers is the Polyvinylidene Fluoride (PVDF), which has negligible shear lag effect (Sirohi and Chopra, 2000b).

(a) Direct effect (Sensor)



(a) Converse effect (Actuator)

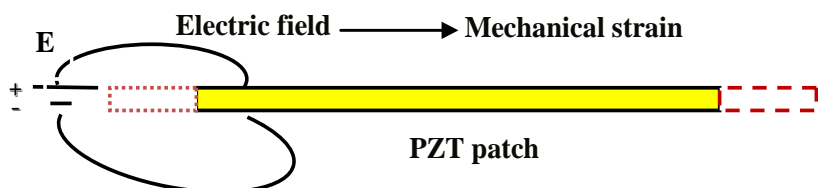


Figure 2.5 Direct and converse effect of piezoelectric materials

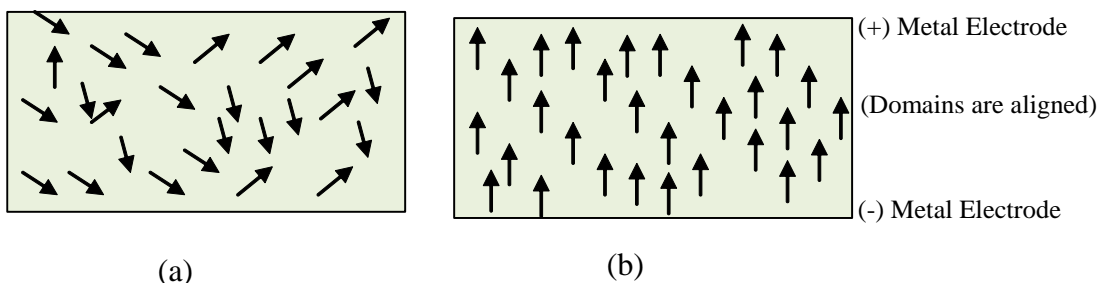


Figure 2.6 Typical Polarization observed in piezoceramic materials (Cook, 2001)
 (a) Unpolarized Ceramic Material (b) Polarized Ceramic Material

2.5.2 Geometric Details of PZT Patches

Several types of PZT patches are commercially available in market in different shapes such as circular, rectangular, square and of varying dimensions. Fig. 2.7 shows a typical commercially available PZT patch used in the present research. The characteristic feature of the patch is that the electrode from the bottom edge is wrapped around the thickness, so that both the electrodes are available on one side of the PZT patch, while the other side can easily be bonded to the host structure.

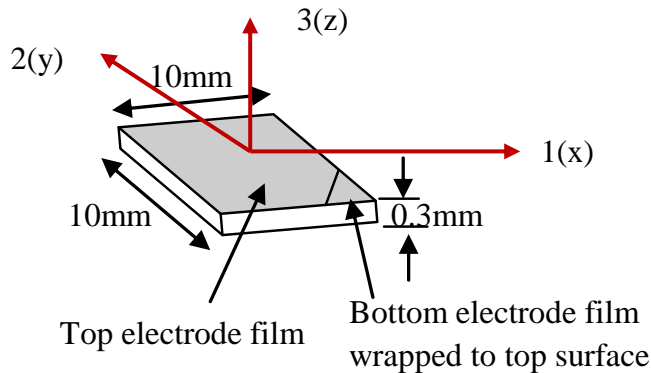


Figure 2.7 Geometric details of a typical PZT patch (PI Ceramics, 2012)

2.5.3 Diverse Applications of Piezoelectric Materials

Since this thesis is primarily concerned with piezoelectric materials, some typical applications of these materials are briefly described here. Traditionally, piezoelectric materials have been well-known for their use in accelerometers, strain sensors, distributed vibration sensors, and pressure transducers (Sirohi and Chopra, 2000a and 2000b). They have been shown to be very promising in active structural control of lab-sized structures and machines and underwater acoustic absorption, robotics, precision positioning and smart skins

for submarines (Kamada et al., 1997; Manning et al., 2000; Song et al., 2002). The present research aims at exploring the application of piezo sensors in corrosion monitoring.

2.6. EMI TECHNIQUE USING PZT PATCHES

2.6.1 Physical Principles

In the EMI technique, a PZT patch is bonded to the surface of the structure to be monitored using a high strength epoxy adhesive, and electrically excited via an inductance capacitance and resistance (LCR) meter. In this configuration, the PZT patch essentially behaves as a thin plate undergoing axial vibrations and interacting with the host structure, as shown in Fig. 2.8 (a and b) and these interactions are reflected back in the form of electrical admittance consisting of conductance and suseptance. Assuming 1D interaction (host structure as a skeletal structure), the PZT patch-host structure system can be modelled as a mechanical impedance (due the host structure) connected to an axially vibrating thin bar (the patch), as shown in Fig. 2.8 (a). The patch in this figure expands and contracts dynamically in direction ‘1’ when an alternating electric field E_3 (which is spatially uniform i.e. $\partial E_3 / \partial x = \partial E_3 / \partial y = 0$) is applied in the direction ‘3’. The patch has half-length ‘ l ’, width ‘ w ’ and thickness ‘ h ’. The direct and converse effects, can be mathematically expressed as (Ikeda 1990)

$$D_3 = \overline{\epsilon_{33}^T} E_3 + d_{31} T_1 \quad (2.9)$$

$$S_1 = \frac{T_1}{Y^E} + D_{31} E_3 \quad (2.10)$$

where axis ‘3’ points along the thickness of the patch and axes ‘1’ and ‘2’ lie in the plane of patch, as shown in the Fig. 2.8 (a). Further, S_1 is the strain along axis ‘1’, D_3 the electric

displacement over the surface of PZT patch, d_{31} the piezoelectric strain coefficient and T_1 the axial stress in the patch along the axis '1'. electric field and $\overline{\varepsilon_{33}^T} = \varepsilon_{33}^T(1 - \delta j)$ its complex electric permittivity at constant stress, with η and δ denoting the mechanical and dielectric loss factors of the patch respectively. The PZT loading in direction '3' can also be neglected by assuming the frequencies involved to be much less than the first resonant frequency for thickness vibrations. The vibrating patch is assumed infinitesimally small and to possess negligible mass and stiffness as compared to the host structure.

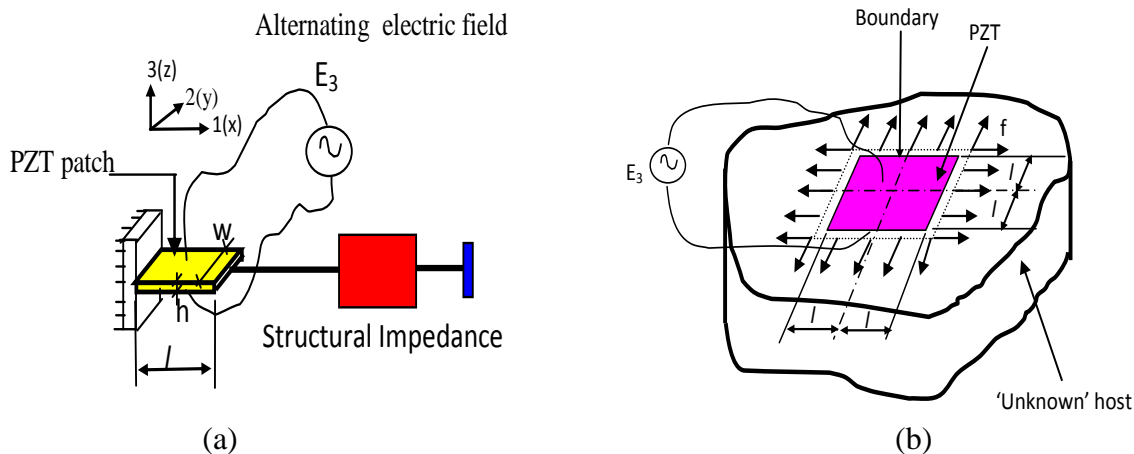


Figure 2.8 Bonded PZT patch and its interaction (a) Modelling of PZT-structure interaction (1D) (Bhalla and Soh, 2003) (b) A PZT patch bonded to the host structure (2D)

The structure can therefore be assumed to possess uniform dynamic stiffness over the entire bonded area. The two end points of the patch can thus be assumed to encounter equal mechanical impedance, Z . Under this condition, the PZT patch has zero displacement at the mid-point ($x= 0$), irrespective of the location of the patch on the host structure. Under these assumptions, the vibrations of the 1D patch can be represented by the following differential equation (Liang et al., 1994), derived based on dynamic equilibrium of the PZT patch.

$$\overline{Y^E} \frac{\partial^2 u}{\partial x^2} = \rho \frac{\partial^2 u}{\partial t^2} \quad (2.11)$$

where ‘ u ’ is the displacement at any point on the patch in direction ‘1’. Solution of the governing differential equation by the method of separation of variables and boundary conditions consistent with assumptions stated above leads to

$$u = A \sin(kx) e^{j\omega t} \quad (2.12)$$

where k is the wave number, related to the angular frequency of excitation ω , the density ρ and the complex Young’s modulus of elasticity of the patch by

$$k = \omega \sqrt{\frac{\rho}{\overline{Y^E}}} \quad (2.13)$$

Making use of the PZT constitutive relation (Eq. 2.13), and integrating over the entire surface of the PZT patch (0 to $+l$), we can obtain an expression for the electro-mechanical admittance (the inverse of electro-mechanical impedance) as

$$\overline{Y} = \omega j \frac{wl}{h} \left[\overline{\epsilon_{33}^T} + \left(\frac{Z_a}{Z + Z_a} \right) d_{31}^2 \overline{Y^E} \frac{\tan kl}{kl} - d_{31}^2 \overline{Y^E} \right] \quad (2.14)$$

where Z_a is the short-circuited mechanical impedance of the PZT patch, given by

$$Z_a = \frac{kwh\overline{Y^E}}{(j\omega)\tan(kl)} \quad (2.15)$$

Z_a is defined as the force required to produce unit velocity in the PZT patch in short circuited condition (i.e., ignoring the piezoelectric effect) and ignoring the host structure. The electric current, which is the time rate of change of charge, can be obtained as

$$\iint_A \dot{D}_3 dx dy = j\omega \iint_A D_3 dx dy \quad (2.16)$$

It may be noted that no assumption about the operating frequency range is made in the derivation of the above equation. For the particular case of $\omega \ll \omega_{res}$, when $\frac{\tan kl}{kl} \rightarrow 1$, the Eq. (2.14) reduces to

$$\bar{Y} = \omega j \frac{wl}{h} \left[\frac{\varepsilon_{33}^T}{Z + Z_a} - \left(\frac{Z}{Z + Z_a} \right) d_{31}^2 \bar{Y}^E \right] \quad (2.17)$$

Eq. (2.14) or Eq. (2.17) couples the mechanical impedance of the mechanical system to the electro-mechanical admittance of the PZT-structure system. The first term in these equations is the capacitance of PZT, and the remaining terms signify the mechanical interaction between the structure and the actuator.

The abovementioned 1D model derived by Liang et al. (1994) is considered oversimplified for the modelling of some complex structural systems. Zhou et al. (1995, 1996) extended the impedance based 1D (skeletal) model to a more generic 2D (planar) model by Incorporating direct impedances Z_{xx} and Z_{yy} , and the cross impedances Z_{xy} and Z_{yx} in Liang's equation. Although the analytical derivations of Zhou et al. (1995 and 1996) are reasonably accurate the experimental difficulties prohibit their direct application for extraction of host structure's mechanical impedance. To alleviate the shortcomings inherent in the existing models, Bhalla and Soh (2004a) introduced a new concept called 'effective impedance'. The actual interaction between the patch and the structure is not restricted at the end points, but extended all over the finite size of PZT patch as shown in Fig. 2.8 (b). They introduced the concept of effective velocity rather than drive point velocity, thus ensuring that the force transmission between PZT patch and structure occurs along the entire boundary of the patch

shown in Fig. 2.8 (b). They derived the following expression for complex admittance of the bonded PZT patch (assumed square shape, as shown in Fig. 2.7 a), as

$$\bar{Y} = \frac{\bar{I}}{\bar{V}} = G + Bj = 4\omega j \frac{l^2}{h} \left[\frac{\varepsilon_{33}^T}{\varepsilon_{33}^T} - \frac{2d_{31}^2 Y^E}{(1-\nu)} + \frac{2d_{31}^2 Y^E}{(1-\nu)} \left(\frac{Z_{a,eff}}{Z_{s,eff} + Z_{a,eff}} \right) \left(\frac{\tan kl}{kl} \right) \right] \quad (2.18)$$

where $Z_{a,eff}$ is the short-circuited effective mechanical impedance of the structure, ν the Poisson's ratio. Any damage to the structure (such as corrosion, which changes the mass and stiffness characteristics of the structure) will cause the structural parameters to change and will thus alter the structural impedance ($Z_{s,eff}$), which in turn changes the admittance (\bar{Y}) in the above equation, thus serving as an indicator of the state of health of the structure.

The EMI technique has been shown to be extremely sensitive to incipient damages, it is practically immune to mechanical noise and demands a low implementation cost (Park et al., 2000a). The PZT patches can easily be bonded to inaccessible locations of structures and aircraft and can be interrogated as and when required, without necessitating the structures to be placed out of service or any dismantling/ re-assembling of the critical components. All these features definitely give an edge to the EMI technique over other existing passive sensor systems.

2.6.2 Frequency Range Selection

One of the unique characteristic of the EMI technique is its high frequency of excitation (in the order of 50 to 500 kHz) which ensures high sensitivity. Sun et al. (1995) recommended that the frequency range in the EMI technique is to be selected such that major vibration modes of structure are included. Park et al. (2003) and Bhalla (2001) additionally recommended that a frequency range ought to be kept within 30 to 400 kHz to ensure high

sensitivity to incipient damage invisible to naked eye. Further, it is also recommended that frequency larger than 500 kHz is unfavourable if lateral modes are used, because the sensing region becomes extremely localized and the PZT patch shows adverse sensitivity to its bonding conditions. Baptista and Filho (2010) proposed a formal procedure to determine the frequency ranges in which the PZT transducers are more sensitive for damage detection.

2.6.3 Effect of Temperature

The electrical admittance signatures acquired from the impedance analyzer are found to be temperature sensitive (Sun et al., 1995; Park et al., 1999). The most undesirable effects caused by temperature on the acquired signatures are the horizontal shift, caused by the change in the host material's Young's modulus, and the vertical shift, due to variations in parameters ε_{33} and d_{31} of the PZT patch (Bhalla and Soh, 2004a). Therefore, the effect of temperature was studied by several researchers (Sun et al., 1995; Bhalla, 2001; Schulz et al., 2003 and Nguyen et al., 2004) and concluded that the overall shift in the frequency spectrum varies linearly with temperature over narrow frequency bands. The most critical vertical shift was caused by the changes of ε_{33} . Sun et al. (1995) suggested a compensation technique based on cross correlation coefficient to compensate for temperature induced horizontal shift. Park et al. (1999) latter proposed an empirical based methodology for temperature compensation, proving the damage detection capability of the EMI technique under fluctuating temperature. In the present research, all the tests were performed under controlled laboratory conditions so that the temperature fluctuations were controlled.

2.6.4 Sensing Range and Optimal Placement of PZT Patches

In the EMI technique, the typical excitation frequency lies in the range of 30-400 kHz. This high frequency of excitation induced renders the actuation and sensing zone to be localized. Esteban (1996) performed extensive theoretical modelling to identify the sensing region of the EMI technique. Based on various case studies, it has been estimated that the sensing zone is closely related to the host materials and density, ranging from 0.6m in concrete to 2-3m in metal. Therefore, in actual application, spacing between the PZT patches should be reasonably chosen according to the abovementioned considerations. Soh et al. (2005) suggested that the PZT patches should be placed at critical location such as those susceptible to shear crack and bending failure and thus the number of the PZT patches required in monitoring the entire structure can be optimized.

2.6.5 Excitation Voltage and Signature Acquisition

The PZT patch is normally excited by the LCR meter with an alternating voltage signal of 1 volt r.m.s. (root mean square) over the user specified frequency range. Sun et al. (1995) reported that the conductance signature remains practically constant when the excitation voltage was increased from 0.5 to 15 V.

2.6.6 Instrumentation and Other Considerations

The impedance measurements (i.e., the real and the imaginary parts) need to be measured for the complete impedance or admittance signatures. For this purpose, there are LCR meters such as Agilent E4980A Precision LCR meter and Wayne Kerr Precision Impedance Analyzer. The issues related to the hardware were first investigated by Peairs et al. (2004),

who proposed a low-cost version of the EMI technique using a FFT analyzer which is less expensive than LCR meters. The work was further extended by Xu and Giurgiutiu (2005) Park et al. (2006) and Panigrahi et al. (2008). Bhalla et al. (2009) further extended the work of Panigrahi et al. (2008) and developed a new impedance-measuring approach with lower cost, greater accessibility, and smaller size.

For a surface bonded PZT patch, the efficiency of strain transfer between the PZT patch and the host structure is mechanically joined by adhesive/bonding layer. In the EMI technique, the adhesive is capable of changing the structural signature by lowering the peaks of the conductance and the slope of the susceptance, as reported by various researchers (Sirohi and Chopra, 2000b; Bhalla, 2004; Qing et al., 2006; Dugnani, 2009; Bhalla et al., 2009). Bhalla and Soh (2004a) suggested that the effect of adhesive on the PZT patch is negligible if the bonding layer is less than one third of the patch's thickness.

2.7 MAJOR RESEARCH IN ELECTRO MECHANICAL IMPEDANCE TECHNIQUE SINCE 1990's

The capabilities of the EMI technique and its advantages have been proven over extensive investigations. Major developments and contributions made by various researchers in the field of EMI technique during the last two decades are summarised as follows. A very detailed review of the various case studies and applications is covered by Park et al., 2003b and Bhalla 2004 who have provided a comprehensive review of the developments in EMI technique since its invention in 1995. The developments after 2004 are summarized as follows:

Bhalla et al. (2005) presented a detailed review of the available sensor technologies and methods for comprehensive monitoring with special emphasis on the conditions encountered underground practically.

Lim et al. (2006) presented a new method for identifying structures from the measured admittance signatures in terms of equivalent structural parameters, whereby the identified parameters are used for damage characterization. The new method has been applied to a truss, a beam and a concrete cube, and found to be able to successfully perform structural identification and damage diagnosis

Hey et al. (2006) presented practical issues concerning the implementation of EMI based SHM and proposed new sensors interrogation algorithms utilizing the sensor multiplexing technique to reduce the time required in interrogating PZT patches one by one.

Yang et al. (2008) simulated the PZT–structure interaction at the high frequency range (upto1000 kHz) using ANSYS8.1. Their studies proved that FEM could merge as an excellent alternative to the experimentation in the study of the EMI technique.

Rickli and Camelio (2008) combined a PZT sensor with multi variate statistical process control (MSPC) to accurately monitor the structural integrity of locating fixtures. This methodology reduced the cost associated with production downtime due to faulty failures and was able to reduce the false alarms and enabled healthy sensor identification with improved capabilities.

Shanker et al. (2010) proposed the simultaneous application of the local EMI and the global dynamic techniques using the same set of PZT sensor patches for improved SHM. Based on

the experimental study conducted on a two-story reinforced concrete frame structure using PZT patches embedded in the structure it was well established that the same PZT patch can be used as the sensor element for the global dynamic technique as well as the local EMI technique. The EMI technique was able to detect the incipient damage more effectively, and the global dynamic technique was effective for moderate to severe damages thus complementing each other.

Neto et al. (2011) proposed a low cost, highly expandable SHM architecture for monitoring an array of PZT transducers, which does not use fast Fourier transform analyzers/algorithms nor any digital computers for processing. They concluded that the proposed architecture offers stability, reliability, low cost, and scalability and monitor any kind, size, and complexity of a structure. It was shown that the impedance signals obtained from the proposed architecture are similar to those obtained from a classical impedance analyzer with much lower better adapted for industrial application.

Yan et al. (2011) proposed an analytical model of a cracked functionally graded beam. The dynamic behaviour of the PZT patches was considered and a viscoelastic law was adopted to describe the bonding imperfection between the PZT patches and the beam.

Lim and Soh (2012) conducted experimental, analytical and numerical studies to investigate the effect of varying axial load in the presence of fixed boundary conditions on the admittance signatures and suggested that the effect of the boundary condition was substantial and needs to be carefully considered in real-life application of the EMI technique for SHM.

Baptista et al. (2012) presented a simple and versatile measurement system for SHM using the EMI technique, which allowed real time data acquisition from multiple sensors and also

included temperature compensations. The proposed system is low cost compared to the conventional impedance analyzers.

Bhalla et al. (2012) presented new approach for fatigue life assessment of bolted steel joints using the equivalent stiffness determined by surface-bonded piezo-impedance transducers. The equivalent system parameters of the joint were identified from the acquired electro-mechanical admittance signatures. Through tests on three prototype steel joints, empirical equations were derived to relate the residual fatigue life to the loss of equivalent identified stiffness. The most promising feature of the proposed approach was that it employs the admittance signature of the surface-bonded piezo transducers directly, thereby circumventing the determination of the in situ stiffness of the joint.

Xu and Jiang (2012) showed that the EMI technique can be employed to evaluate the condition of interfacial bolts for a concrete-steel composite girder element with removable bolts which are employed to simulate the damage of bolts.

Annamdas and Yang (2012) extended the application of EMI technique for monitoring of soil excavation carried out in Singapore and concluded that the PZT sensors can be groomed for practical applications without much difficulty.

Quinn et al. (2012) developed an embedded wireless sensing system for monitoring initial curing and health of concrete structures. Their results showed that the embedded EMI method was sensitive to the removal of formwork and possibly debonding effects on aggregate and the effect that these have on the concrete.

Providakis et al. (2013) designed a wireless and miniaturized EMI based measuring to monitor the early age strength of concrete. Based on their experimental studied, they found that the EMI signatures gradually shift to the right as the concrete curing time increased.

Cherrier et al. (2013) proposed a method to generate damage localization map based on two techniques EMI and inverse weighting interpolation, which was validated on one dimensional and two dimensional composites structures.

Recently, Annamdas and Radhika (2013) presented some important developments in monitoring the metallic and non-metallic structures using the EMI technique, specifically concentrating on wired, wireless and energy harvesting methods.

2.8 LIMITATIONS IN APPLICATION OF PZT PATCHES FOR STRUCTURAL HEALTH MONITORING

The main limitation with the PZT materials is their brittle nature, due to which, the PZT sheets cannot withstand bending, exhibit poor conformability to curved surfaces, show considerable fluctuation in their electric properties with temperature. Also, soldering wires to the electrode of PZT patch requires special skill and often results in broken elements, unreliable connections or localized thermal depoling of the elements. The other limitations with PZT materials are (i) aging: PZT patches erode gradually, in a logarithmic relationship with time after polarization (PI Ceramic, 2012). Exact rates of aging depend on the composition of the ceramic element and the manufacturing process used to prepare it. (ii) Electrical Limitations: PZT patches depolarize when exposed to a strong electric field of polarity opposite to that of the polarizing field. A field of 200-500 V / mm or higher can have

a significant depolarizing effect. The degree of depolarization depends on the grade of material, exposure time, temperature, and other factors. (iii) Mechanical Limitations: Application of mechanical stress on PZT material beyond certain limit can destroy the alignment of dipole. This limit generally depends on the type of grade and the brand of the material used to prepare the PZT patches. (iv) Thermal Limitations: If a PZT sheet is heated to above the Curie point (temperature at which materials lose its piezoelectric effect), the domains become disordered and the material gets depolarized. The recommended upper operating temperature for a ceramic is between 0 °C and the Curie point. In general, temperature fluctuations affect the properties such as d_{31} , $\overline{\epsilon}_{33}^T$ and $\overline{Y^E}$ of the PZT patch, and to some extent structural properties of the host system (Bhalla, 2001).

In addition to the above, the specific limitations of EMI technique include:

- 1) Due to the utilization of high excitation frequencies, the sensing zone of the PZT patch is very small (For metals it is 2m and for non homogeneous materials 0.2m), so in order to monitor a real life structure, several PZT patches need to be deployed. The location of the bonding of the PZT patch needs to be judiciously decided.
- 2) The main drawback of the EMI technique is its inability to assess the overall structural stability as it is a local SHM technique and since most of the civil structures are statically indeterminate, the cracking of a few joints/members may not necessarily affect the overall safety and stability of the monitored structure (Bhalla, 2004) and the data need to be carefully interpreted.

2.9 SUMMARY: CRITICAL POINTS OF REVIEW

In this chapter, initially a general idea about the corrosion and its process with emphasis on rebar corrosion is presented. The main causes of rebar corrosion in RC structures (i.e., chloride induced and carbonation induced corrosion) are briefly described. Various techniques to detect and quantify the rebar corrosion are elaborated with their limitations.

As the primary focus of this research is to extend the applications of PZT sensors to corrosion monitoring using the EMI technique, the concept of SHM using PZT sensors is described covering the geometric details, sensing abilities and diverse applications of the PZT sensors. During the recent years, the EMI technique using the PZT sensors has proven to be an efficient tool in SHM. As the research is focused on EMI technique, the basic principles and the governing equations of the technique are elaborately discussed and finally the recent technological developments of this technique are presented.

From the critical literature review discussed regarding rebar corrosion detecting techniques and from the SHM using EMI technique, following points can be noted

1. The use of potential measurements to assess corrosion has been criticized in the past by various researchers for its instability depending on the prevailing measurement conditions (Ghaz et al., 1990; Elsener et al., 2003).
2. There is no general correlation between the i_{corr} (corrosion current rates) and potential measurements (Broomfield 2007). For practical purposes, the potential values need to be complimented with other corrosion assessment techniques.

3. The LPR measurements are subjected to several complications, such as the compensation of IR drops, the presence of localized corrosion, the interference with other electrical signals, and the determination of the rebar area being tested (Gozalez et al., 1985 and Feliu et al., 1989)
4. The gravimetric measurements such as mass loss method is an efficient method for determining the corrosion rates, however it is destructive in nature and is generally performed after long exposure periods.
5. From the literature review, it is found that the EMI technique is very effective and sensitive in detecting the damage (loss of structural parameters) caused to the structures. Detection of corrosion in RC structures using this technique is still a new area of research and has not yet been explored, although some of the researchers had applied the EMI technique for corrosion monitoring using PZT sensors, their work has been only limited to the metallic structures and using statistical parameters only.
6. Further, limited research is available based on the utilization of extracted equivalent parameters (from PZT patches) for correlation with the actual parameters, while all the previous studies used the raw conductance signature for damage detection. The success of the equivalent parameters in concrete (Soh and Bhalla, 2005) and fatigue (Bhalla et al., 2012) provides motivation for exploring their potential for better corrosion assessment.

2.10 RESEARCH OBJECTIVES

Based on the critical review points relating to the corrosion detection techniques and SHM using EMI technique, the following objectives have been set for the present Ph. D. research:

1. To investigate the capabilities of PZT patches (using the EMI technique), to inspect the structure in real-time (to supplement routine inspections) so that corrosion could be detected and treated before significant cracking develops.
2. To develop a new corrosion detection and assessment methodology using PZT patches, which can be autonomously, remotely monitor, alert operators about the immediate structural problems and speed up the maintenance repairs.
3. To present a new diagnostic approach for the assessment of corrosion based on the equivalent system parameters identified by means of the EMI technique, using real and imaginary components of the admittance signature and also identify the damage sensitive equivalent parameters for reinforced concrete structures.
4. To develop an empirical model for expressing corrosion (chloride induced) severity in terms of changes in the equivalent structural parameters (stiffness and mass) directly “identified” by PZT patches surface bonded to the bare steel bars as well as rebars embedded in concrete.
5. To derive empirical relation between the actual stiffness loss and the PZT identified stiffness loss, which can be used in real life corrosion monitoring of RC structures, where the determination of actual stiffness loss of rebar is impractical.
6. To differentiate various phrases of corrosion i.e., corrosion initiation, propagation and cracking using the derived equivalent stiffness model.
7. To determine corrosion rates, knowing the mass loss of the rebar from the equivalent mass model.
8. To detect, with reasonable certainty, the carbonation initiation corrosion through accelerated carbonation tests and to correlate the structural changes due to

carbonation with the microstructural properties i.e. with scanning Electron microscope (SEM) imaging and Raman spectroscopy analysis.

9. To apply the developed model of accelerated chloride induced corrosion in determining the corrosion rates in natural environmental conditions and further study the effect of FA blended concrete on reinforcement corrosion.

The following chapters present details of how the above objectives are met, starting from experimental study on bare steel rebars to the ones embedded inside concrete, experiencing chloride/carbonation induced corrosion process.

CHAPTER- 3
DIAGNOSIS OF CHLORIDE INDUCED CORROSION IN
BARE STEEL BARS

3.1 INTRODUCTION

Steel is principally used as the reinforcing material in RC structures as it is the time proven match for concrete. RC structures are designed on the premise that steel and concrete act together to withstand the induced forces. The coefficients of thermal expansion for both steel and concrete are approximately the same; this along with excellent bendability property and bond with concrete makes steel the best material as reinforcement in the RC structures. One of the problems encountered by this combination is the occurrence of corrosion in steel, which is a very common problem faced by the ageing infrastructure across the world. The interest of the scientific community in rebar corrosion problem has increased during the last several years because of the wastage of the precious metal owing to corrosion, apart from endangering the structural performance. Corrosion of steel reinforcement has been identified as the most common cause of deterioration and premature failure of RC structures (Montemor and Simoes, 2003).

This chapter presents a new approach for the assessment of corrosion in bare steel bars, using the EMI technique. The quantification of corrosion induced damage is based on the equivalent parameters identified by the surface bonded PZT patch. The chapter covers the specific experiments conducted on bare steel bar specimens followed by the development of empirical mass and stiffness models based on the measured electro-mechanical impedance data.

3.2 MECHANICAL IMPEDANCE OF STRUCTURES

Lamb waves techniques and the EMI technique are the two prominent damage detection techniques, which utilize the direct and converse capabilities of smart piezoelectric materials to non-destructively inspect and evaluate the health of structures. Both techniques have recently been integrated into autonomous SHM devices, such that the same self-sensing patch can perform both detection techniques (Park et al., 2003a). The main aim of this research is to evaluate the EMI technique as a corrosion detection and quantification tool for rebars embedded in concrete. For this purpose, as a first step, the tests have been conducted on bare steel bars and then the experiments are extended to steel bars embedded in concrete.

Electrical impedance is a parameter used to characterize electric circuits and components, given as

$$Z = R + Xj \quad (3.1)$$

where the real part of impedance is the resistance R and the imaginary part is the reactance X . The electrical admittance on the other hand, is a measure of how easily a circuit or a device allows current to flow, and is the inverse of impedance. It is defined as

$$Y = \frac{1}{Z} = G + Bj \quad (3.2)$$

where G is called the conductance and B the susceptance. To understand the EMI technique, it is important to understand the concepts of mechanical impedance as it is analogous to electrical impedance.

A harmonic force, acting upon a structure, is given as (Bhalla, 2004)

$$F(t) = F_o \cos \omega t + jF_o \sin \omega t = F_o e^{j\omega t} \quad (3.3)$$

The resulting velocity response \dot{u} , at the point of application of the force, is also harmonic in nature. However, it lags behind the applied force by a phase angle ϕ , due to the ‘mechanical impedance’ of the structure. Hence, velocity can also be represented as a phasor, as

$$\dot{u} = \dot{u}_0 \cos(\omega t - \phi) + j\dot{u}_0 \sin(\omega t + \phi) = \dot{u}_0 e^{j(\omega t - \phi)} \quad (3.4)$$

The mechanical impedance of a structure, analogous to the electrical impedance, at any point, is defined as the ratio of the driving harmonic force to the resulting harmonic velocity at that point, in the direction of the applied force, that is

$$z = \frac{F}{\dot{u}} = \frac{F_o e^{j\omega t}}{\dot{u}_0 e^{j(\omega t - \phi)}} = \frac{F_o}{\dot{u}_0} e^{j\phi} \quad (3.5)$$

The main advantage of the impedance approach is that the differential equations of Newtonian mechanics are reduced to simple algebraic equations and a black-box concept is introduced. Critical forces and velocities only at one or two points of interest need to be considered, thereby eliminating the need of a complex analysis of the system (Bhalla, 2004).

Like the electrical relationships, combinations of mechanical elements like dampers, springs, and masses comprise mechanical systems. The mechanical impedances of the three basic mechanical elements such as for a pure mass ‘ m ’ can be derived as ‘ $m\omega j$ ’ (Hixon, 1988). Similarly, the mechanical impedance of an ideal spring possessing a spring constant ‘ k ’ can be derived as ‘ $-jk/\omega$ ’, and that of a damper can be obtained as ‘ c ’ (the damping constant). The rules for series combination of impedance elements are similar to electrical impedances connected in parallel. Similarly, mechanical impedances connected in parallel are treated like

electrical impedances in series. Hence, for a parallel combination of ‘ n ’ mechanical systems, the equivalent mechanical impedance is given by Hixon (1988) as

$$Z_{eq} = \sum_{i=1}^n Z_i \quad (3.6)$$

and, for a series combination,

$$\frac{1}{Z_{eq}} = \sum_{i=1}^n \frac{1}{Z_i} \quad (3.7)$$

A healthy structure may be thought of as a multiple degree of freedom system composed of several mechanical elements i.e., different combinations of mass, spring, and damper elements. If the basic elements are known, they could be combined using superposition theorems. The result would be a single impedance equation which would describe the input (Force) output (velocity) relationship for the structure. The equation would define the frequency dependant structural response of the system which thus identifies the healthy mechanical impedance composition of the structure. Thus, if the structure is corroded or cracked, the mechanical impedance composition would deviate from the healthy response, and it would be possible to see the effect of the damage through the mechanical impedance change.

3.3 MECHANICAL IMPEDANCE OF PZT PATCHES

Based on the above concept, Liang et al. (1994) derived the mechanical impedance of the PZT patch (in the short circuited condition), as

$$Z_a = \frac{F_{(x=l)}}{\dot{u}_{(x=l)}} = \frac{whT_{(x=l)}}{\dot{u}_{(x=l)}} = \frac{wh\overline{Y^E}S_{(x=l)}}{\dot{u}_{(x=l)}} \quad (3.8)$$

Where, \dot{u} the velocity response and l , w and h the patch dimensions. It should be noted that only one symmetrical half of the PZT patch (l = half length) has been considered. The next section applies the concept of mechanical impedance to corrosion degradation of bare steel bars.

3.4 DETAILS OF ACCELERATED CORROSION STUDY

The mechanics of chloride induced corrosion in rebar of RC structures was discussed in detailed in Chapter 2. In this chapter, the feasibility of the EMI technique for corrosion detection in bare steel bars is explored. Three high yield deformed (HYD) steel bars of Fe415 grade (IS 1786, 1985) of 300 mm length and 16 mm diameter were chosen for performing the accelerated corrosion experiments. All the bars were machined in the central portion so as to achieve a smooth surface to bond the patch (as shown in Fig. 3.1a). A thin layer of two part Araldite epoxy adhesive was applied on the machined surface and a PZT patch of size 10x10x0.3 mm and grade PIC 151 (PI Ceramics, 2012) was placed on it. Light pressure was applied over the assembly using small weight. The set up was left undisturbed in this condition at room temperature for 24 hours to enable full curing of the adhesive. Wires were then soldered to the electrodes of the PZT patch and connected to Agilent E4980A LCR meter (Agilent Technologies, 2012), as shown in Fig. 3.1 (b). The LCR meter imposes an alternating voltage signal of 1 volts rms to the bonded PZT transducer over the user specified preset frequency range (100-300 kHz in the present case). The magnitude and the phase of the steady state current are directly recorded in the form of conductance and susceptance

signatures in the frequency domain, thereby eliminating the requirements of domain transform. In addition, no amplifying device is necessary. In this manner, the electro-mechanical admittance signature, consisting of the real part (conductance G) and the imaginary part (susceptance B) was acquired in a frequency range of 100-300 kHz for all the three bars, as shown in Fig. 3.2 for a typical specimen. A frequency interval of 100 Hz was used for each admittance measurement. Since the conductance signatures of piezo-impedance transducers have been reported to be temperature sensitive (Sun et al., 1995; Park et al., 1999), all the tests were performed under controlled laboratory conditions so that the temperature fluctuations could be ruled out.

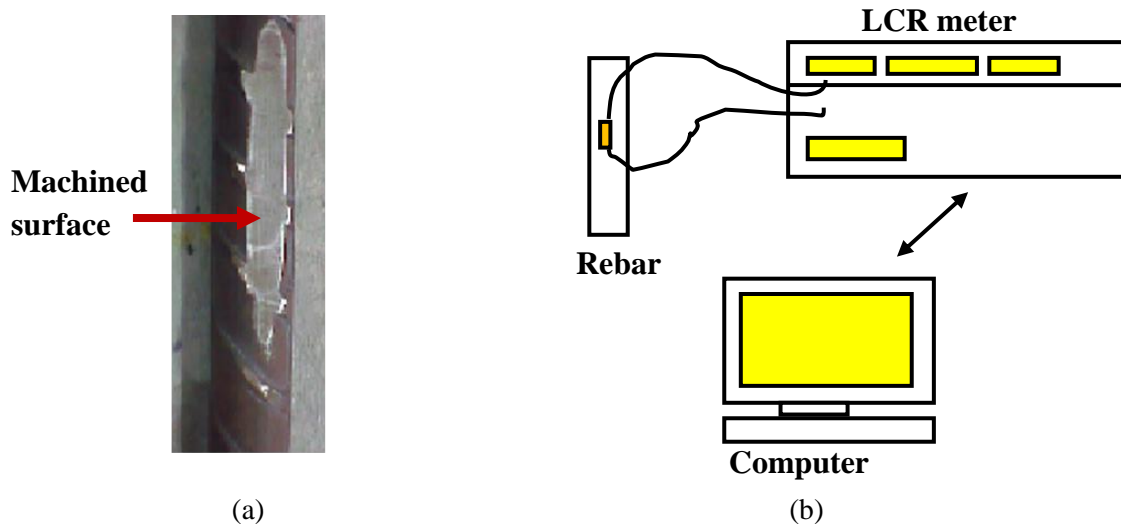


Figure 3.1 Experimental set up (a) Rebar specimen prepared for bonding the PZT (b) Experimental set up

Under normal environmental conditions, corrosion of a rebar is a relatively slow process, often taking several years to progress significantly. In order to obtain the results in a reasonable time frame for a laboratory-based study, accelerated corrosion through impressed current technique was adopted (Grattan et al., 2009; Zheng et al., 2009 and 2010; Gao et al., 2011). After the baseline signatures were acquired (as shown in Fig. 3.2), the specimens were

placed in a beaker containing “brine” solution (of salinity 35 parts per thousand). It was duly ensured that the PZT patch was always above the top surface of the brine solution i.e. the PZT patch was never submerged in the solution, so as to rule out the possible deterioration to PZT patch. To accelerate corrosion, an electrical loop was set up with the steel bar specimen forming the anode and the negative terminal was connected to a copper bar dipped in the solution acting as cathode, as shown in Fig. 3.3. A constant current $150\mu\text{A}/\text{cm}^2$ was applied to the specimens using fixed power supply device, model ST 4076 (Scientech Technology, 2011) for a total period of eight hours and the admittance signatures were acquired periodically at an interval of one hour. Before the signature acquisition, the bars were taken out of the solution and dried under running fan for a period of about 15 minutes.

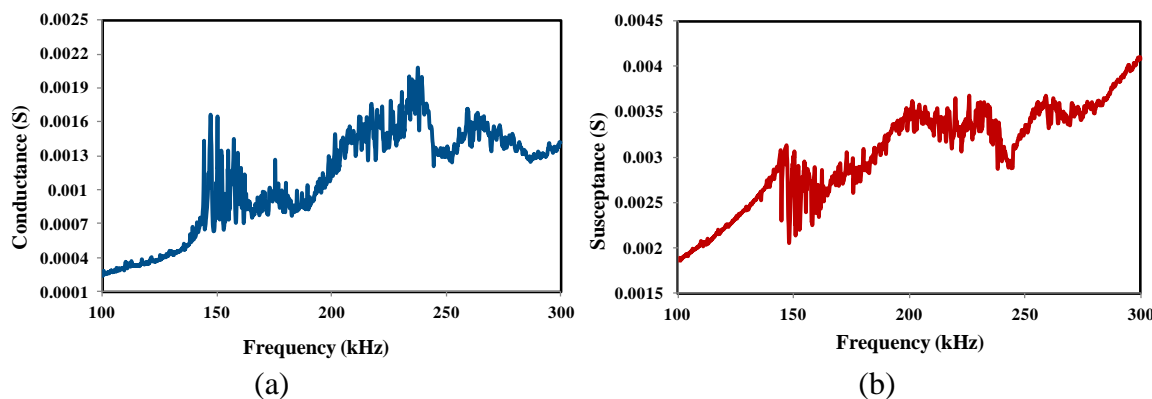


Figure 3.2 Experimental admittance signatures (a) Conductance (b) Susceptance

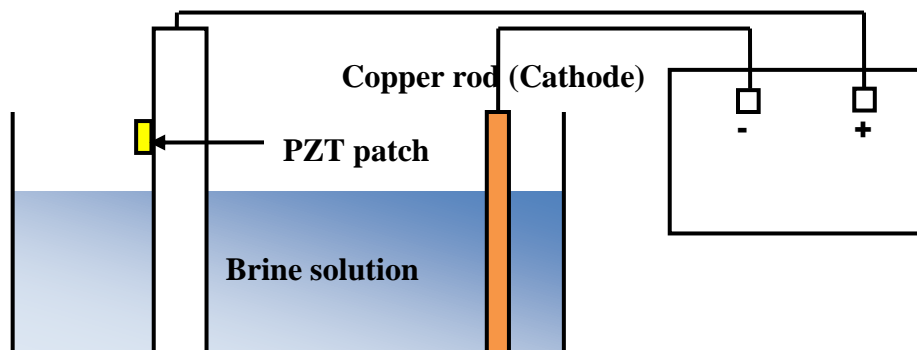


Figure 3.3 Accelerating corrosion set up

CHAPTER- 3 Diagnosis of Chloride Induced Corrosion in Bare Steel Bars

Fig. 3.4 shows the condition of one of the steel bar before and after accelerated corrosion. As clearly visible from the figure, substantial corrosion has occurred in the bar after eight hours of the application of the constant current. The cross section of the bar has reduced considerably (see Fig. 3.4b) in the region which has been dipped inside the brine solution. While the steel bar is placed in the brine solution, care has been taken such that the PZT patch is always above the surface of the solution. The distance of the affected region (where corrosion occurred) from the patch was within its zone of influence, which typically extends to about 1m in such 1D structures (Park et al., 2000b).

The conductance signatures obtained from the sensor are shown in Fig. 3.5 for all the specimens. The variation of G (the real part of admittance) of the PZT patches, bonded to the bare steel bar specimens is considerable after subjected to eight hours of accelerated corrosion and the signatures can be observed to change substantially for all the three specimens. The change in the conductance signature can be seen in light of degradation of mass, stiffness and/or damping of the steel bar due to the exposure to accelerated corrosion for eight hours.



Figure 3.4 Condition of specimens (a) Pristine specimen (b) Corroded specimen

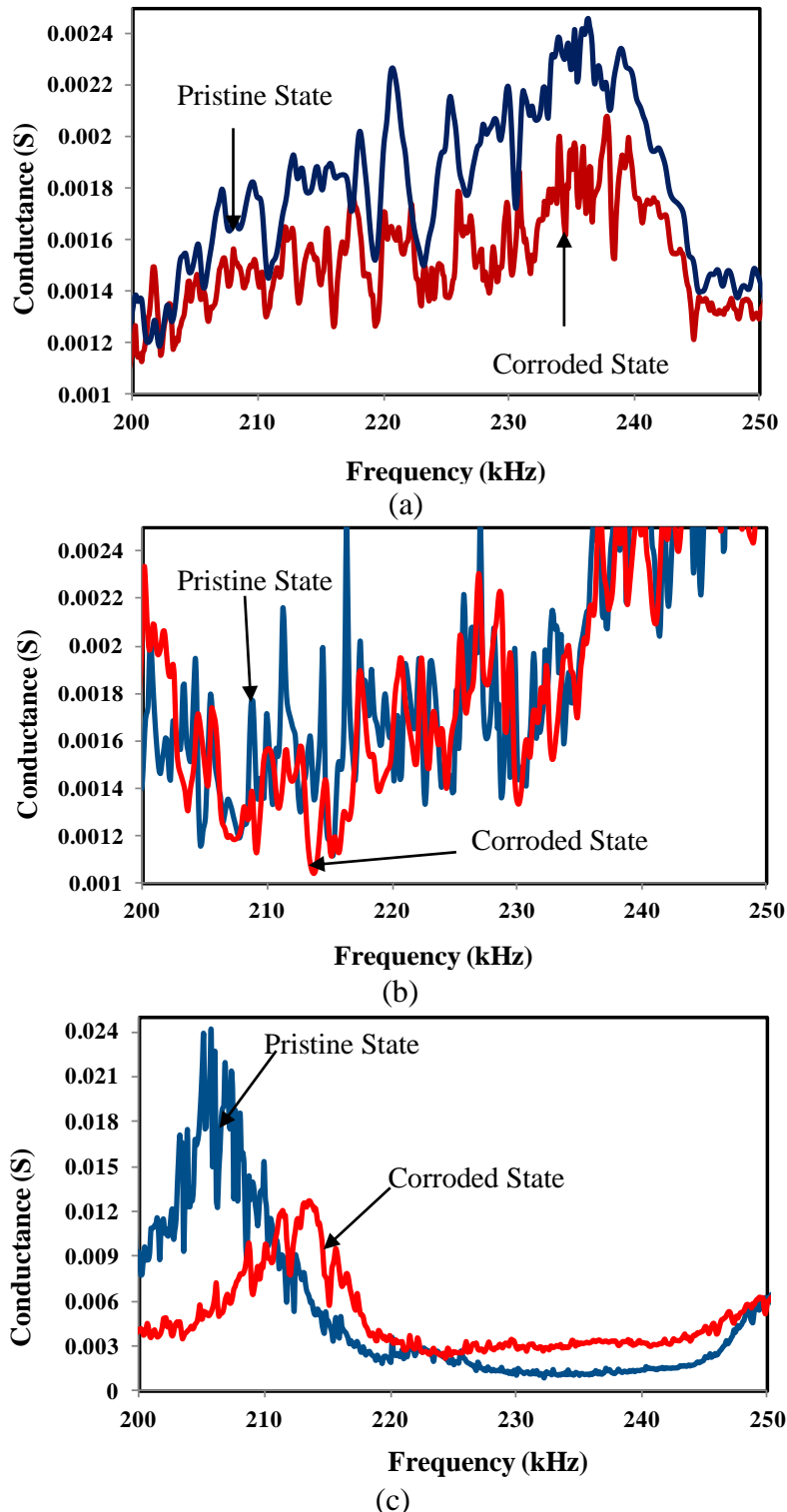


Figure 3.5 Variation of the conductance signature due to accelerated corrosion exposure
 (a) Specimen 1 (b) Specimen 2 (c) Specimen 3

However, as observed in the figures, the conductance signature varies from specimen to specimen due to the fact that the signature depend on number of factors such as bonding conditions of the patch, local surface and the variability of the PZT parameters. From the marked difference in the signature, it can be concluded that the mechanical impedance has changed due to corrosion. This happens because corrosion changes the mass, stiffness, and/or damping properties of the bar, which in turn causes the conductance signature to change in accordance with Eq. (2.21). The next section focuses on quantification of the corrosion induced deterioration.

3.5 DAMAGE QUANTIFICATION

Described below are some of the computational techniques which can be used for the comparison of two signatures, one of which is the baseline signature of the healthy structure and the other one is the signature after an unknown damage.

3.5.1. Root Mean Square Deviation (RMSD)

The RMSD index is defined as (Giurgiutiu and Rogers, 1998; Giurgiutiu et al., 1999) as

$$RMSD = \sqrt{\frac{\sum_{i=1}^N (G_i - G_i^0)^2}{\sum_{i=1}^N (G_i^0)^2}} \times 100 \quad (3.9)$$

where G_i is the conductance of the PZT patch at any stage during the test and G_i^0 is the baseline value (in pristine condition), i representing the frequency index (100 to 300 kHz).

3.5.2 Signature Assurance Criteria (SAC)

Let, $u = [u_i]$, $i = 1, 2, 3, \dots, N$ be a reference signature obtained from an healthy structure, and $v = [v_i]$, $i = 1, 2, 3, \dots, N$ be the second signature obtained from the same structure after an unknown level of degradation has occurred, then SAC value is given by

$$SAC(u, v) = \frac{|u^T \cdot v|^2}{u^T \cdot u \cdot v^T \cdot v} \quad 0 \leq SAC \leq 1.0 \quad (3.10)$$

SAC = 1.0 implies that u and v are identical and a value of SAC=0 implies that the two are totally uncorrelated (Bhalla, 2001).

3.5.3 Waveform Chain Code (WCC) Technique (Bhalla, 2001)

Let u and v be two signatures as defined above. WCC uses the summation of the absolute differences between two slopes and two curvatures (Samman and Biswas, 1994 a and b).

The slope at a point is given by $S_i = u_i - u_{i-1}$ where $i = 2, 3, 4, \dots, N$ (3.11)

The relative Slope can be expressed as, $S_i^r = \frac{S_i}{S_{\max}}$ (3.12)

This can be converted to a scaled slope by scaled relative slope,

$$S_i^{sr} = 50S_i^r (-50 \leq C_i^{sr} \leq 50) \quad (3.13)$$

Similarly, Scaled Relative Curvature, which is the derivative of slope, can be expressed as

$$C_i^{sr} = \frac{S_i^{sr} - S_{i-1}^{sr}}{2} (-50 \leq C_i^{sr} \leq 50) \quad (3.14)$$

The two signatures, u and v , as defined above, may be compared by calculating their Slope Differential Values (SDV) and Curvature Differential Values (CDV) as defined below

Slope Differential Value, $S_i^{dv} = |S_i^{rs,v} - S_i^{rs,u}|$ (3.15)

Curvature Differential Value, $C_i^{dv} = |C_i^{rs,v} - C_i^{rs,u}|$ (3.16)

Larger value of SDV or CDV at a point implies a significant difference between the two signatures in the neighbourhood of the point. Their values may range from 0 to 100%.

3.5.4 Adaptive Template Matching (ATM)

Two signatures u and v are considered identical if the following two criteria are satisfied (Samman and Biswas, 1994 a and b)

$$(a) (1 - \beta) u_i \leq v_i \leq (1 + \beta) u_i \quad (3.17)$$

$$(b) u_i > \Delta \text{ and } v_i > \Delta \quad (3.18)$$

in which, β is the percent tolerance on the magnitude and Δ is the threshold of the magnitude.

$$\Delta = \partial X \max(u_i, v_i) \quad (i = 1, 2, 3, \dots) \quad (3.19)$$

where $0 \leq \partial \leq 1$

Given u , v , and Δ , the technique calculates the minimum tolerance value β .

These damage metrics, as described above, can be used to mathematically quantify the damage while reducing the deviation in admittance data to single scalar value. For preliminary investigations, the RMSD metric has been widely used because it is an

established statistical metric to quantify damage (Giurgiutiu and Rogers, 1998; Giurgiutiu et al., 1999). The variation of the RMSD index can be studied in light of the degradation of actual stiffness of the specimen with the increase in corrosion.

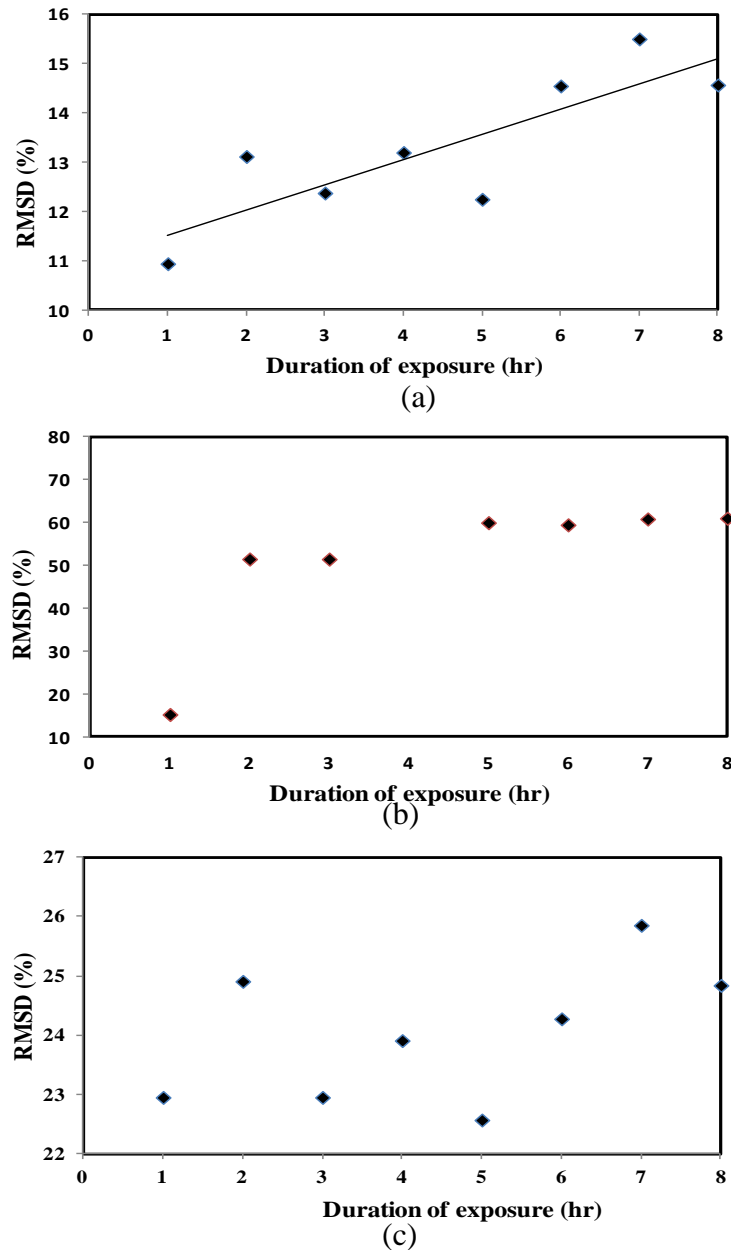


Figure 3.6 Variation of RMSD (a) Specimen 1 (b) Specimen 2 (c) Specimen 3

Fig. 3.6 shows the variation of the RMSD indices of the three specimens as a function of the duration of accelerated corrosion exposure. For specimen 1, the RMSD index appears to follow a crudely linear trend (Fig. 3.6a). For specimen 2, the RMSD increases abruptly in between first and second hour and then exhibits a weakly linearly increasing trend (Fig. 3.6b). However, for Specimen 3 (Fig. 3.6c), essentially a scatter of values are observed.

Although all the three bars were identically affected (since the specimens as well as the exposure conditions were identical), the overall magnitude and the variation of the RMSD index differs significantly from specimen to specimen. Hence, it does not provide damage related information regarding the corrosion severity consistently. This is not unexpected since RMSD is only a statistical quantifier. It was also reported in the literature that the raw conductance signatures as well as the RMSD index are not very dependable as they only provide a qualitative information about the damage (Bhalla et al., 2012).. To gain further insight into the phenomenon, structural parameters were extracted from the impedance spectrum. The next section performs detailed analysis to extract inherent system parameters and identify the one showing consistent variation with advancement of corrosion.

3.6 ANALYSIS OF STRUCTURAL MECHANICAL IMPEDANCE

EXTRACTED FROM ADMITTANCE SIGNATURE

The electro-mechanical admittance (given by Eq. 2.21) can be decomposed into active and passive parts as (Bhalla, 2004)

$$\bar{Y} = \underbrace{4\omega j \frac{l^2}{h} \left[\bar{\varepsilon}_{33}^T - \frac{2d_{31}^2 \bar{Y}^E}{(1-\nu)} \right]}_{\text{Passive Part}} + \underbrace{\frac{8\omega d_{31}^2 \bar{Y}^E l^2}{(1-\nu)} \left(\frac{Z_{a,eff}}{Z_{s,eff} + Z_{a,eff}} \right) \bar{T}j}_{\text{Active Part}} \quad (3.20)$$

or

$$Y = Y_P + Y_A \quad (3.21)$$

The passive part solely depends upon the parameters of the PZT patch and is independent of the host structure. The host structure's parameters appear in the active part only, in the form of the structural impedance, $Z_{s,eff}$. Using the computational procedure outlined by Bhalla and Soh (2004 a, b), the real and the imaginary components (x and y , respectively) of the structural impedance i.e., $Z_{s,eff}$ can be determined as

$$Z_{s,eff} = x + yj \quad (3.22)$$

Where

$$x = \frac{M(x_aR - y_aS) + N(x_aS + y_aR)}{M^2 + N^2} - x_a \quad (3.23)$$

$$y = \frac{M(x_aR + y_aS) - N(x_aS - y_aR)}{M^2 + N^2} - y_a \quad (3.24)$$

$$M = \frac{B_A h}{4\omega K l^2} \text{ and } N = -\frac{G_A h}{4\omega K l^2} \quad (3.25)$$

and

$$R = r - \eta t, S = t + \eta r, K = \frac{2d_{31}^2 \bar{Y}^E}{(1-\nu)} \quad (3.26)$$

where, G_A and B_A are the real and the imaginary components of the active admittance, computed from

$$\bar{Y}_A = \bar{Y} - \bar{Y}_P \quad (3.27)$$

and $Z_{s,eff} = x_a + y_a j$ is the effective mechanical impedance of the PZT patch. This procedure enables the determination of the drive point mechanical impedance of the structure, $Z_{s,eff}$, at a particular angular frequency ω from the measured data, without demanding any *a priori* information governing the phenomenological nature of the structure.

Depending upon the variation of ‘ x ’ and ‘ y ’ with the frequency and the associated values, the inherent elements (stiffness ‘ k ’, mass ‘ m ’ and Damping ‘ c ’) making the host structural system can be identified. The experimental signature of the PZT patches bonded to the three specimens consists of G and B over 100-300 kHz range. The mechanical impedance of the host structure (here steel rebars) was obtained at each frequency using the above computational procedure. A close examination of the extracted impedance components (x and y) in the frequency range 100-110 kHz of the healthy state revealed that the system behaviour is similar to that of a *Kelvin-Voigt* system i.e. a parallel arrangement of a spring element (k) with a damper (c), as shown in Fig. 3.7, for which the real and imaginary components are given by Hixon (1998) as

$$x = c \quad \text{and} \quad y = -\frac{k}{\omega} \quad (3.28)$$

Within the frequency range 100-110 kHz, x was found to possess more or less a constant positive value and y a negative value with magnitude decreasing with frequency, which is the characteristic of the *Kelvin-Voigt* system as illustrated in Fig. 3.8 (a, b and c) respectively for all the three specimens.

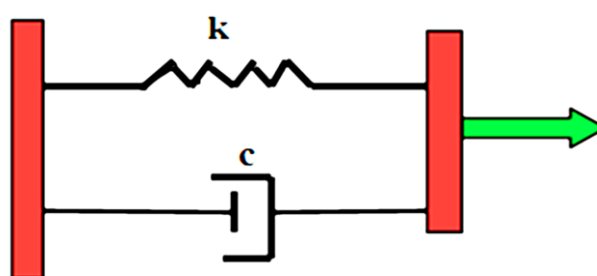


Figure 3.7 Kelvin-Voigt system (Hixon 1998)

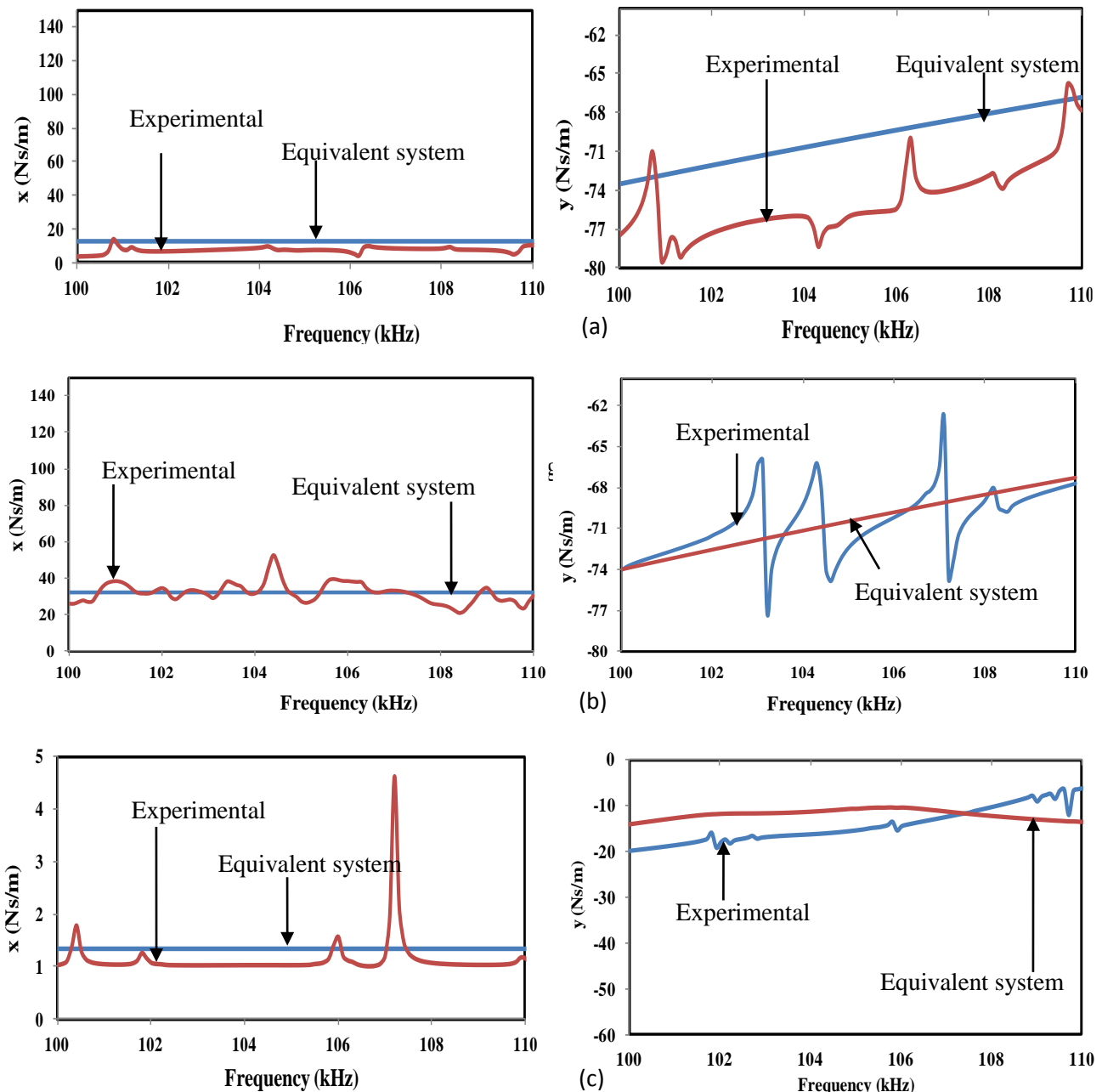


Figure 3.8 Comparison of experimental plots x and y with those of identified system
 a) Specimen 1 (b) Specimen 2 (c) Specimen 3

For *Kelvin-Voigt* system, the value of ' k ' equal to the slope of the plot of y with ω^{-1} (Eq. 3.28) which should be a straight line as illustrated in Fig. 3.9 for all the specimens.

CHAPTER- 3 Diagnosis of Chloride Induced Corrosion in Bare Steel Bars

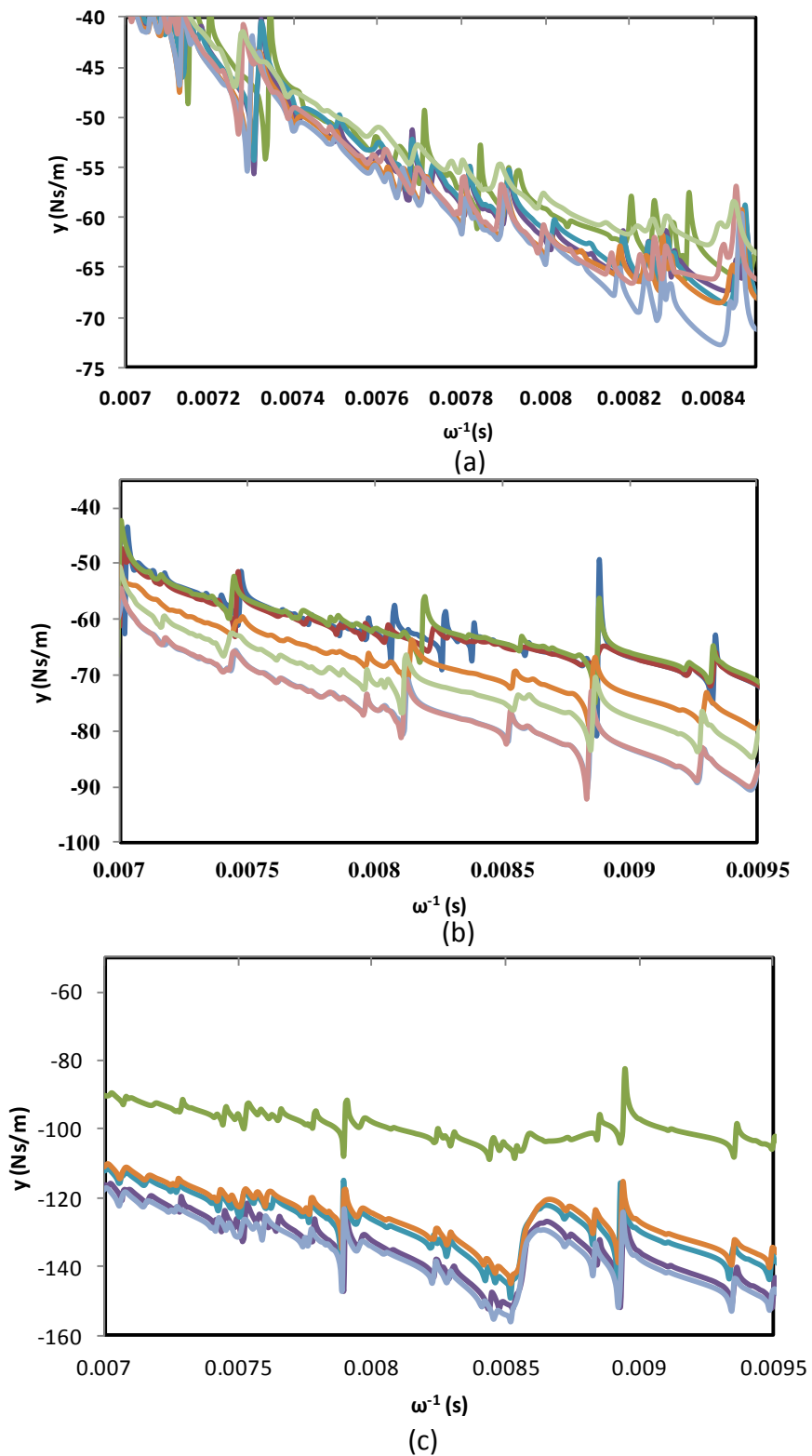


Figure 3.9 variation of ' y ' with ω^I

(a) Specimen 1 (b) Specimen 2 (c) Specimen 3

A very consistent observation is that with the advancement of corrosion, the slope of the curve decreases consistently, this is much more consistent than the trend of the RMSD indices shown in Fig. 3.6.

Using Eq. (3.28), the values of k and c were determined for all the specimens after each hour of accelerated corrosion. Fig. 3.10 (a, b and c) display the effect of corrosion severity (in terms of number of hours of application of the constant current) on the identified equivalent structural parameters (c and k). With corrosion progression after an exposure of eight hours, the damping can be observed to increase by about 41%, 38% and 60% and the identified stiffness can be observed to reduce by about 19%, 16% and 29% for the specimens 1, 2 and 3 respectively, after an exposure time of eight hours of accelerated corrosion. Compared to the variation of the RMSD index (see Fig. 3.6), this observed variation in identified parameters is much more agreeable.

The major phenomenon accompanying the corrosion process is the loss of mass occurring on account of thinning of section as observed in Fig. 3.4. Although the *Kelvin-Voigt* system based analysis showed consistent results, the identified system (parallel spring-damper combination) does not include mass element, which is expected to play significant role due to the loss of mass associated with corrosion process. To identify a system consisting of mass, a closer observation of frequency range 250 to 300 kHz showed that the system behaviour was similar to a series combination of spring, damper and mass such as the one shown in Fig. 3.11(a).

The analytical plots of ‘ x ’ and ‘ y ’ obtained by the equivalent parameters match well with their experimental counterparts, for specimen 1 as shown in Fig. 3.11 (b and c). Specimen 2

CHAPTER- 3 Diagnosis of Chloride Induced Corrosion in Bare Steel Bars

also followed a similar trend in the frequency range 250-300 kHz. However, specimen 3 was exception and was therefore not considered.

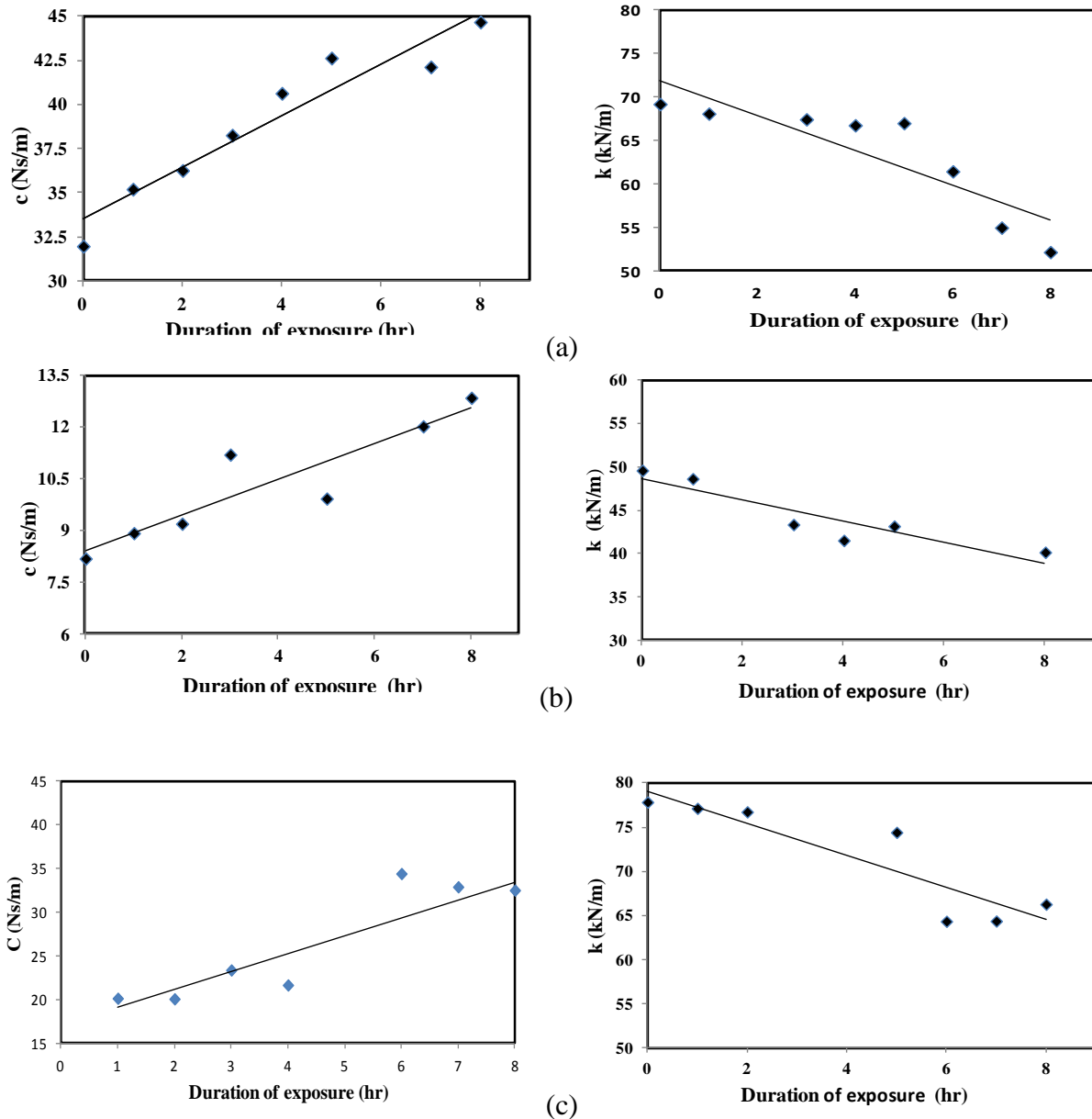


Figure 3.10 Variation of extracted system parameters (stiffness and damping)
 (a) Specimen 1 (b) Specimen 2 (c) Specimen 3

CHAPTER- 3 Diagnosis of Chloride Induced Corrosion in Bare Steel Bars

For this combination, the system parameters are related to and as (Hixon, 1998).

$$x = \frac{c^{-1}}{c^{-2} + \left(\frac{\omega}{k} - \frac{1}{\omega m}\right)^2} \quad \text{and} \quad y = \frac{-\left(\frac{\omega}{k} - \frac{1}{\omega m}\right)^2}{c^{-2} + \left(\frac{\omega}{k} - \frac{1}{\omega m}\right)^2} \quad (3.29)$$

The angular frequency at which $y=0$ is denoted by ω_0 . Using Eq. (3.29), the system parameters can be determined, by algebraic manipulations, as

$$m = \frac{k}{\omega_0^2} \quad (3.30)$$

$$k = -\frac{x^2 + y^2 (\omega^2 - \omega_0^2)}{\omega y} \quad (3.31)$$

and

$$c = \frac{x^2 + y^2}{x} \quad (3.32)$$

The system parameters i.e. equivalent spring constant, equivalent mass and equivalent damping constant were determined for specimens 1 and 2 using the Eqs. (3.30 to 3.32) after each hour of corrosion exposure. The equivalent stiffness was found to reduce by 24% and 20%, the equivalent mass reduced by 24% and 19% and the equivalent damping increased by 24% and 20% for specimen 1 and 2 respectively after eight hours of exposure. The variations of the system parameters with increasing corrosion exposure for this system are shown in Fig.3.12. For this model, the relative reduction in the equivalent mass is agreeable between the two specimens. During the experiment, the actual mass loss of the specimen was also measured to correlate with the PZT identified equivalent mass.

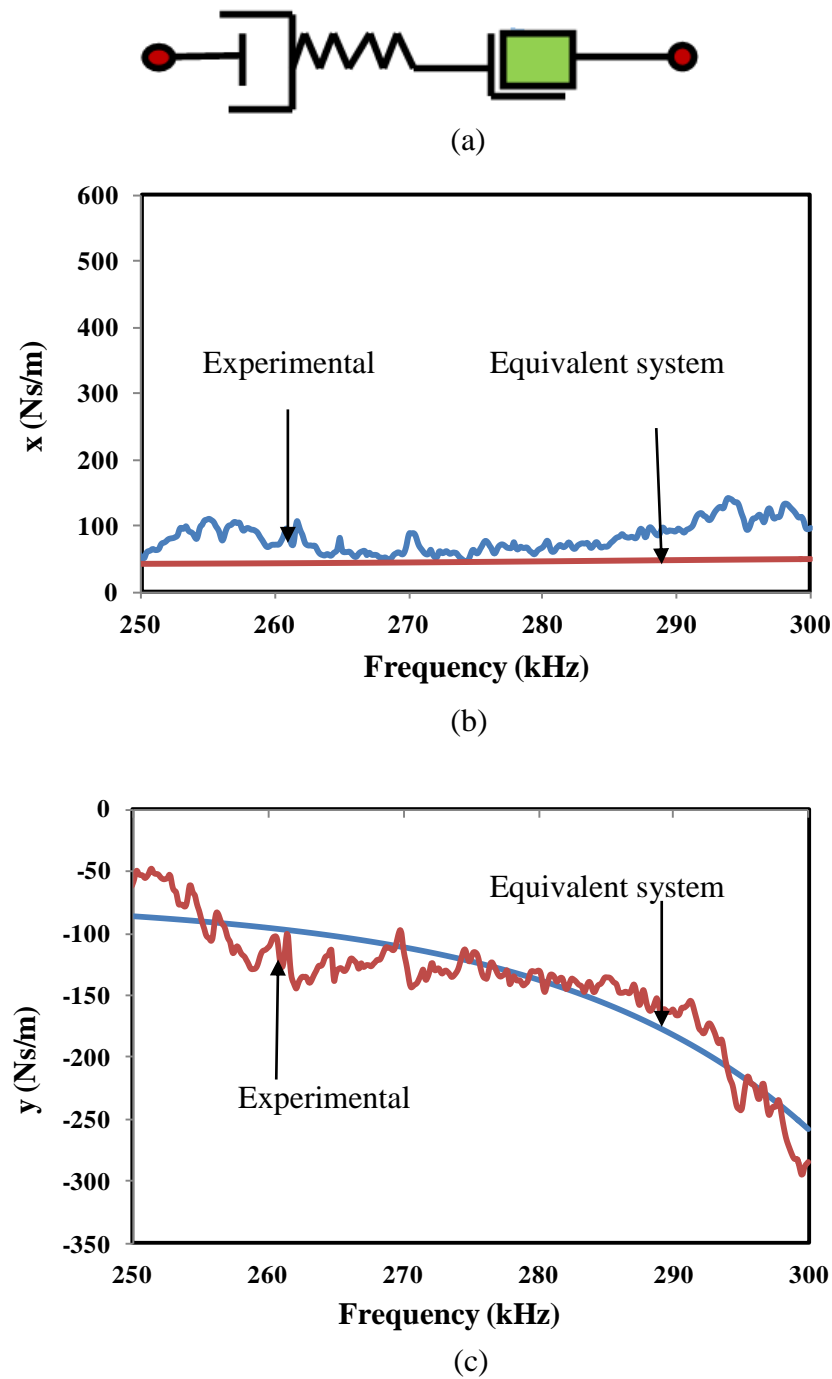


Figure 3.11 Equivalent System parameters (a) Equivalent system (series combination of spring-damper and mass) (b) x vs f of specimen1 (c) y vs f of specimen 1

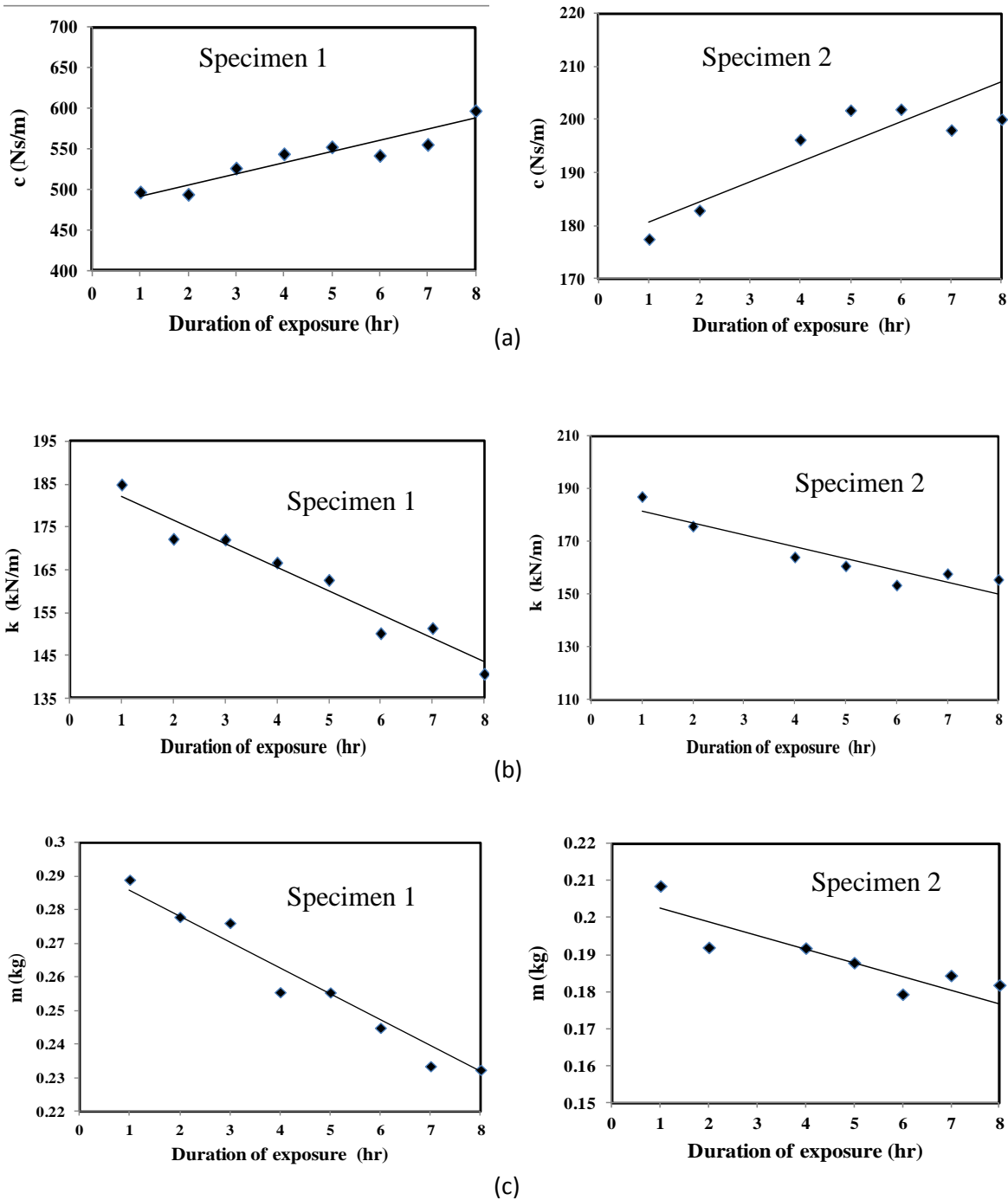


Figure 3.12 Variation of extracted system parameters (a) Equivalent damping of specimen 1 and 2 (b) Equivalent stiffness of specimen 1 and 2 (c) Equivalent mass of specimen 1 and 2

Fig.3.13 shows a plot of the mass loss of the specimens measured with the progression of corrosion. This was measured directly using a weighing balance by removing the specimens from the accelerated corrosion after each hour.

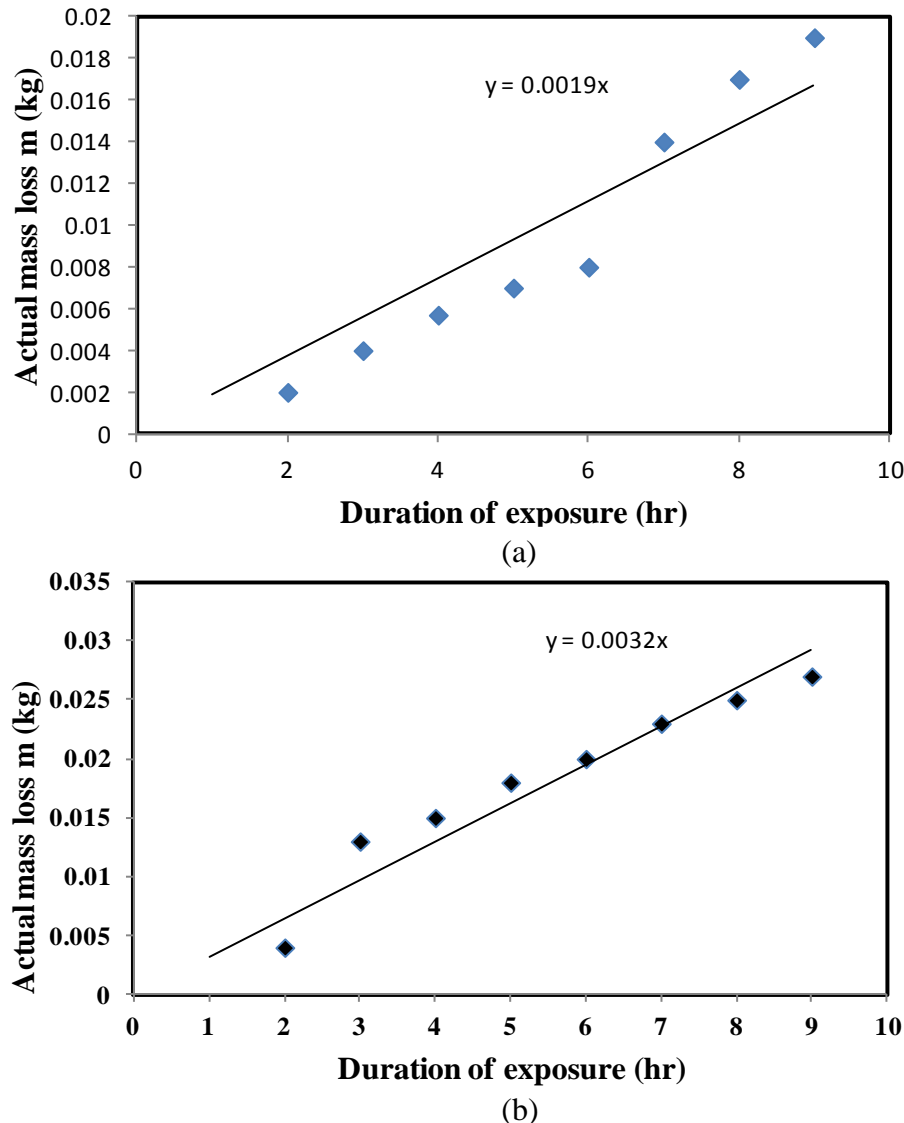


Figure 3.13 Variation of actual mass loss with accelerated corrosion exposure
 (a) Specimen 1 (b) Specimen 2

For purpose of quantification, mass loss can be expressed in non-dimensional form as

$$\Delta m = \frac{\delta m}{m} \quad (3.33)$$

where m is the original mass of the specimen and δm is the loss of mass. Here, both the actual and the PZT identified mass can be substituted. To correlate the mass loss identified by PZT (using Eq. 3.30) with the actual mass loss measured directly, a non-dimensional model is derived as

$$\left(\frac{\delta m}{m} \right)_{actual} = \lambda_{mb} \left(\frac{\delta m}{m} \right)_{PZT} \quad (3.34)$$

Where λ_{mb} is a constant relating the non-dimensional PZT based mass loss with actual mass loss for bare steel bar. Fig. 3.14 shows that $\left(\frac{\delta m}{m} \right)_{PZT}$ determined from the PZT identified mass correlates well with that based on the actual mass loss. Thus, the PZT identified mass can provide a reasonable estimation of the actual mass loss of the specimen. Based on the data averaged over the two patches for the two specimens, the value of λ_{mb} is found to be equal to 4.974. This non-dimensional mass model of steel bars helps to find out the actual mass of the specimen without the need of actual mass.

The experimental results were also verified by using conventional half cell potential (using ACM field machine). When the PZT identified mass loss changed from 0.15 kg to 0.21 kg, the potential reading changed from -501 mV to -394 mV for specimen 1 which has the probability of severe corrosion (ASTM C876, 1999).

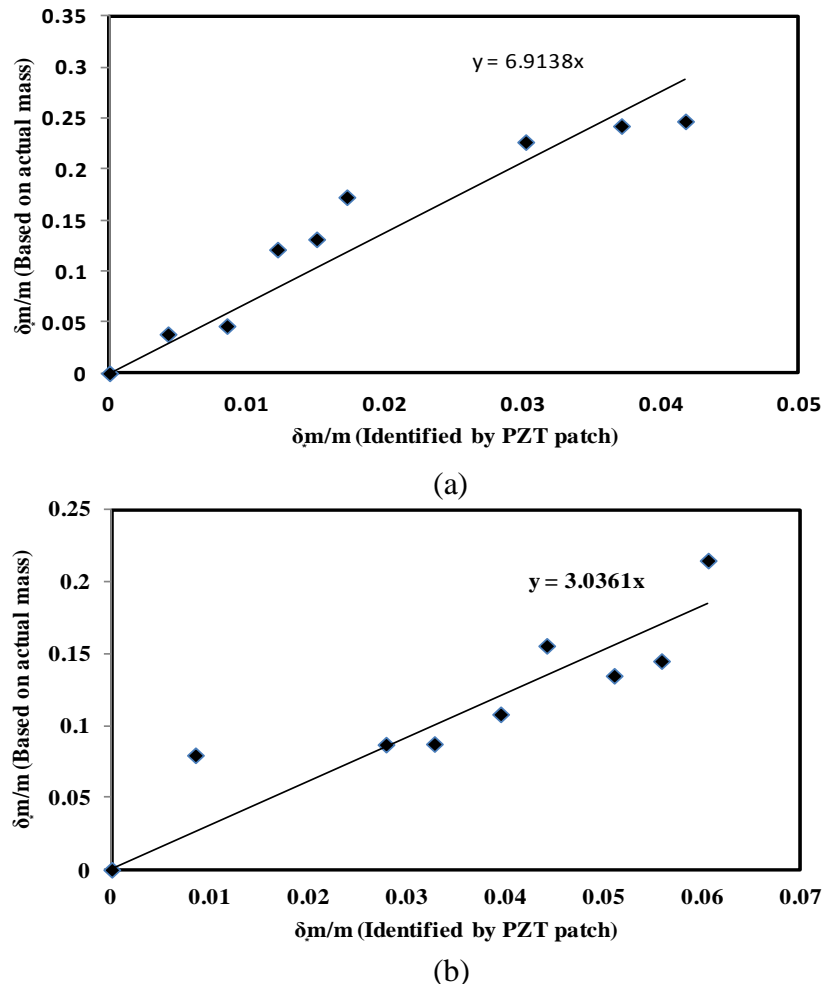


Figure 3.14 Correlation between loss of actual mass with PZT identified mass loss
 (a) Specimen1 (b) Specimen 2

Eq. (3.34) can thus be directly used, with no requirement of determining the absolute mass of the specimen as it gives the loss of mass directly.

The approach is more reliable as compared to the conventional potential measurement values because the value of the potential difference depends on various factors such as type of electrode used, concrete porosity etc. In addition, for real-life structures, the potential measurement of steel rebar embedded in concrete cannot be measured directly at the interface of concrete/ rebar due to the presence of concrete cover. Further, the potential

measurements do not provide quantitative information on the actual corrosion rate of rebars. Whereas, from the derived non-dimensional mass model corrosion rate can be determined this is covered in detail for rebar corrosion in RC structures in the next chapter. Moreover, the potential measurements need to be interpreted in the context of complementary data from the concrete structures by specialists or skilled engineers. The approach presented in this chapter, however is more practical, direct and consistent.

3.7 CONCLUDING REMARKS

This chapter presented a new corrosion measurement approach for bare steel bars using the EMI technique through the use of surface bonded PZT patches based on the extracted structural parameters from the impedance spectrum. Better response of ' k ' and ' m ' is observed as compared to the RMSD index as it makes use of real as well as imaginary components of admittance signature for extracting damage sensitive equivalent structural parameters. This approach based on equivalent structural parameters is an improvement over the statistical indicators, such as RMSD, which fail to provide meaningful indication of the loss of stiffness and mass of the specimens. Further, the identified mass follows a very consistent behaviour with corrosion progress and the relative loss of the identified mass correlates well with the relative loss of actual mass of the specimens. The empirical correlation derived from the PZT patches can be utilized in corrosion detection of rebars in real-life RC structures, where they are not exposed for direct visual check. The next chapter extends the study to rebars embedded inside concrete.

CHAPTER- 4
DEVELOPMENT OF CORROSION ASSESSMENT MODEL
FOR REBARS EMBEDDED IN RC STRUCTURES

4.1 INTRODUCTION

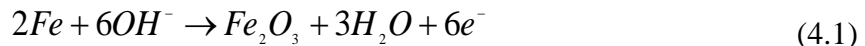
In Chapter 3, as a preliminary investigation, a new empirical model was developed to assess the corrosion in bare steel bars based on the extracted structural parameters from the impedance spectrum of surface bonded PZT patches. This chapter extends proposed method to the rebars embedded in concrete and presents corrosion assessment models which can be used in real life corrosion monitoring of RC structures.

Comprehensive tests were performed on RC specimens under accelerated chloride exposure until the specimens were cracked due to corrosion in order to calibrate the identified system parameters (equivalent stiffness and mass) to the actual parameters of the structure.

4.2 REBAR CORROSION IN REINFORCED CONCRETE STRUCTURES

As pointed out in Chapters 1 and 2, corrosion of steel rebars in concrete is probably the most serious durability problem of RC structures in the modern times. The main corrosive agents i.e., the chlorides can ingress into concrete from several sources. They can be cast into the concrete due to use of ground water/seawater in the mix or contaminated aggregates. They may also diffuse into the concrete due to sea salt spray and direct seawater wetting or de-icing salts. These chlorides diffused into concrete reduce the alkalinity of the pore solution thereby initiating corrosion. The durability of steel within concrete depends upon the alkalinity of the pore solution, typically at $\text{pH} > 13$, (high degree of alkalinity) steel

passivates in the presence of oxygen by the formation of a surface layer of Fe_2O_3 as given below.



However, the degree of protection provided by concrete due to the formation Fe_2O_3 layer may be considerably reduced when the RC structure is exposed to de-icing salts, when immersed in seawater, or due to high chloride content of water used in concrete mix, through the penetration of chlorides into the hardened concrete and reaching the rebar. Once they reach the rebar, passivation provided by the alkalinity of the cement fails to protect it from corrosion, leading to the formation of rust on the steel surface.

Fig. 4.1 illustrates the basic reactions of corrosion. It may be noted that water and oxygen are needed at the cathode for corrosion to occur. The anodic and the cathodic reactions shown in Fig. 4.1 are only the first steps in the process of rust formation. However, a chain of reaction takes place where ferrous hydroxide becomes ferric hydroxide and then hydrated ferric oxide or rust, as given by Eqs. (4.2-4.4) (Broomfield, 2007).

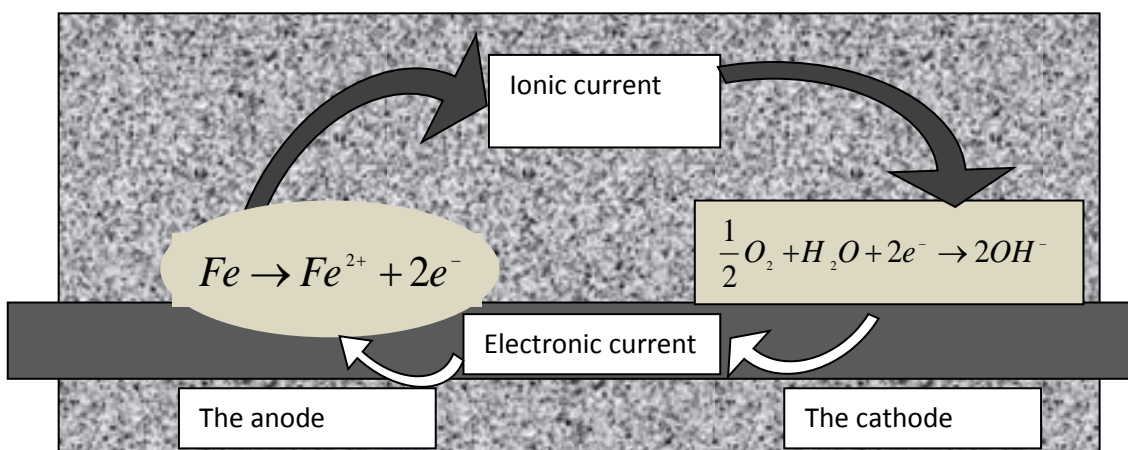
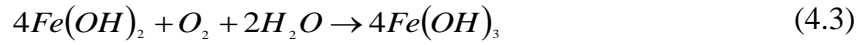


Figure 4.1 The anodic and cathodic reactions for corroding steel (Broomfield, 2007)

CHAPTER- 4 Development of Corrosion Assessment Model for Rebars Embedded in RC Structures



Ferrous hydroxide



Ferric hydroxide



Hydrated ferric oxide (rust)

The unhydrated ferric oxide has a volume of about twice that that of the steel. When it becomes hydrated, it swells even more and becomes porous. As a result, the volume at the steel/concrete interface increases to about six to ten times, as indicated in Fig. 4.2. This leads to the cracking and spalling that we observe as the usual consequence of corrosion of steel in concrete.

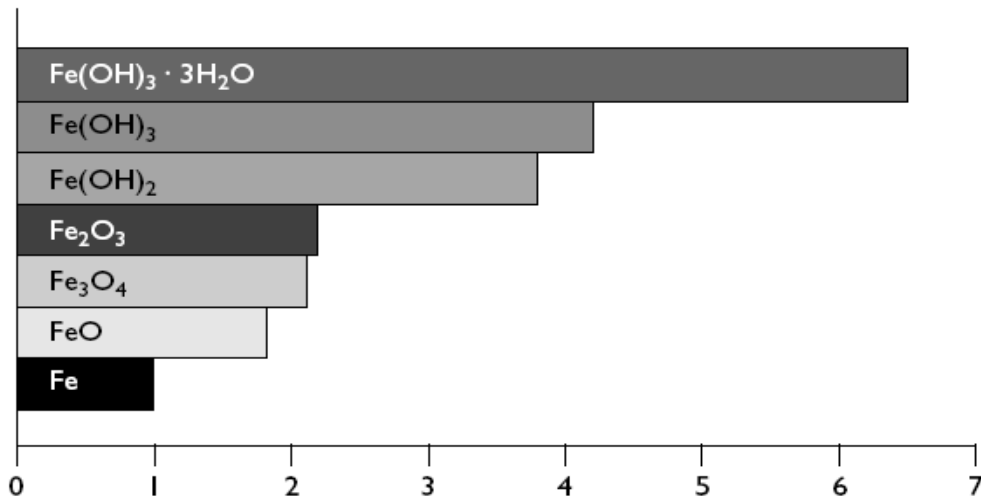


Figure 4.2 Relative volumes of iron and its oxides (Mansfield, 1981)

This chapter presents the results of the accelerated corrosion tests performed on five concrete cubes with embedded rebars. The assessment of corrosion has been done via the PZT patches surface bonded on the rebars, using the equivalent structural parameters identified by the patches. The corrosion assessment models are formulated based on the analysed data. While all the previous studies have concentrated on metal components, and employed the raw conductance signature for corrosion monitoring (as discussed in chapter 2), the study covered in this chapter focuses on corrosion in RC structures using the equivalent structural parameters extracted from the mechanical impedance, after filtering out the PZT parameters. The next section deals with the detailed experimental study, data acquisition, analysis and development of the corrosion assessment model based on the equivalent parameters.

4.3 SPECIMEN PREPARATION

In this investigative study, five RC cubes of M30 grade (as per IS 456, 2000), 150x150x150 mm in size, were cast along with 200 mm long, 16 mm diameter HYD rebar located centrally. The rebars were thoroughly cleaned with a wire brush prior to bonding the PZT at mid length as explained in Chapter 2. The concrete cube specimens were then cast with rebars placed centrally using OPC, fine aggregate of Zone 1 grading (as per IS 383, 1970) and crushed coarse aggregate of nominal size 10 mm. Table. 4.1 present the details of composition of the concrete mix. The standard moulds were filled with concrete in three layers, taking particular care in pouring the concrete to avoid damage to the PZT sensor. The concrete was compacted carefully using table vibrator, the specimens were demoulded after 24 hours of casting.

Table 4.1 Concrete mix design details

Materials/Parameters	Quantity
Water-cement ratio	0.4
Ordinary Portland Cement 53 Grade (kg/m ³)	500
Fine aggregate (kg/m ³)	570.5
Coarse aggregate (kg/m ³)	1062.2
Slump (mm)	100

After 28 days of curing, the wires soldered to the electrodes of the PZT patch were connected to the LCR meter as shown in Fig. 4.3. In this manner, the electro-mechanical admittance signature, were acquired in a frequency range of 50-400 kHz. A frequency interval of 100 Hz was used for each impedance measurement.

4.4 ACCELERATED CORROSION EXPOSURE ON CONDUCTANCE SIGNATURES

The accelerated corrosion experiments were performed on same lines as described in Chapter 3 for bare bars after a period of 28 days from the day of casting so as to rule out the simultaneous occurrence of both concrete curing and corrosion. Out of the five specimens, one specimen (number 5) was selected as the control specimen and was reserved for splitting during the test. Fig. 4.4 shows the initial baseline conductance spectrum of the PZT patches bonded to the rebars of the remaining four specimens (numbered 1 to 4), acquired after 28 days of curing, and before being subjected to accelerated corrosion. As can be observed in the figure, the conductance signatures vary from specimen to specimen.

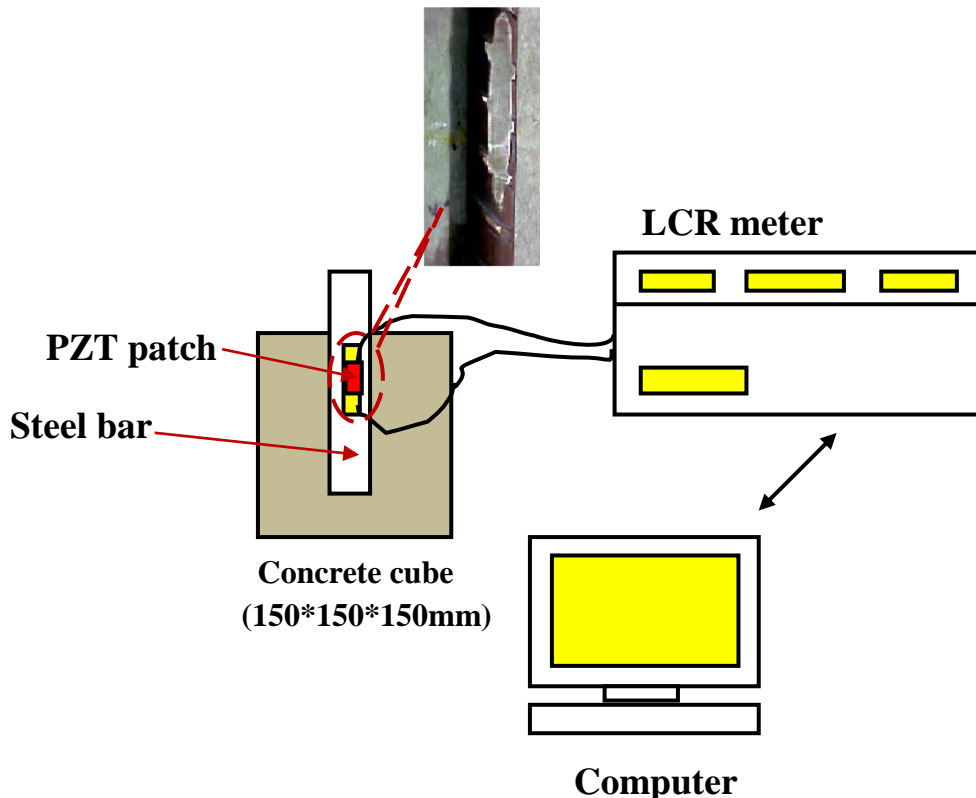


Figure 4.3 Specimen preparation and data acquisition setup

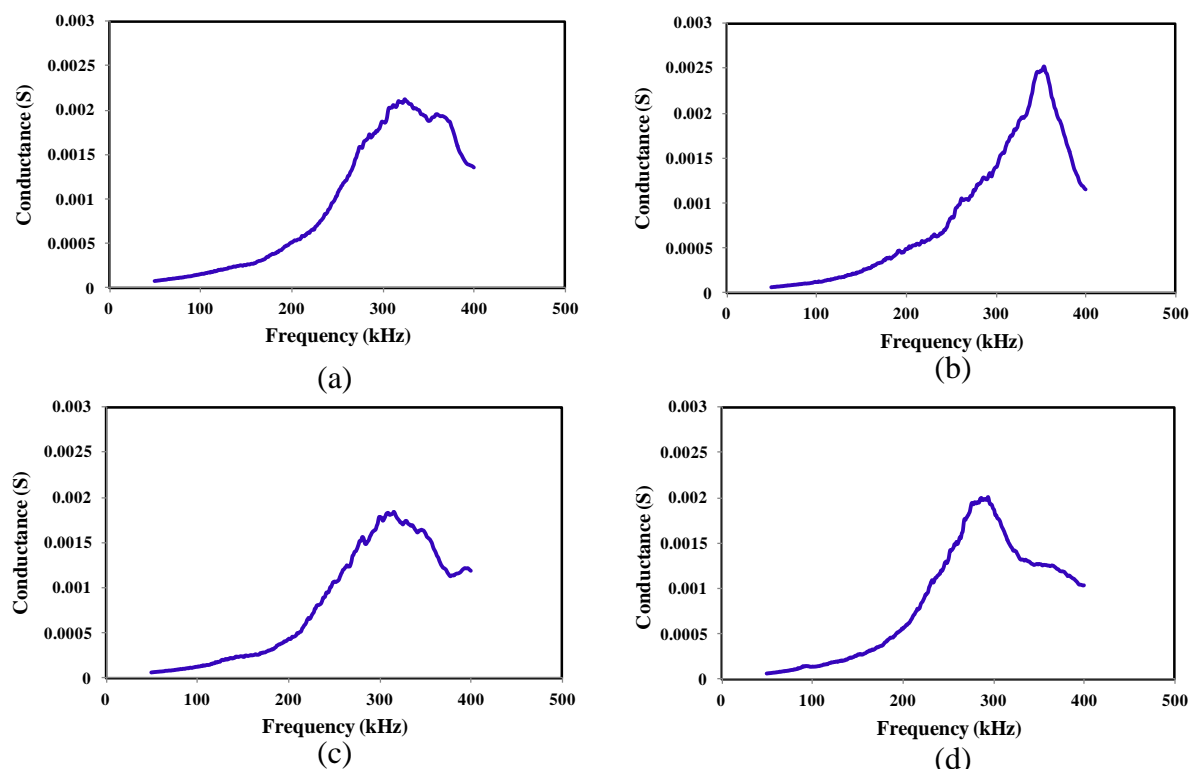


Figure 4.4 Baseline conductance signatures of PZT patches embedded in RC specimens
(a) Specimen 1 (b) Specimen 2 (c) Specimen 3 (d) Specimen 4

CHAPTER- 4 Development of Corrosion Assessment Model for Rebars Embedded in RC Structures

This is because a particular PZT patch monitors a limited area. There may be a variability of parameters associated with the patch, the surrounding concrete as well as the bonding conditions. In the EMI technique, it is the deviation in signature with respect to baseline signature, which is of greater importance than the baseline signature itself. In order to inflict a significant degree of corrosion to the rebars embedded in concrete in the limited available time, the corrosion was accelerated using the impressed current approach as described in Chapter 3 for a period of over four months (with an impressed current of $150 \mu\text{A}/\text{cm}^2$), until the cubes were cracked. During the exposure period, admittance signatures were acquired for each specimen at regular intervals. Before any signature acquisition, the cubes were taken out of the brine solution, wiped clean of water, and dried in running fan for 30 minutes.

After 45 days of exposure, accumulation of rust was observed on the surface of all the specimens. Figs. 4.5 (a and b) show the condition of specimen 5 (reference specimen) in the pristine state and after accelerated chloride exposure of 45 days. To examine the condition of the concrete and the rebar inside it, the specimen was cut open at 45 days as shown in Fig. 4.5 (c). The corrosion initiation is clearly visible as the red rust, in both the steel rebar as well as in the concrete at the steel/concrete interface. As apparent from the figures, it can be concluded that the corrosion had already initiated by the 45th day. After this observation, the other specimens (numbered 1-4) were continued in the accelerated corrosion environment until cracks were developed on the surface of the cubes.

Substantial cracks appeared in all the RC cubes after 120 days of exposure, as shown for typical specimen1 in Fig. 4.6 (a). This happened due to the accumulation of the corrosion products, creating an expansive stresses exceeding the tensile strength of concrete. To

examine the condition of the rebar and the concrete inside the specimen, all the remaining specimens (1 to 4) were split open and the rebars were removed to carry out the gravimetric mass loss measurements. Figs. 4.6 (b and c) show the condition of the rebar and the surrounding concrete for a typical specimen 1 split open after 120 days.

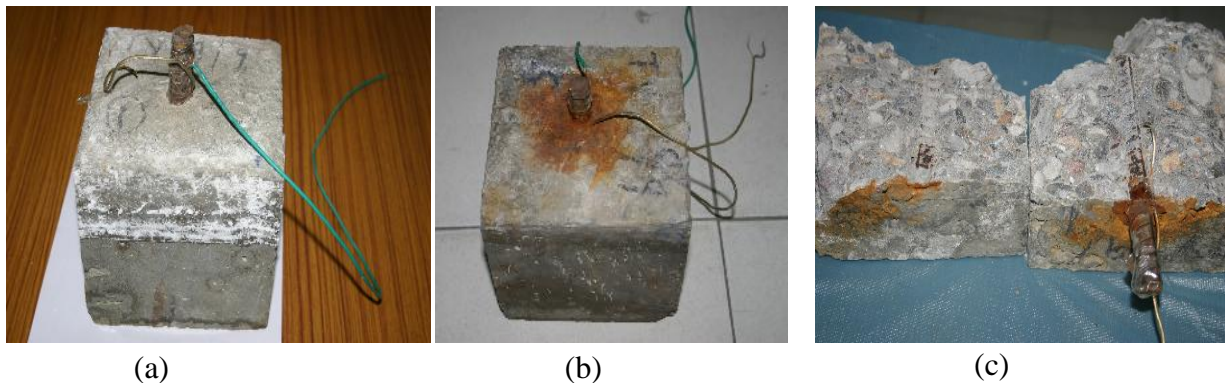


Figure 4.5 Condition of RC specimen 5
(a) Pristine state (b) After 45 days (c) After split open at 45 days

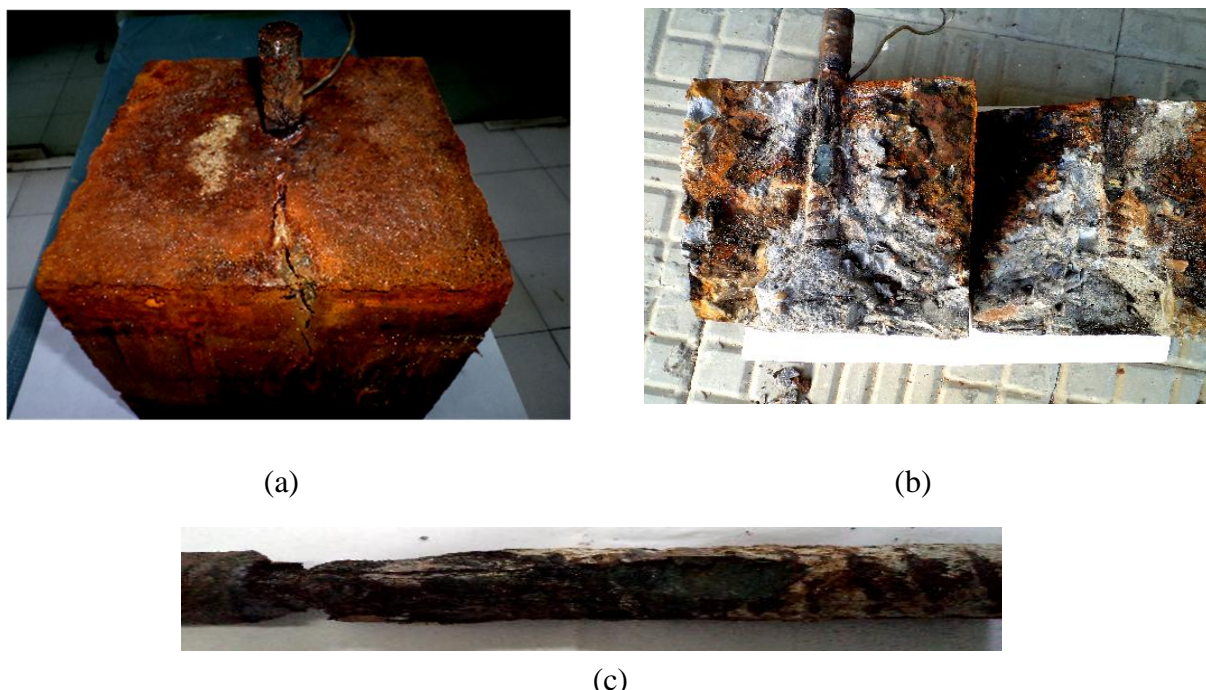


Figure 4.6 Condition of specimen 1 after 120 days of accelerated corrosion
(a) Cracked specimen (b) Cracked specimen after splitting (c) Corroded bar

On comparing the condition of the concrete and the rebar for 45 and 120 day exposure periods, it can be commented that the corrosion reached an alarming level at 120 days. The level of bar reduction in the embedded region is typically far greater than that observed on the rest of the bar. Most of the free region (projecting above the concrete) showed no sign of reduction in the cross-section due to corrosion. Another observation is that the severity of corrosion is non-uniform (i.e., uneven surface topography) along the bar length in all the specimens. The upper embedded region of the bar has greater reduction of the cross-section than the bottom region, as apparent in Fig. 4.6 (c).

From Eq. (2.26), as described in Chapter 2, when the properties of the host structure are altered, the mechanical impedance of the structure gets changed, resulting in deviation of signature. Any changes in the conductance signature, such as frequency and magnitude of the peaks, are attributed to the changes in the mechanical impedance of the structure. In order to monitor the changes in the RC cubes during the accelerated corrosion, the shifts in the magnitude and the frequency of the conductance signature were tracked at the main resonance peak.

Figs. 4.7 to 4.10 show the acquired conductance signature of the PZT patches bonded to the four specimens during the accelerated corrosion period of 120 days. As seen from the figures, the peaks of the conductance signature have reduced considerably during the corrosion process. The reduction in the magnitude of the peaks is attributed to increase of the damping at the rebar concrete interface due to the formation of corrosion products and also due to the associated cracking in the concrete.

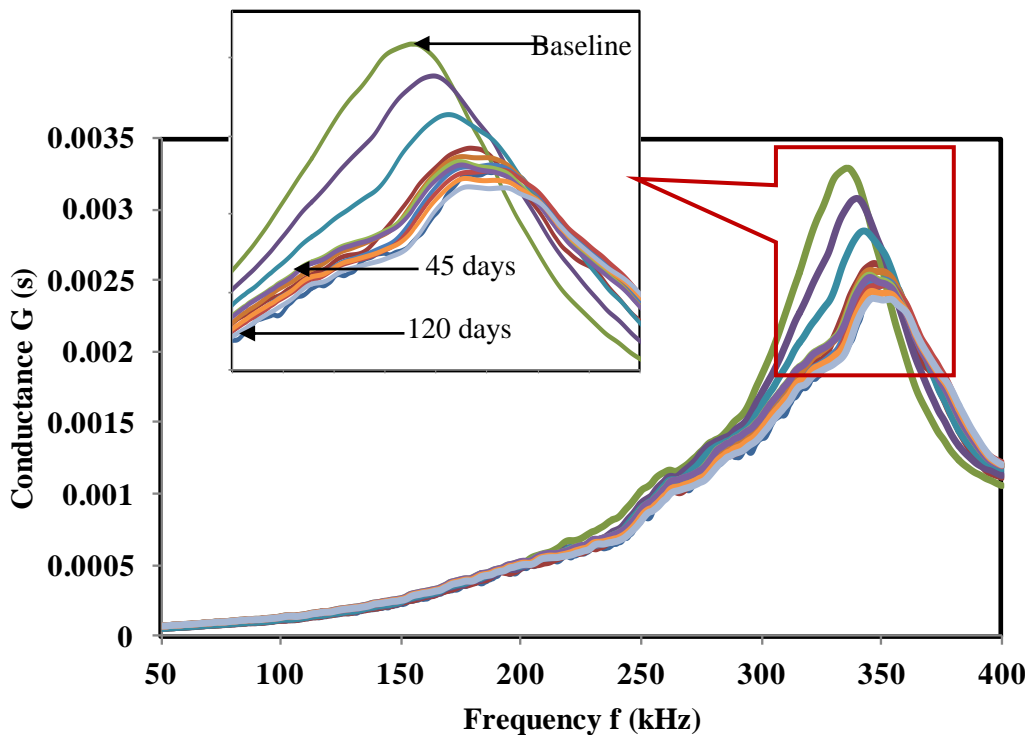


Figure 4.7 Variation of conductance signatures of specimen 1 during accelerated corrosion process

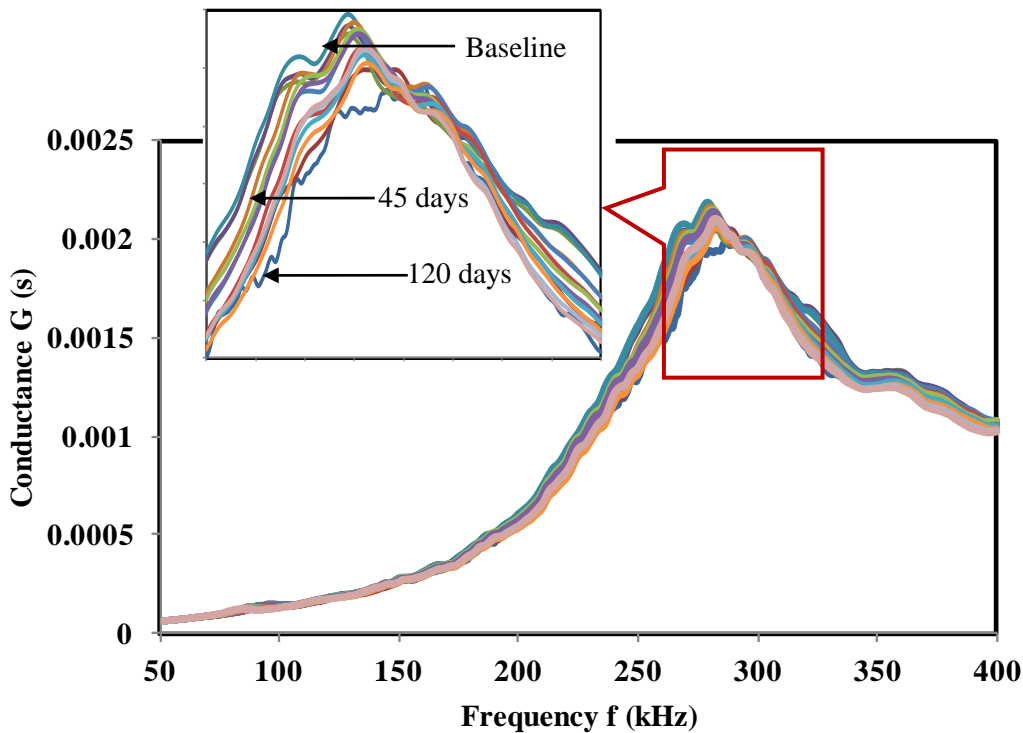


Figure 4.8 Variation of conductance signatures of specimen 2 during accelerated corrosion process

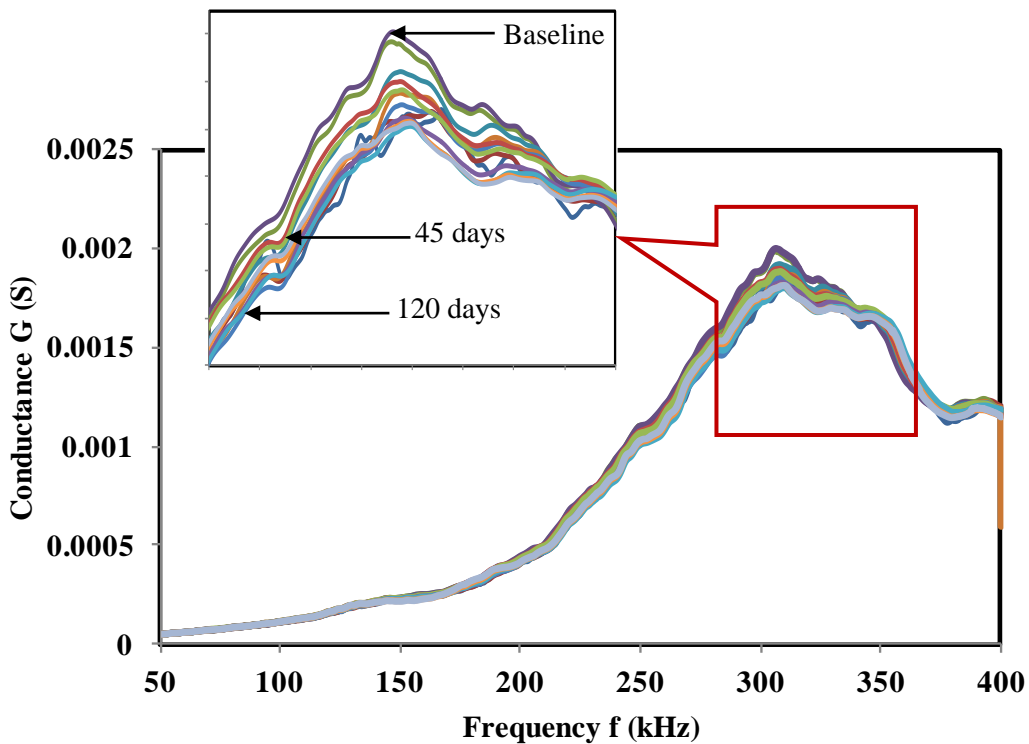


Figure 4.9 Variation of conductance signatures of specimen 3 during accelerated corrosion process

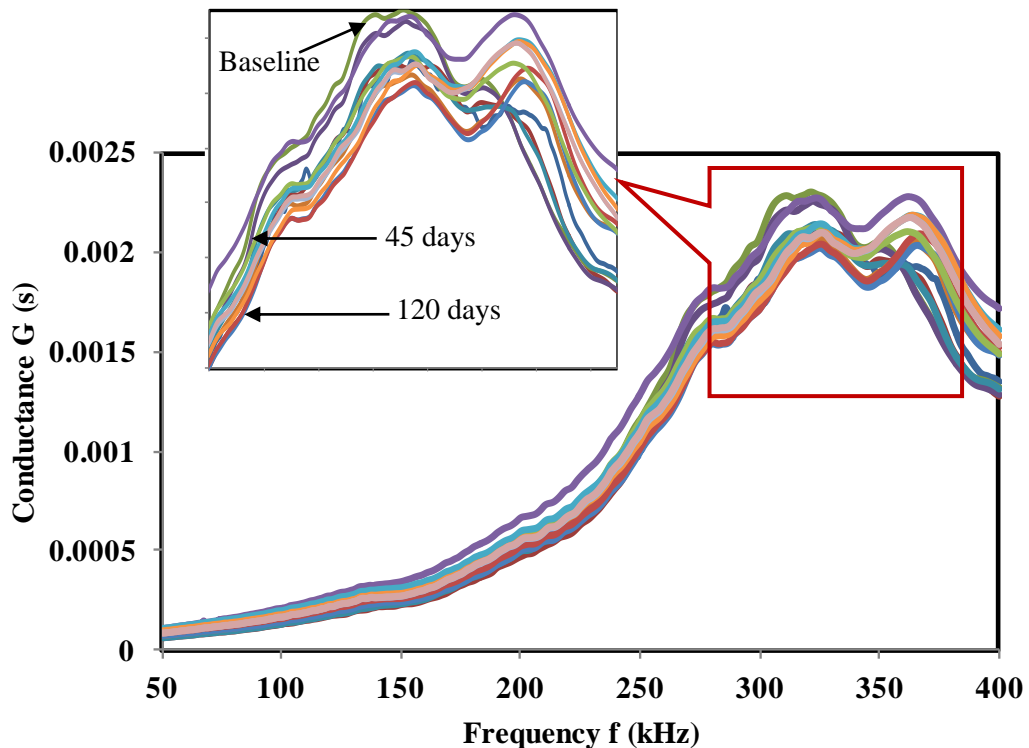


Figure 4.10 Variation of conductance signatures of specimen 4 during accelerated corrosion process

This is in contrast to the observations made by Soh and Bhalla (2005) in their experiments to monitor concrete curing, where the peak magnitude increased, as the additional stiffening action caused by the increase of concrete strength.

To quantify the changes in the conductance signature, statistical indices such as RMSD was calculated. Fig. 4.11 illustrates the variation of the RMSD index of the four RC specimens. For specimen 1, the RMSD values exhibit a linear trend with a large scatter. Specimens 2 and 4 exhibit a haphazard trend, while specimen 3 shows a parabolic trend. In general, the RMSD values exhibit a large variation from one specimen to another. The trend of RMSD values as observed here for embedded rebars and that of bare steel bars (Chapter 3) are very similar to that reported by Bhalla et al., (2012), where the RMSD based damage index could not provide a consistent variation for steel bolted specimens. The subsequent sections deals with the development of corrosion model using extracted equivalent parameters.

4.5 ANALYSIS BASED ON EQUIVALENT STRUCTURAL PARAMETERS

Again, the procedure outlined in Chapter 3 was adopted to determine the drive point mechanical impedance of the structure, $Z_{s,eff} = x + yj$, at a particular frequency ω , from the admittance signature. The 2D interaction model represented by Eq. 2.21 was used, since the PZT patch bonded on rebar and surrounded by concrete exhibits d_{31} and d_{32} couplings. At the same time, the PZT patch loading in direction ‘3’ is neglected by assuming the frequencies involved to be much less than the first resonant frequency for thickness vibrations. Following this procedure, ‘x’ and ‘y’ were determined for the entire frequency 50 to 400 kHz. A close examination of the extracted impedance components in the frequency range 150-250 kHz revealed that the system

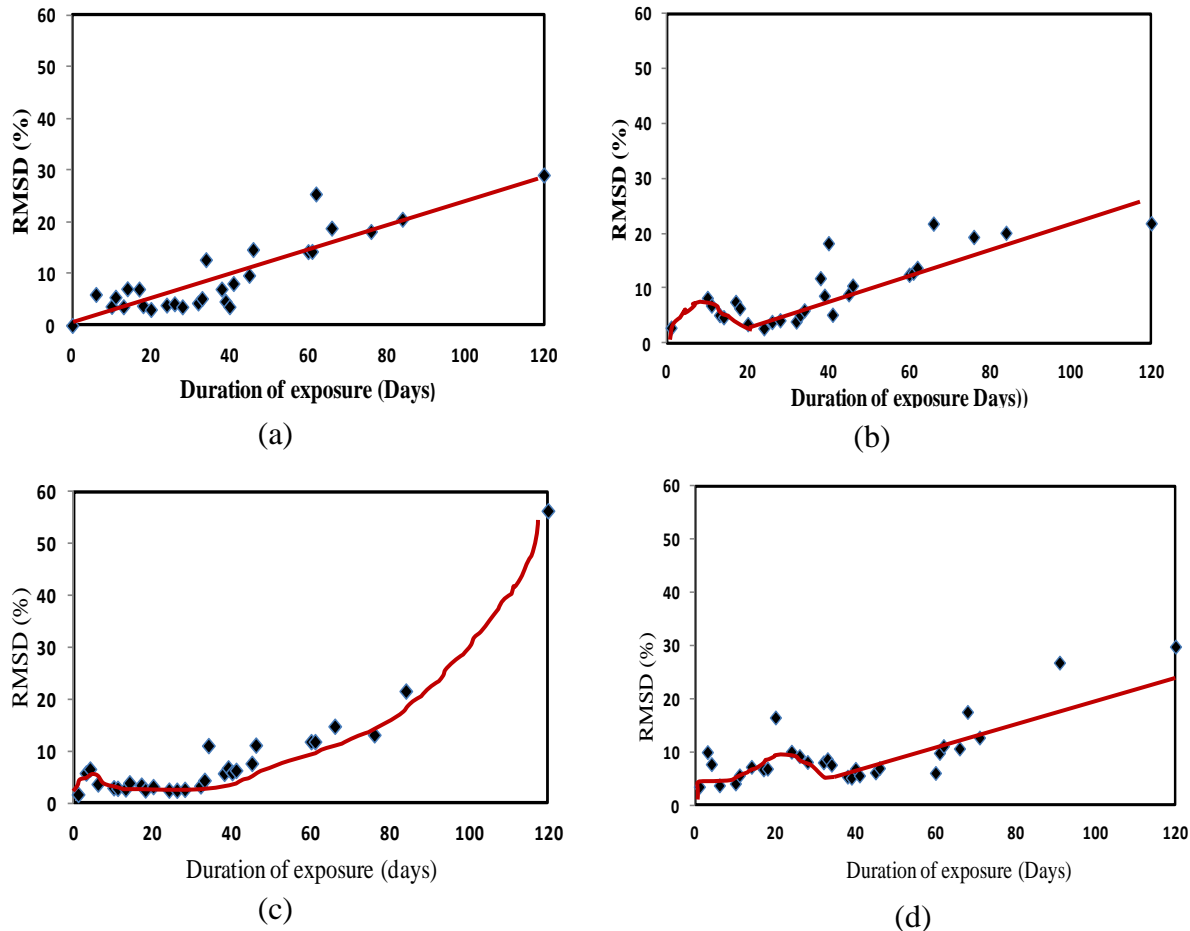


Figure 4.11 Variation of RMSD index during accelerated corrosion process
(a) Specimen 1 (b) Specimen 2 (c) Specimen 3 (d) Specimen 4

exhibited similar system behaviour as that of parallel spring-damper-mass (k - c - m) combination (Hixon, 1998) as shown in Fig. 4.12. This system is chosen to include mass and calculate the rate of corrosion.

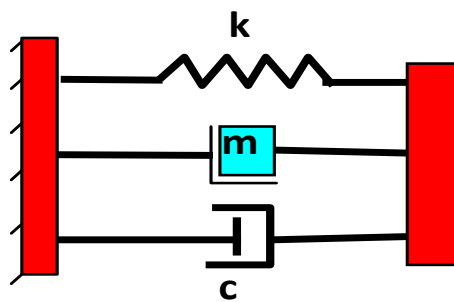


Figure 4.12 Identified system (Parallel combination of spring-mass-damper)

For this system,

$$x = c \quad \text{and} \quad y = m\omega - \frac{k}{\omega} \quad (4.5)$$

The angular frequency at which $y = 0$ is denoted by ω_0 . Using Eq. (4.5), the system parameters can be determined, by algebraic calculations, as

$$k = \frac{y\omega\omega_0^2}{(\omega^2 - \omega_0^2)} \quad (4.6)$$

$$m = \frac{k}{\omega_0^2} \quad (4.7)$$

and

$$c = x \quad (4.8)$$

Fig. 4.13 shows the comparison between the experimental plots with the analytical plots for the identified equivalent system (parallel combination of k-c-m). Reasonably good agreement can be observed between the two plots. Hence, the structural system identification is satisfactory. Using Eqs. 4.6 to 4.8 and the actual impedance plots, the average “equivalent” system parameters c , k and m in the healthy state (before subjecting the specimens to accelerated corrosion) were determined as listed in Table. 4.2.

Table 4.2 Equivalent structural parameters identified by PZT patch in healthy state

Specimen	c (Ns/m)	k (KN/m)	m (kg)
1	231.45	683.91	0.21
2	135.06	473.29	0.14
3	188.37	753.60	0.23
4	177.62	618.36	0.19

CHAPTER- 4 Development of Corrosion Assessment Model for Rebars Embedded in RC Structures

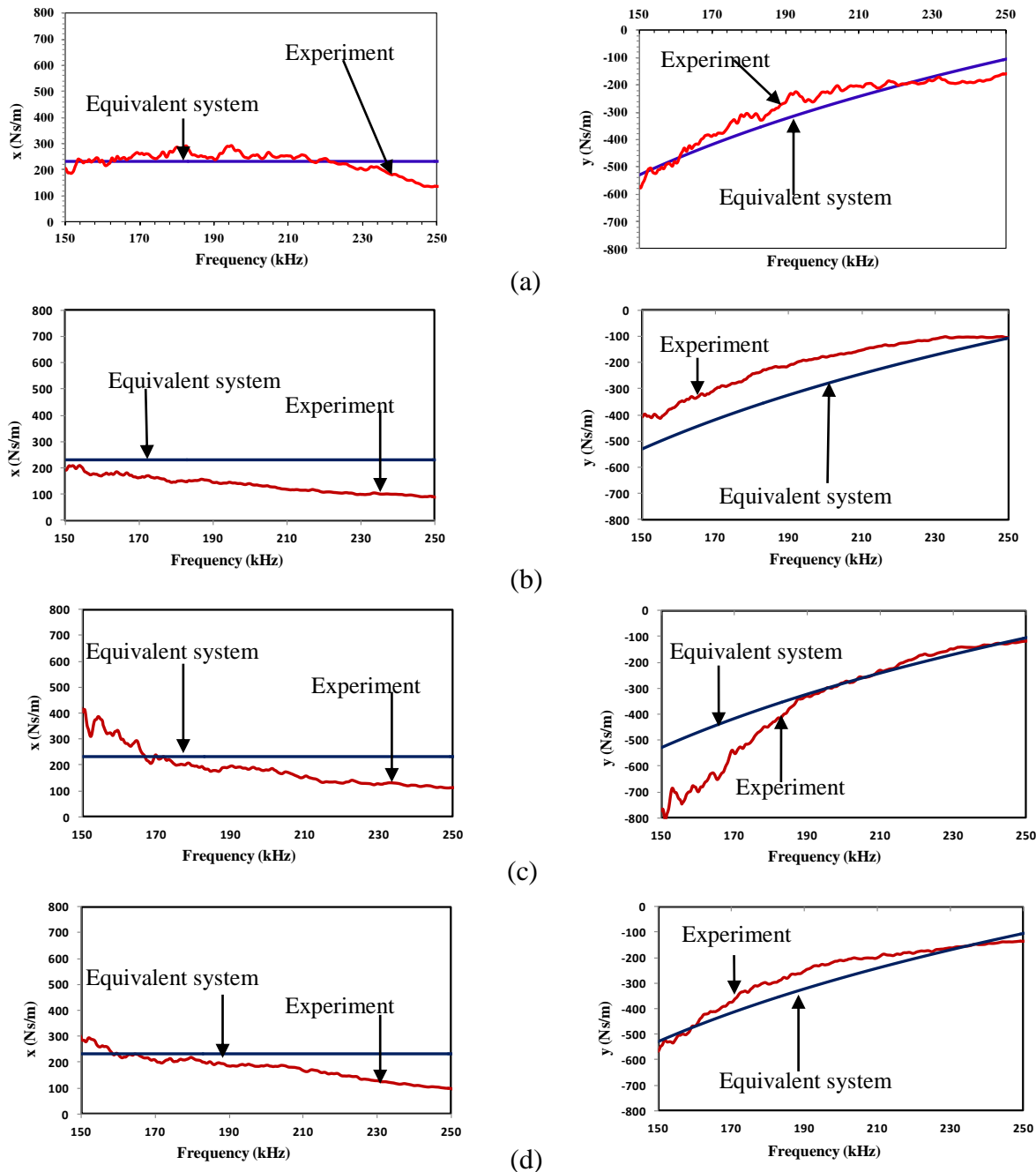


Figure 4.13 Experimental and analytical plots of ‘ x ’ and ‘ y ’ for baseline signatures
 (a) Specimen 1 (b) Specimen 2 (c) Specimen 3 (d) Specimen 4

The variation of the equivalent structural parameters m and k with corrosion progression are shown in Figs. 4.14 and 4.15 respectively. As expected (see Eqs. 4.6 and 4.7), both k and m follow similar trends.

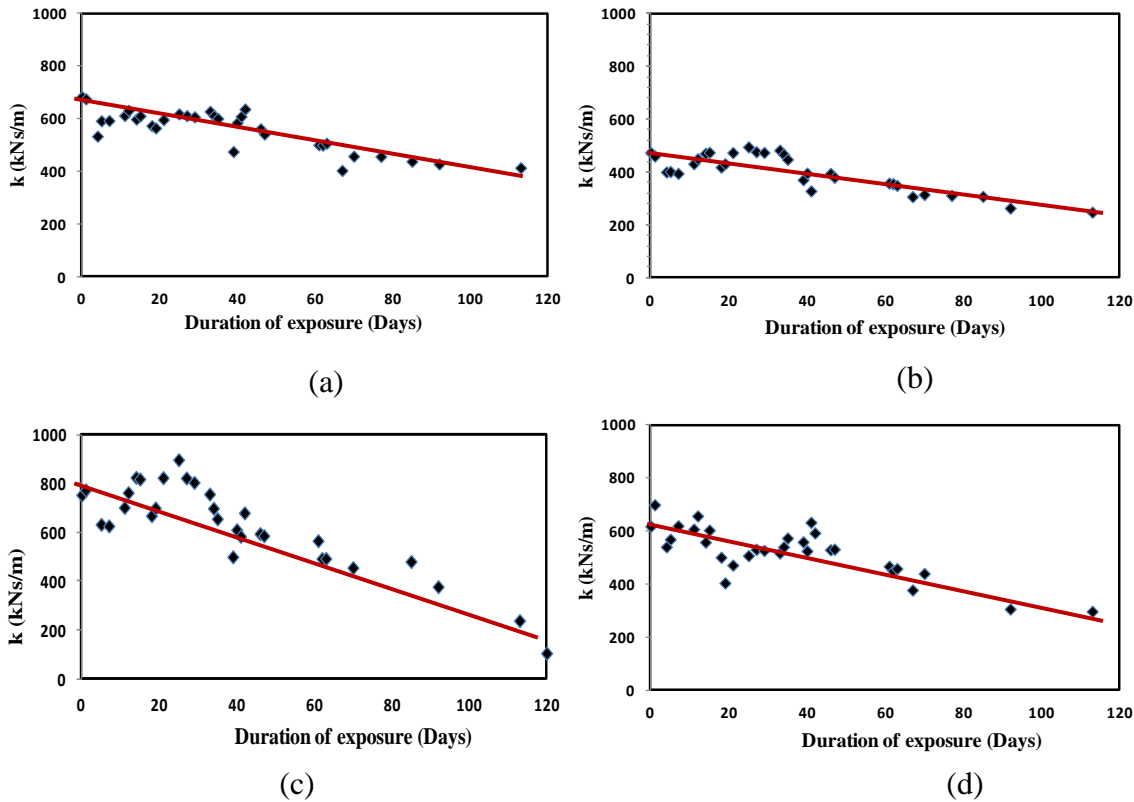


Figure 4.14 Variation of PZT identified stiffness with corrosion progress
(a) Specimen 1 (b) Specimen 2 (c) Specimen 3 (d) Specimen 4

The variation of m and k as observed exhibit more or less a linear trend with large scatter during the initial 45 days and after that the values found to decrease consistently. In contrast to the variation of RMSD (Fig. 4.11) the variations of m and k are more regular. With corrosion progression, the equivalent stiffness and the equivalent mass can be observed to reduce by about 35% and 18% respectively on an average after an exposure period of 120 days. The dimensionless parameters $\Delta k/k$ and $\Delta m/m$, where Δk is the stiffness loss and Δm is the mass loss respectively, were also computed and plotted against the duration as shown in Fig. 4.16 and 4.17 respectively. The calibration of these parameters on the basis of observed deterioration is covered in the next section.

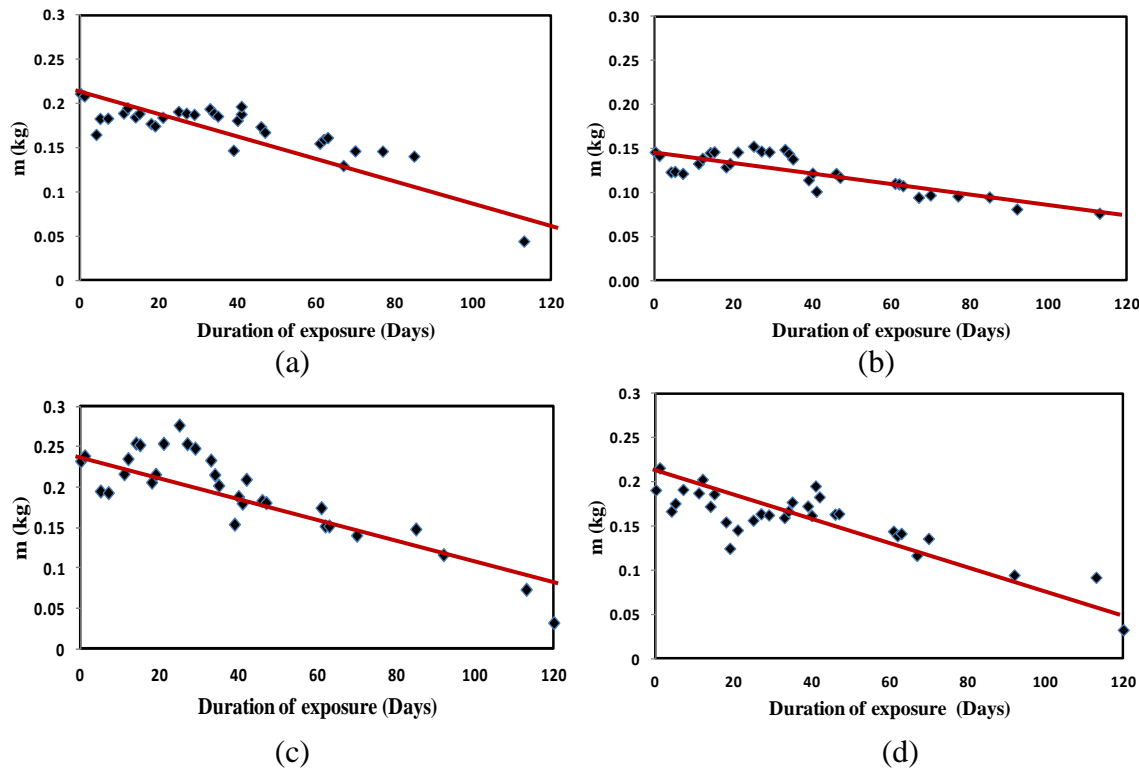


Figure 4.15 Variation of PZT identified mass with corrosion progression

(a) Specimen 1 (b) Specimen 2 (c) Specimen 3 (d) Specimen 4

4.6 CALIBRATION OF EXTRACTED EQUIVALENT PARAMETERS WITH CORROSION SEVERITY

This section deals with the calibration of the various phases of corrosion with the PZT identified stiffness parameter and also correlating the corrosion rates based on equivalent mass loss with the actual mass loss.

4.6.1 Development of Equivalent stiffness model

The actual stiffness (initial and final) of the rebar was calculated indirectly based on the minimum cross sectional area (along the length of the bar), before the rebar was embedded in concrete and after the rebar was removed from the concrete specimen by splitting after 120

days respectively. The PZT identified equivalent stiffness, both initial and final, was directly obtained from the Eq. (4.6) by substituting the impedance parameters of baseline (for initial) and of 120 days (for final). Table 4.3 lists the computed stiffness (both PZT identified and actual) for all the four specimens.

Knowing the stiffness, the relation between the actual stiffness loss and the PZT identified stiffness loss can be written as

$$\left(\frac{\Delta k}{k}\right)_{actual} = \Lambda_k \left(\frac{\Delta k}{k}\right)_{PZT} \quad (4.9)$$

where Λ_k is a constant relating the non dimensional PZT based stiffness loss with actual stiffness loss. Using Eq. (4.9) Λ_k is calculated for all the specimens and tabulated in Table 4.4. Three out of four specimens have closely matching value of Λ_k . The value of Λ_k averaged covering all the four specimens comes out to be 0.49. This correlation helps in estimating the actual stiffness loss due to the corrosion (whose measurement is not feasible in a real structure non-destructively) by determining the PZT identified stiffness loss instead (using Eq.4.6), which can be achieved non-destructively.

Table 4.3 Initial and final stiffness (actual and PZT identified)

Specimen	Initial stiffness (actual N/m)	Final stiffness (actual N/m)	Initial stiffness (PZT identified kN/m)	Final stiffness PZT identified kN/m)
1	119.75	95.35	683.91	437.92
2	119.75	89.14	473.29	247.61
3	119.75	87.81	753.60	105.53
4	119.75	86.04	618.36	297.01

Table 4.4 Relation between non-dimensional actual stiffness loss and PZT identified stiffness loss

Specimen	$\Delta k/k$ (actual)	$\Delta k/k$ (PZT identified)	$\Lambda_k = \frac{(\frac{\Delta k}{k})_{actual}}{(\frac{\Delta k}{k})_{PZT}}$
1	0.20	0.35	0.56
2	0.25	0.47	0.53
3	0.26	0.85	0.31
4	0.28	0.51	0.54

By visual inspection of the specimen 5 shown in Figs. 4.6 (a, b and c), it can be observed that by the 45th day, the accumulation of corrosion products had just started and by 120 days, it had reached an alarming level where the specimen had cracked due to the larger volume of the corrosion products at the steel/concrete interface.

Hence, the chloride induced corrosion process can be distinguished into three different phases, namely, corrosion initiation followed by propagation and finally, the cracking, based on the visual inspection and the variation of the dimensionless stiffness parameter, as illustrated in Fig. 4.16. Phase I, the corrosion initiation phase up to 45th day, during which the dimensionless stiffness parameter $\frac{\Delta k}{k}$ (based on PZT identified stiffness) ranges between 0 to 0.2. This is followed by phase II, the corrosion propagation phase from 45th day to 90th day during which the $\frac{\Delta k}{k}$ values ranges from 0.2 to 0.4, i.e. after initiation of the corrosion process, the accumulation of corrosion products (iron oxides and hydroxides), occupying a volume several times larger than that of the original iron (Tutti, 1982). This leads to internal stresses that result in cracking and spalling of the concrete cover.

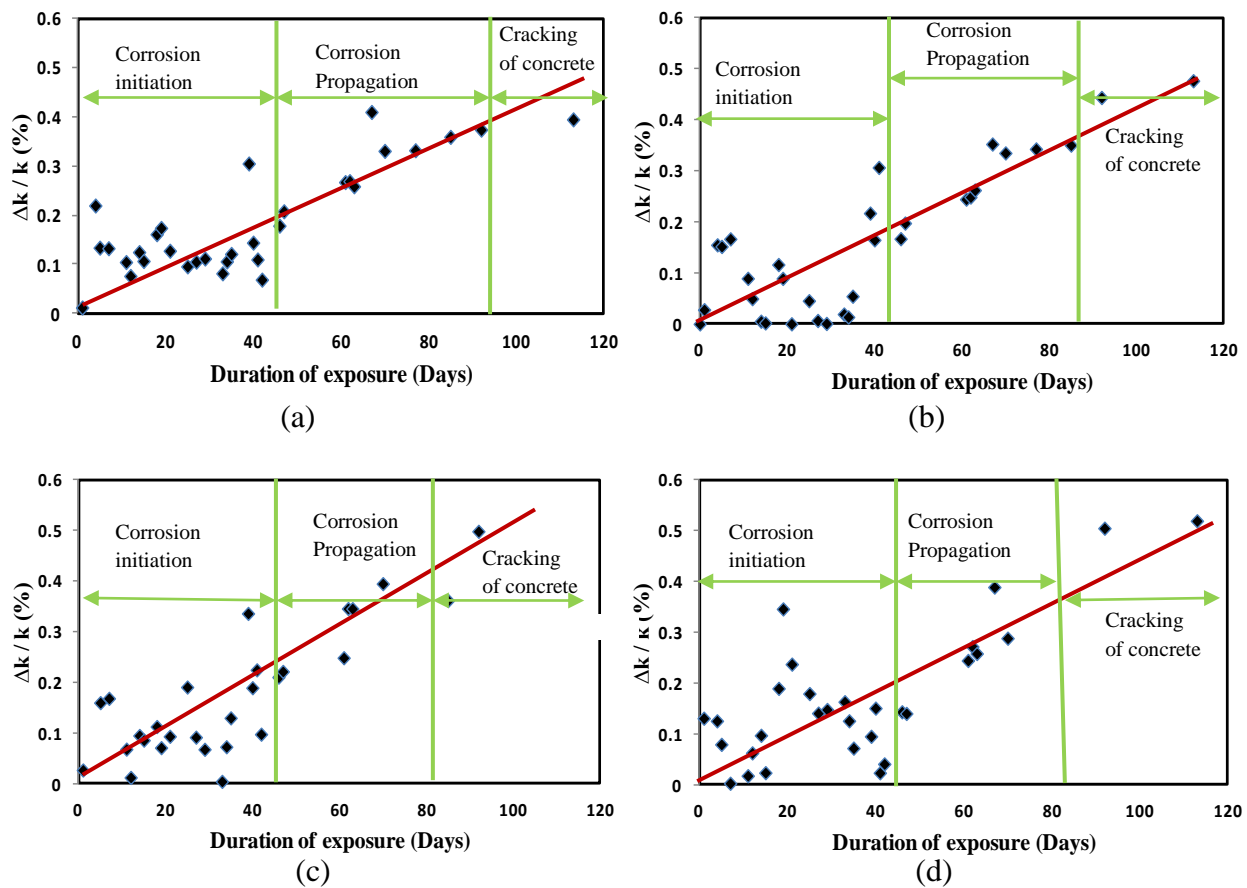


Figure 4.16 Variation of ($\Delta k / k$) PZT identified stiffness loss with corrosion progression
(a) Specimen 1 (b) Specimen 2 (c) Specimen 3 (d) Specimen 4

At this stage the intrusion of aggressive agents, oxygen and humidity is facilitated. Finally, phase III starts, accompanied by large scale concrete cracking due to the overshooting of the internal stresses caused from the building up of corrosion products, during which the $\frac{\Delta k}{k}$ values are typically in excess of 0.4. This can be considered as an alarming situation, where the total loss of the structural integrity occurs. Hence, in an actual scenario, the PZT identified stiffness ‘ k ’ parameter alone can thus provide satisfactory information about level of corrosion induced damage non-destructively in term of identifying the relevant phase of corrosion and can be substitute to the conventional electro-chemical techniques. The

application of this approach is illustrated in chapter 7 for the case of RC specimens subjected to naturally occurring corrosion.

4.6.2 Development of Equivalent Mass Model for Corrosion Rates

Gravimetric mass loss technique is a destructive method, which deals with the measurement of mass of the rebar before being embedded into the concrete and after the end of the corrosion experiments, taking it out destructively. The detailed test procedures of preparing, cleaning, and evaluating corrosion test specimens are described in ASTM G1 (ASTM, 2012). The difference in mass (gravimetric loss) is a quantitative average of the attack of corrosion. Although this method is very time-consuming and only applicable to the laboratory studies, it is a useful tool to check the corrosion rates obtained from other techniques.

To determine the corrosion rates, the initial mass of all the rebars were measured before embedding them. After splitting all the specimens, the final mass loss of the steel bars was determined by the gravimetric method after chemically cleaning the corrosion products. The PZT identified mass was also calculated directly using Eq. (4.7) during the corrosion exposure, without any destructive measure.

Knowing the actual and the PZT identified mass a similar relation as Eq. (4.9) can be derived relating both as,

$$\left(\frac{\Delta m}{m}\right)_{actual} = \Lambda_m \left(\frac{\Delta m}{m}\right)_{PZT} \quad (4.10)$$

Where Λ_m is a constant relating the non-dimensional PZT based mass loss with actual mass loss.

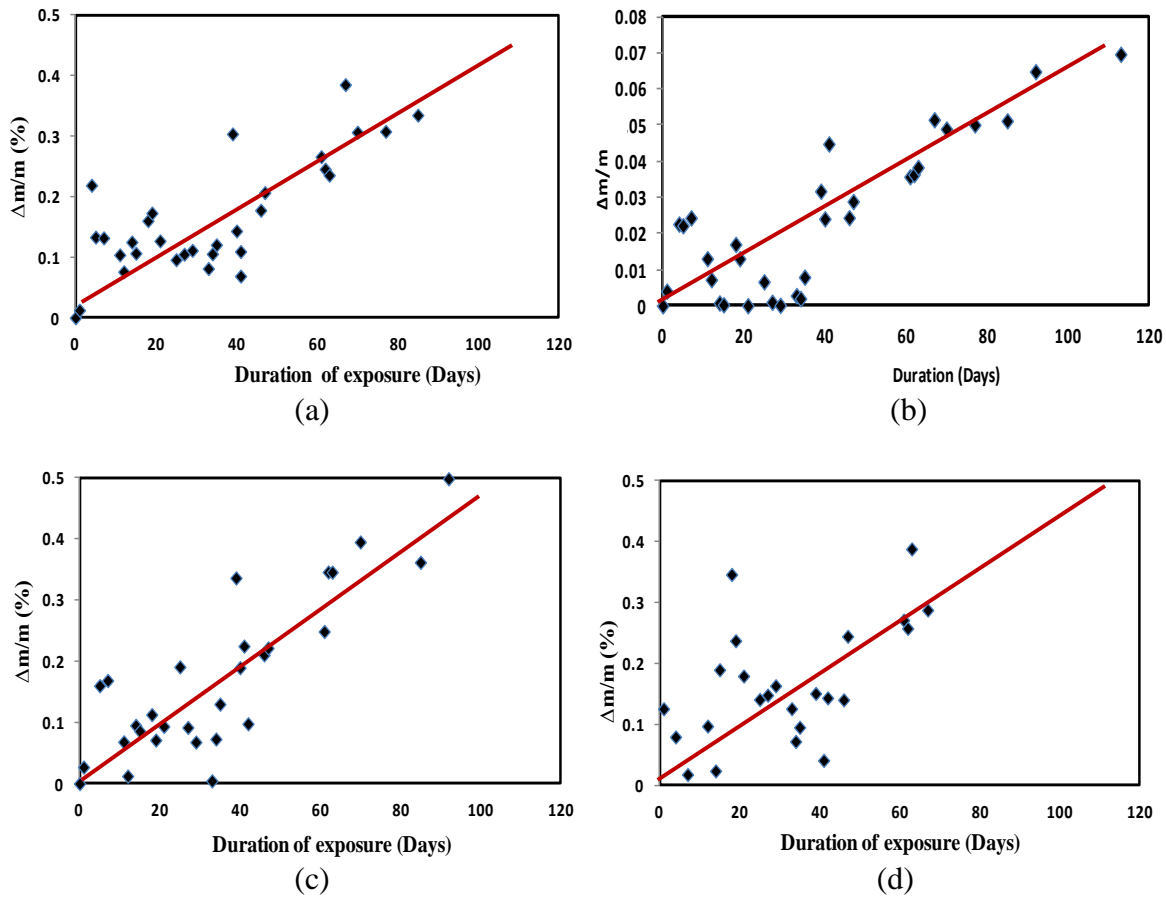


Figure 4.17 Variation of ($\Delta m/m$) PZT identified mass loss with corrosion progression
(a) Specimen 1 (b) Specimen 2 (c) Specimen 3 (d) Specimen 4

Table 4.5 compares the non dimensional actual mass loss and non dimensional PZT identified mass loss. A_m was computed for all the specimens and the average value of A_m works out to be 0.54. This correlation will be useful in calculating the corrosion rates of the rebar, because measuring the actual mass loss in real life structures is not possible as rebar is inside the concrete. Based on the EMI measurements, this can be achieved non-destructively.

Knowing the mass loss, the corrosion rate (mm/year) can be calculated as

$$\Delta_c = \frac{(K * \Delta m)}{(a * T * D)} \quad (4.11)$$

CHAPTER- 4 Development of Corrosion Assessment Model
for Rebars Embedded in RC Structures

where K is a constant equal to 8.76×10^4 , Δm is the mass loss in grams, a is the area in cm^2 , T is the time of corrosion exposure in hours and D is the density of steel i.e., 7.8 g/cm^3 . The corrosion rates were calculated using both PZT identified mass loss and actual mass loss and tabulated in Table 4.6.

Table 4.5 Relation between non-dimensional actual mass loss and PZT identified mass loss

Specimen	Initial mass (actual kg)	Final mass (actual kg)	Initial mass (PZT identified kg)	Final mass (PZT identified kg)	$\Delta m/m$ actual	$\Delta m/m$ PZT	$\Lambda_m = \frac{\left(\frac{\Delta m}{m}\right)_{actual}}{\left(\frac{\Delta m}{m}\right)_{PZT}}$
1	0.27	0.21	0.21	0.14	0.20	0.33	0.60
2	0.27	0.21	0.14	0.07	0.22	0.47	0.46
3	0.27	0.19	0.23	0.11	0.26	0.49	0.53
4	0.27	0.19	0.19	0.09	0.28	0.51	0.54

Table 4.6 Corrosion rate values (without considering Λ_m)

Specimen	Identity	Initial mass (kg)	Final mass (kg)	Mass loss (kg)	$\Delta_c = (87.6 * \Delta m / a * D * t)$
1	Actual	0.27	0.21	0.05	1.06
	PZT	0.21	0.14	0.07	1.37
2	Actual	0.27	0.20	0.06	1.33
	PZT	0.14	0.07	0.06	1.29
3	actual	0.27	0.19	0.07	1.39
	PZT	0.23	0.11	0.11	2.24
4	actual	0.27	0.19	0.07	1.47
	PZT	0.19	0.091	0.09	1.91

Table 4.7 presents a comparison of the corrosion rate determined using the PZT identified mass ($\Lambda_m = 0.54$ was considered) and the one determined based on the actual gravimetric mass loss. Two out of the four specimens, the corrosion rate has been predicted with only 20 % error. In the remaining specimens, the error has been over 40%. However, keeping in view of the complicated natures of corrosion and associated variability this provides some picture. The variability in HCP is much higher. It is concluded that the PZT identified mass loss can conveniently substitute the actual mass loss determination, thus circumventing the use of actual mass loss, which is in fact practically not feasible for corrosion rate determination.

Table 4.7 Comparison of actual and PZT identified corrosion current rates (considering Λ_m)

Specimen	Corrosion rates using actual mass loss (mm/year)	Corrosion rates using PZT identified mass loss after incorporating Λ_m (mm/year)	Error (%)
1	1.066	0.859	19.4
2	1.338	0.457	65.8
3	1.396	1.212	13.18
4	1.474	0.848	42.46

4.7 CONCLUDING REMARKS

The chapter has presented a new diagnostic approach to carry out the assessment of rebar corrosion based on the equivalent system parameters identified by means of the EMI technique. The real and imaginary components of the admittance signature were used to extract the damage sensitive equivalent structural parameters. The extracted equivalent structural parameters (m and k) correlate well with the actual mass and stiffness. Empirical

CHAPTER- 4 Development of Corrosion Assessment Model for Rebars Embedded in RC Structures

models derived between the actual parameters and the PZT identified parameters can be used in real life corrosion monitoring of RC structures, where the determination of actual parameters of rebar is impractical. Based on the mass model, corrosion rates determined using the PZT identified mass loss correlate well with those calculated based on the actual mass. Based on the stiffness model, it is recommended from the results and observations that a value of $\Delta k/k$ over 0.2 indicates corrosion initiation and 0.4 indicates alarming corrosion level. The next chapter explores the possibility of using ready to use piezo-based CVS for corrosion assessment instead of PZT patches surface bonded on to the rebars.

CHAPTER- 5
COMPARISON OF REBAR CORROSION ASSESSMENT CAPABILITY OF SURFACE BONDED AND EMBEDDED PIEZO SENSORS

5.1 INTRODUCTION

As described in the previous chapters, the PZT patches need to be bonded to the surface of rebar prior to casting in order to monitor corrosion induced damage. This needs surface preparation and other minute bonding tasks so as to warrant certain skill level for the user. Recently, ready to use packaged sensors have been proposed (Bhalla and Gupta, 2007), which can simply be embedded into concrete and do not require high skill from the user. The packaging also protects the sensor from the harsh environment. This chapter presents a corrosion monitoring study of RC specimens using the embedded sensor, for this purpose, CVS, a proprietary product of IIT-Delhi (Bhalla and Gupta, 2007), as shown in Fig. 5.1 have been directly used.

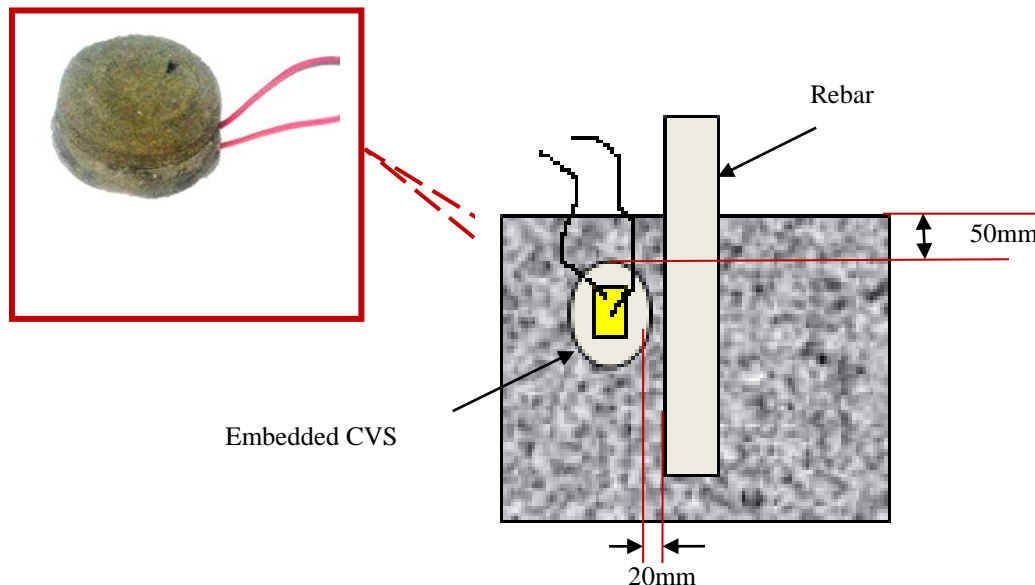


Figure 5.1 RC cube specimen with embedded sensor

CHAPTER- 5 Comparison of Rebar Corrosion Assessment Capability of Surface Bonded and Embedded Piezo Sensors

The main objective of this chapter is to assess corrosion using embedding CVS in RC structures and compare the results with the surface bonded piezo sensors (SBPS), already discussed in Chapter 4.

5.2 ADVANTAGES OF EMBEDDED SENSORS

In general, the PZT patches can be either surface bonded to monitor the existing structures or embedded into the structures during their casting. The important features of embedding the PZT patch into the host structure are durability, protection from the surface finish and safety against vandalism etc. In addition, these patches do not interfere with the aesthetic beauty of the structure. When used in an onsite situation, embedding the sensor is standardized than that of the SBPS.

The application of adhesive for bonding the SBPS to the host structure, while accurate in a laboratory situation, may not be satisfactory at site, as a higher variability is likely to be associated. Since the performance (sensing/actuating) of a piezo transducer highly depends on the ability of the bond layer to transfer the stress and strain (through shear lag mechanism) between the transducer and the structure (Bhalla and Moharana, 2013), embedded sensors show better and more consistent performance.

5.3 CONFIGURATION AND APPLICATION OF EMBEDDED PZT SENSORS

Several configurations of embedding PZT patches are described in the literature. However, the embeddable PZTs assembled by various methods are not general purpose and are mostly application based. Annamdas et al. (2010) has presented details of various configuration of embedding the PZT patch with its merits and demerits. For example, an embeddable patch

CHAPTER- 5 Comparison of Rebar Corrosion Assessment Capability of Surface Bonded and Embedded Piezo Sensors

prepared for axial load monitoring cannot be used for transverse load monitoring and vice versa (Annamdas and Soh. 2006; Annamdas et al., 2010). However, the CVS developed at IIT Delhi is completely encapsulated (unlike the design of Chen et al., 2004) to ensure much superior protection. It has superior signal to noise ratio, better strain compatibility with surrounding concrete and has higher longevity as compared to SBPS.

The several applications of embedded sensors for SHM of concrete and other composites are summarized as follows:

Wu and Chang (2006 a, b) have studied the damage detection method of debonding damage in RC structures using embedded PZT sensors built into the structure. The method is also verified by experimental test results, which showed that the signal's amplitude of the sensor decreased with the extent of increase in debonding.

Qin et al. (2010) studied the feasibility of using embedded sensor to detect the acoustic emission activities in concrete. They reported excellent sensing abilities of the sensor for acoustic emission detection through a four point bending test on concrete beam. Higher sensitivity was also observed for the embedded sensors.

Kang et al. (2010) conducted an experimental study to assess damage in composite plates by fusing information from multiple sensing paths of the embedded PZT sensor. Their tests showed satisfactory detection of defects in composite plates using the embedded sensor.

Kim et al. (2011) proposed a real time concrete strength monitoring technique using embedded sensors. They found that the resonant frequencies in the impedance signals shifted gradually to the right due to the strength development of the concrete.

CHAPTER- 5 Comparison of Rebar Corrosion Assessment Capability of Surface Bonded and Embedded Piezo Sensors

Quinn et al. (2012) developed a wireless sensing system to monitor initial curing and subsequent structural health of concrete. Their initial tests results showed that the embedded sensor to be sensitive to the removal of form work and can possibly detect debonding effects on aggregates. However, a detailed package design and the choice of packing material are required to ensure that package-cement interface does not initiate failure in concrete.

Hari et al. (2012) examined the effects of embedded piezoelectric fiber composite sensor (PFCSs), macro-fiber composite (MFC) and piezoelectric fiber composite (PFC) on the structural integrity of glass-fiber-epoxy composite laminates. From the tensile tests, it was observed that embedding the PFCS and the PZT sensors in a composite structure led to reduction in the ultimate strength by 3 % and 6% respectively. From the fatigue tests, it was concluded that both embedded PFCS and surface bonded PZT sensors exhibited change resulting from the fatigue behaviour of composite specimens. Overall, the pure PZT sensor seemed to have lower compatibility with composites when compared to PFCSs.

In this chapter, the corrosion sensing abilities of embedded CVS is compared with that of SBPS based on the experimental observations and results.

5.4 EXPERIMENTAL DETAILS AND RESULTS

Three RC cubes were cast following the same procedure outlined in Chapter 4. The only basic difference was that the PZT patch was not surface bonded to rebar but it was embedded inside the concrete as CVS while casting as shown in Fig. 5.1. All the other details such as dimensions of the rebar, the PZT patch and the cube were same as in the specimens described

in Chapter 4. It should be noted that unlike SBPS, the CVS is not directly in contact with the corroding rebar but situated at a horizontal distance of 20 mm from the rebar (see Fig. 5.1).

5.4.1 Comparison of Conductance Signature

The baseline conductance signature from the embedded CVS was acquired after the 28 day curing period and is compared with that of the CVS embedded inside concrete in Fig. 5.2. As seen from the figure, it may be noted that the magnitude and the frequency of the resonance peak of the SBPS is higher than that of the embedded CVS, which suggests that the SBPS encounters a stiffness higher than that of embedded CVS. In addition, the embedded CVS exhibits less sharp peaks when compared to the SBPS, which is because of the greater damping encountered by the CVS inside the mortar. These observations are consistent with the fact that SBPS is directly attached to the steel (which is stiffer and has much smaller damping than concrete), thereby getting a greater influence from steel rebar.

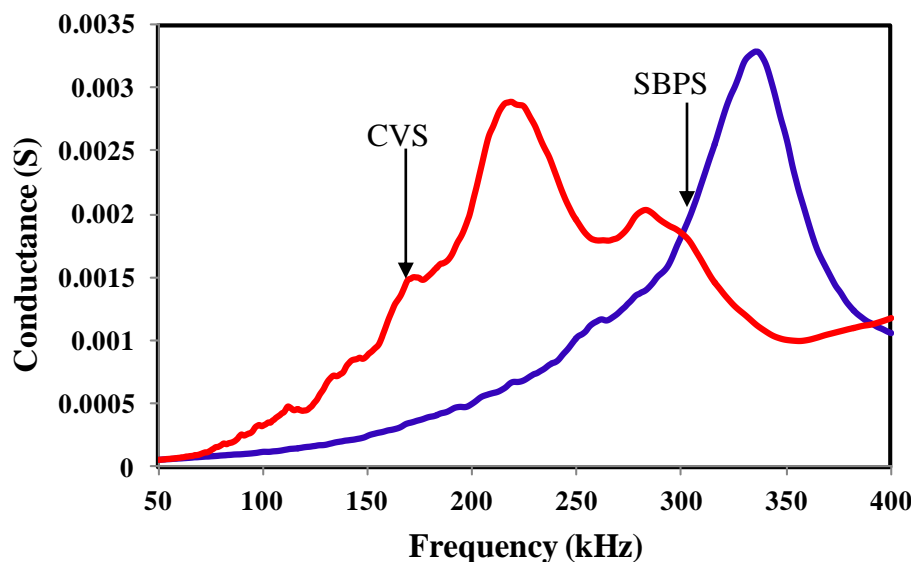


Figure 5.2 Comparison of conductance signature of SBPS and CVS in pristine state

After acquiring the baseline signature, the cubes were subjected to accelerated chloride induced corrosion following the same procedure outlined in Chapter 4 for 120 days with the aim of determining the feasibility of using the CVS as corrosion monitoring sensor.

Fig. 5.3 shows the variation of conductance signatures of the embedded CVS for a typical specimen 1 during the accelerated corrosion exposure. It can be observed that the CVS conductance signatures have shown considerable changes (Resonant peak frequency has been lowered consistently and the signature showed less sharp peaks during the entire exposure period) during the accelerated corrosion exposure. Fig. 5.4 compares the representative conductance signatures of SBPS and CVS during accelerated corrosion exposure. It can be observed that the resonance peak values have reduced for both SBPS and CVS. However, it can be observed that the reduction in magnitude of the resonance peak of corroded state is higher for the SBPS when compared to the CVS. This needs to be studied in depth so as to determine the utility and the sensing capabilities of embedded one, covered in the subsequent sections.

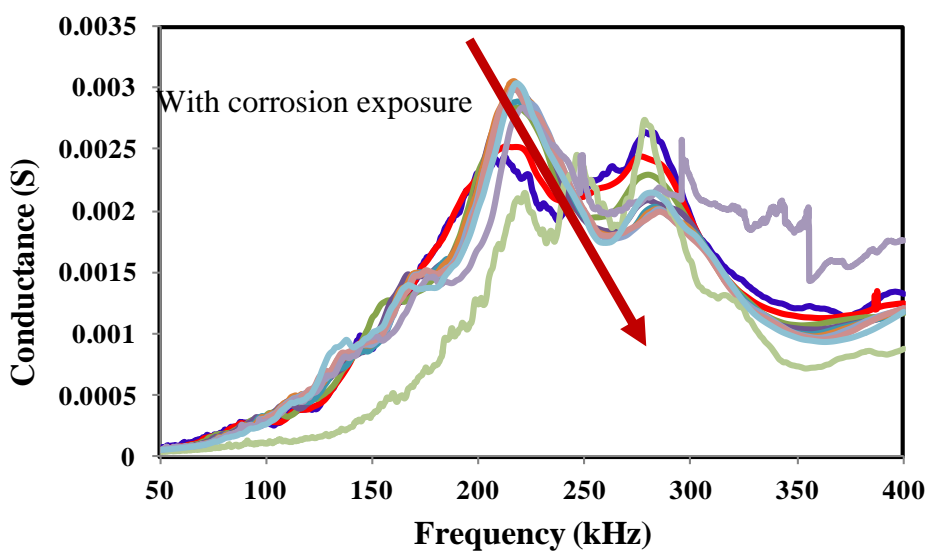


Figure 5.3 Variation of conductance signature of CVS of typical specimen during accelerated corrosion exposure

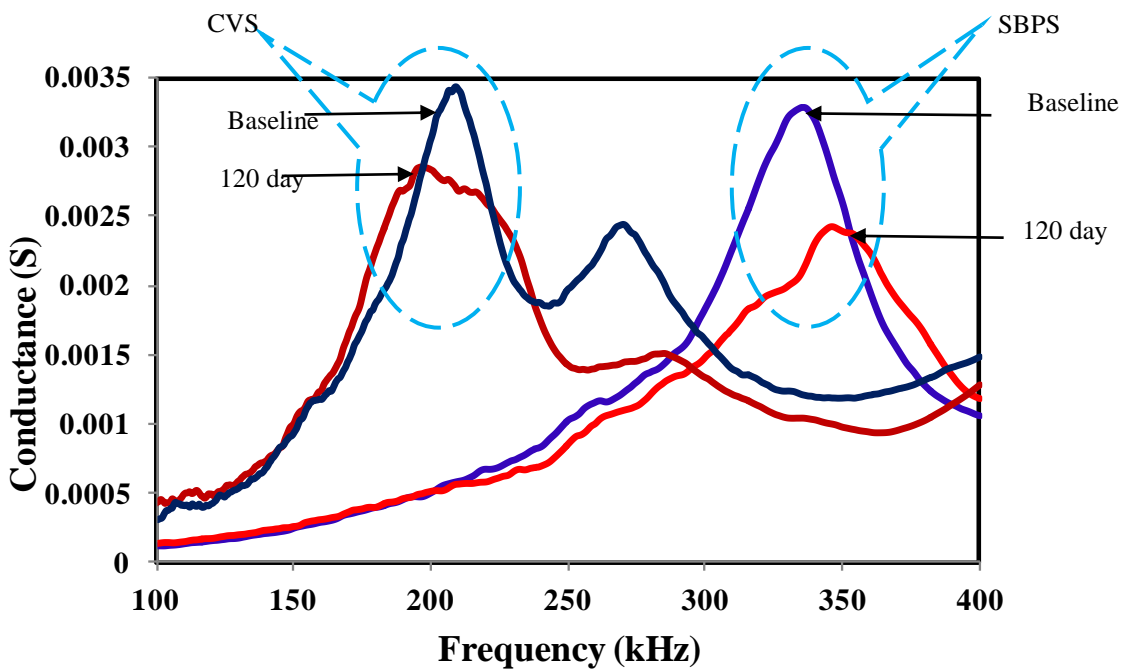


Figure 5.4 Comparison of variation in conductance signature due to corrosion exposure of CVS and SBPS of typical specimens

5.4.2 Comparison of Root Mean Square Deviation Index

The RMSD (see Eq. 3.9 of Chapter 3) index was determined and its variation with the accelerated corrosion exposure is presented in Fig. 5.5 for a typical CVS and SBPS. It can be observed from the figure that as the accelerated corrosion progresses, the RMSD values also increase, however reaching an asymptotic value of about 20 %. On comparing the RMSD graphs of both the SBPS and the CVS during the corrosion process, it can be observed that during the initial days of exposure, the RMSD values of the embedded CVS were higher than those of the SBPS, which indicates that the changes occurring during the ingress of chloride ions into concrete i.e. the corrosion initiation period has been captured better by the embedded CVS.

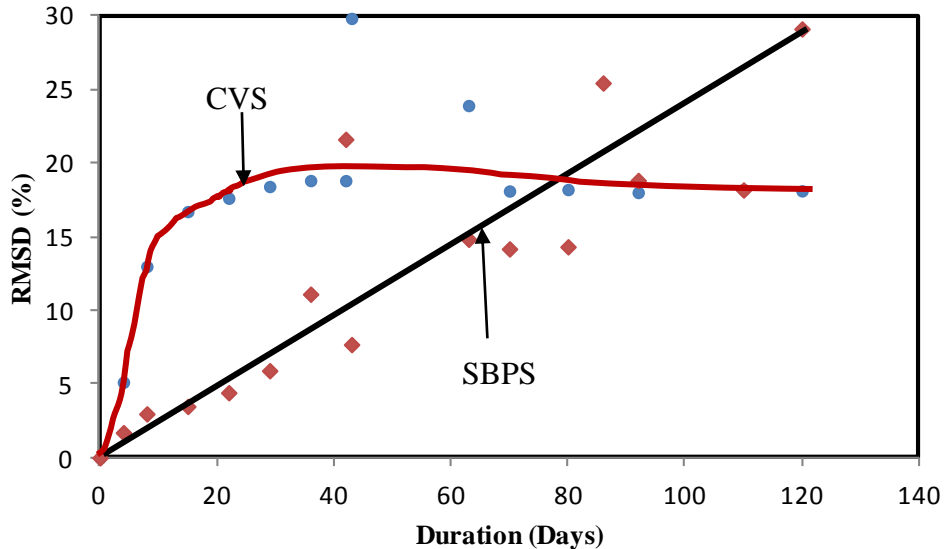


Figure 5.5 Comparison of variation in RMSD of CVS and SBPS of typical specimens

5.4.3 Comparison of Equivalent Stiffness Parameters

In order to evaluate the behaviour of the identified equivalent stiffness parameter of CVS, during the accelerated corrosion exposure, the equivalent structural parameters were determined in the 150-200 kHz frequency range from the admittance signature. In this frequency range, the system behaviour was similar to the one identified in Chapter 4 (for SBPS one). Fig. 5.6 shows the comparison between the experimental plots and the equivalent analytical plots, based on which the system is identified.

Fig. 5.7 (a, b) shows the effect of accelerated corrosion on the equivalent stiffness parameter of CVS and SBPS with corrosion progression. The stiffness can be observed to reduce until 40th day. Thereafter, with further exposure, the values remained more or less constant. It should be noted that the initial changes (up to 40th day) were captured reasonably well by CVS.

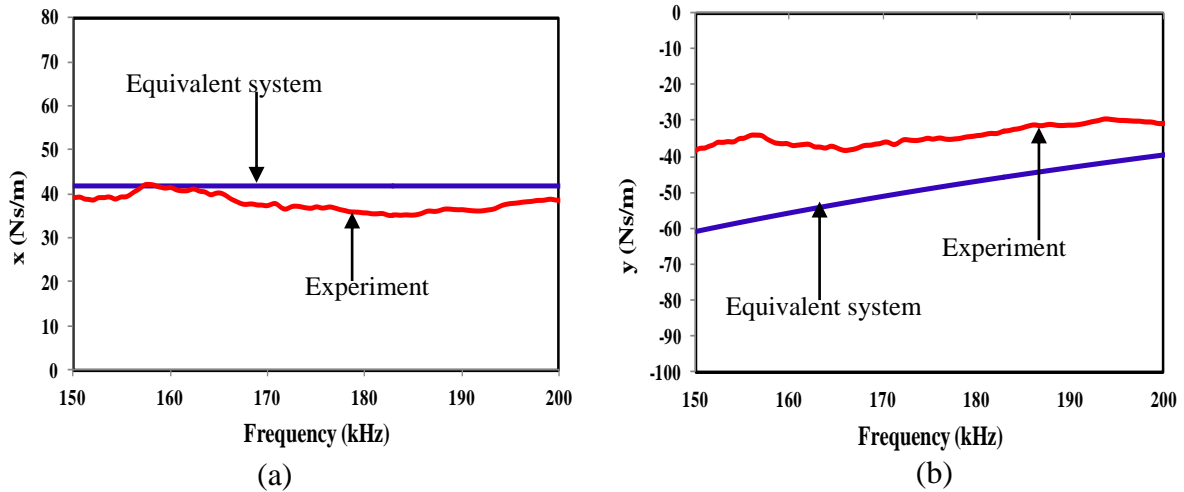


Figure 5.6 Experimental and analytical plots of embedded CVS
 (a) Variation of 'x' (b) Variation of 'y'

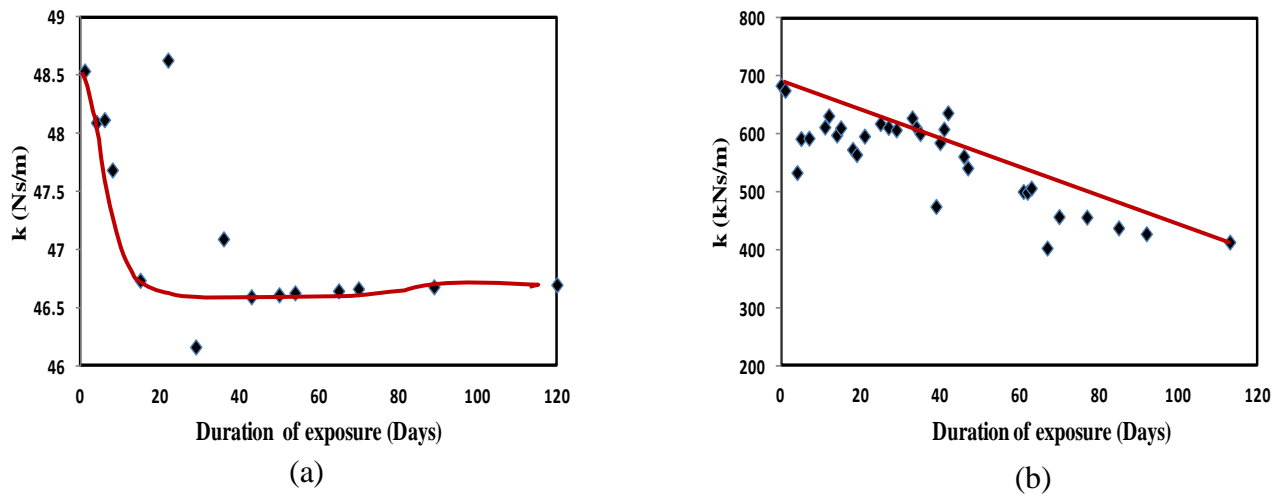


Figure 5.7 Variation of identified stiffness with corrosion progress
 (a) CVS (b) SBPS

On comparing the equivalent stiffness of the SBPS and CVS in Fig. 5.8, it can be observed that the magnitude of the equivalent stiffness identified by the embedded CVS is comparatively lower than that of the SBPS, since it is directly bonded to the surface of the rebar whereas CVS is embedded near rebar.

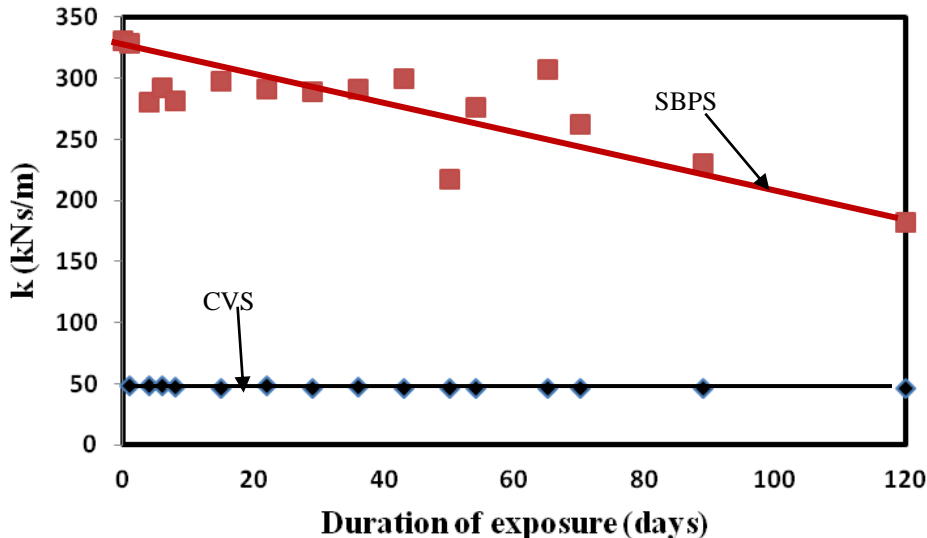


Figure 5.8 Comparison of variation of equivalent stiffness of CVS and SBPS

Fig 5.9 shows the variation of the non-dimensional stiffness loss for the CVS. To compare the relative stiffness loss of both SBPS and CVS, the non-dimensional stiffness loss is plotted for both for all the three specimens in Fig.5.10. It could be noticed that during initial priod of exposure the non-dimensional stiffness loss increased for both the SBPS and the CVS.

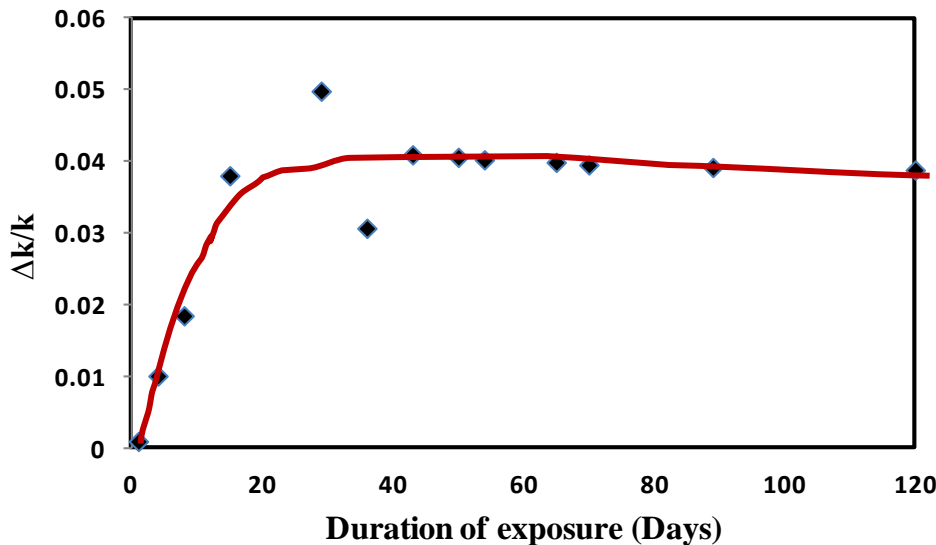


Figure 5.9 Variation of $\Delta k/k$ with corrosion progress of CVS

CHAPTER- 5 Comparison of Rebar Corrosion Assessment Capability of Surface Bonded and Embedded Piezo Sensors

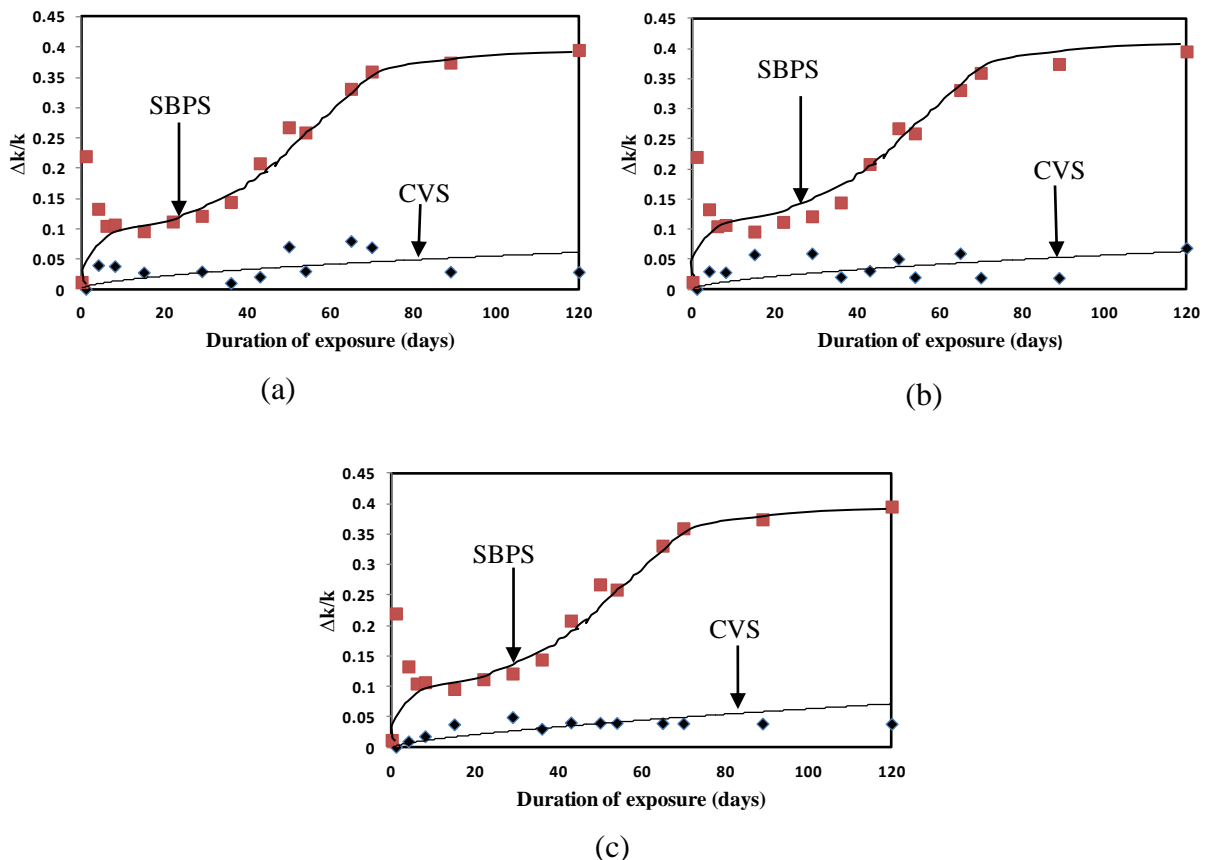


Figure 5.10 Comparison of variation in $\Delta k/k$ of CVS and SBPS
 (a) Specimen 1 (b) Specimen 2 (c) Specimen 3

After the 40th day (corrosion propagation phase just starts here), the stiffness loss of the CVS remained constant and that of the SBPS one increased monotonically. This shows that the CVS is able to capture the changes inside the concrete during the ingress of the chloride ions, passive layer break down and attack of the reinforcement. However after 40th day, the values of CVS remained more or less constant, which implies that the embedded CVS could not able to track the further changes occurring in the concrete rebar interface once the corrosion had initiated. In contrast, the values of the SBPS were found to increase during the corrosion exposure.

CHAPTER- 5 Comparison of Rebar Corrosion Assessment Capability of Surface Bonded and Embedded Piezo Sensors

As pointed out in the previous chapter, the chloride induced corrosion process, can be distinguished into three different phases, namely, corrosion initiation, corrosion propagation and finally, concrete cracking, which were defined based on the visual inspection and the dimensionless stiffness parameter by SBPS. Fig 5.11 (a and b) compares the corrosion phases distinguished by CVS and SBPS respectively along similar lines.

Based on the Figs. 5.11 (a) and (b), it can be observed that the CVS is highly sensitive during the corrosion initiation stage, corresponding to the period of time in which the chloride ions diffuse into the concrete and build up at the rebar surface towards a critical state when the passive layer's breakdown occurs. The SBPS, on the other hand, comparatively is less sensitive during this phase. However, the SBPS can be observed to be more sensitive during the second and third phases of corrosion i.e., corrosion propagation and cracking respectively. The initial stage ends when the passivity breaks down, at which corrosion propagation begins and significant corrosion starts. This stage can be identified by SBPS reasonably well. The higher sensitivity of CVS during initial stages is attributed to the fact that the sensor is embedded inside the concrete, and is very sensitive to the changes occurring inside the concrete during the chloride ions diffusion. Once chloride ions reach the rebar and the alkalinity is lost, the rebar started corroding. During this stage, the changes in the concrete are minimal. This is the reason that the values of $\Delta k/k$ are more or less constant for CVS after the 40th day. In contrary to this, the SBPS can be observed to be highly sensitive once the passive layer breaks down and rebar started corroding. This is because of the fact that the SBPS is directly bonded to the rebar, where the second and third phases predominantly occur. Hence, it may be concluded that the CVS shows a high sensitivity

during the corrosion initiation stage while SBPS shows the same during the later stages namely during the propagation and the cracking phases.

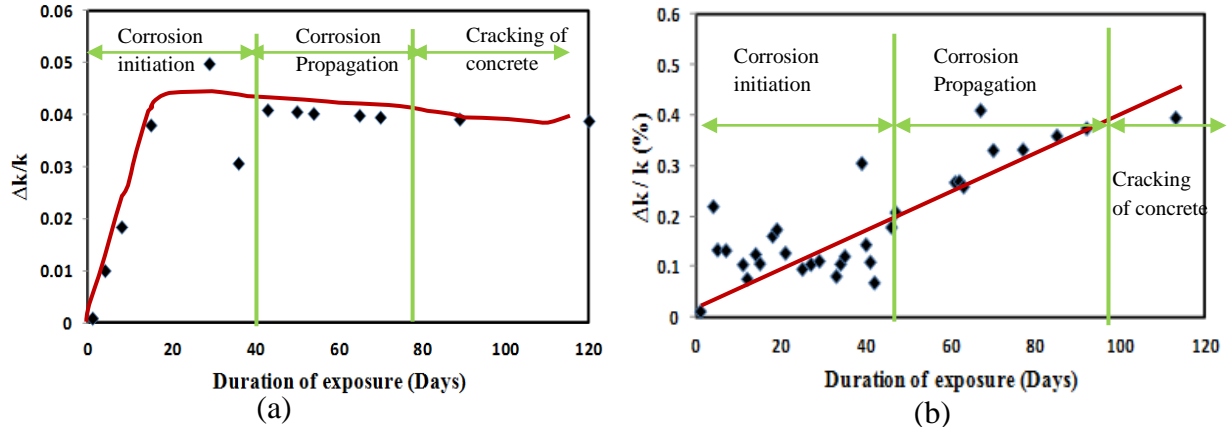


Figure 5.11 Comparison of various phases of corrosion (a) Using CVS (b) Using SBPS

However, together, both CVS and SBPS form complimentary sensors and substantiate each other. It is recommended that in actual field applications, both types of sensors should be used.

5.5 CONCLUDING REMARKS

This chapter presents the assessment of corrosion using embedded CVS. On comparing the conductance signatures and the equivalent stiffness, it may be concluded that the embedded CVS are effective in monitoring the initial changes occurring during the ingress of chloride ions into the concrete. However, once the passive film is broken down and the reinforcement starts corroding, the effectiveness is substantially reduced. The results presented in this chapter very well establish that the same PZT can be either embedded or surface bonded and both the CVS and SBPS complement each other. CVS has been employed here since it is

CHAPTER- 5 Comparison of Rebar Corrosion Assessment Capability of Surface Bonded and Embedded Piezo Sensors

very robust. The PZT patch is very carefully protected against any deterioration by corrosive environment, which might otherwise affect the SBPS. Next chapter presents the diagnosis of carbonation induced corrosion using SBPS.

CHAPTER- 6
**MONITORING AND ASSESSMENT OF CARBONATION
INDUCED CORROSION IN RC STRUCTURES**

6.1 INTRODUCTION

Besides the chloride induced corrosion, the other commonly occurring type of rebar corrosion in RC structures is that induced by the ingress of atmospheric carbon dioxide into concrete, commonly referred as carbonation induced corrosion. The carbonation phenomenon can fill up the pores leading to more durability, however, it makes the alkalinity of the pore fluid drops from a pH value of over 12 to as low as 8, thus providing an ideal environment for corrosion to initiate. Whether chloride induced or carbonation induced, the rebar corrosion is generally accompanied by the loss of rebar cross section and accumulation of corrosion products, which occupy much larger volume than the original steel.

The process of carbonation and its associated reactions are already covered in Chapter 2. This chapter focuses on extending the earlier assessment approach of chloride induced corrosion to carbonation induced corrosion. However, the carbonation induced corrosion operates with a different mechanism. As carbonation progresses, a strengthening of the concrete occurs owing to filling of the concrete pores with calcium carbonate crystals. When the carbonation depth reaches the rebar, a drop in pH renders it highly susceptible to corrosion due to breakdown of the protective passive film formed at higher pH. Compared to chloride-induced corrosion, carbonation is generally a relatively slower process, the initiation phase varies depending upon a number of factors. In a high-quality concrete, it has been estimated that carbonation will proceed at a rate of not more than 1.0 mm per year. The

CHAPTER- 6 Monitoring and Assessment of Carbonation Induced Corrosion in RC Structures

carbonation rate is significantly increased in concrete with a high water-cement ratio, low cement content, short curing period, low strength, and highly permeable or porous paste. Carbonation is also highly dependent on the relative humidity of the concrete. The carbonation rates are highest at a humidity range between 50 % and 75 %. Carbonation-induced corrosion typically occurs on areas of building facades that are exposed to rainfall, shaded from sunlight, and have small concrete cover over the reinforcing steel (Concrete Technology, 2013).

This chapter presents the results of experimental accelerated carbonation corrosion tests performed on RC cylinders with rebars (surface bonded with PZT patch) embedded in concrete to monitor corrosion. The study involved accelerated carbonation tests performed on four cylindrical specimens spanning over 250 days of exposure at Department of Physics, University of Bath UK (under UK India Education and Research Initiative (UKIERI) sponsored Project “Interactive Systems and Coatings for a Sustainable Built Environment”). The corrosion assessment is based on procedure outlined in Chapter 4. The piezo based equivalent stiffness parameter has been primarily relied upon for corrosion assessment. The results are correlated with high resolution microscopic images.

6.2 ACCELERATED CARBONATION STUDY: EXPERIMENTAL PROCEDURE

Four RC cylinders of Grade M30 (IS 456, 2000), were cast with diameters of 25, 35, 45 and 60 mm respectively, and a length 100 mm, as detailed in Table 6.1. The mix design proportions are same as detailed in Table 4.1 of Chapter 4. A single piece of 16 mm diameter HYD steel rebar, grade Fe415, was cast in the centre of each cylinder with a PZT surface bonded to it. The rebar length was 120 mm allowing 20 mm to project out at one end of the

CHAPTER- 6 Monitoring and Assessment of Carbonation Induced Corrosion in RC Structures

cylinder. Out of the four cylinders one specimen was chosen as the reference specimen for the purpose of monitoring carbonation penetration depth through phenolphthalein staining.

Table 6.1 Details of specimens used for accelerated carbonation induced corrosion assessment

Specimen No.	Specimen size	Cover to reinforcement (mm)
1	60 * 100 mm (Control specimen)	22
2	25 *100 mm	4.5
3	35 *100 mm	9.5
4	45*100 mm	14.5

Accelerated carbonation has been used since 1960's (Page, 1988) as carbonation of concrete is relatively slow under natural conditions. After the 28day curing period, the four specimens in the current investigation were placed in a carbonation chamber (as shown in Fig. 6.1). Wax was applied to the base of each cylindrical sample to limit CO₂ through the base. The CO₂ concentration in the chamber was maintained at 5 % under a relative humidity of 75±5 % and temperature of 25 °C. During the accelerated carbonation exposure, the admittance signatures were acquired at frequent intervals throughout the experimental exposure period of 250 days.

Fig. 6.2 shows the initial baseline conductance spectrum of the PZT patches of three specimens, acquired after 28 days of curing, before being subjected to accelerated carbonation. From the figure, it can be observed that with the decrease in the diameter of the specimen, the conductance signature's peak tend to become sharper and at the same time occurs at a higher frequency. The higher resonance peak frequency for the smaller diameter

specimen indicates that the PZT patch identified the specimen to be stiffer as compared to the larger diameter specimen. This observation is attributed to the increasing influence of the concrete cover, which has a lower stiffness and contributes a higher damping, as the cover to reinforcement ratio increases from Specimen 2 to 4.

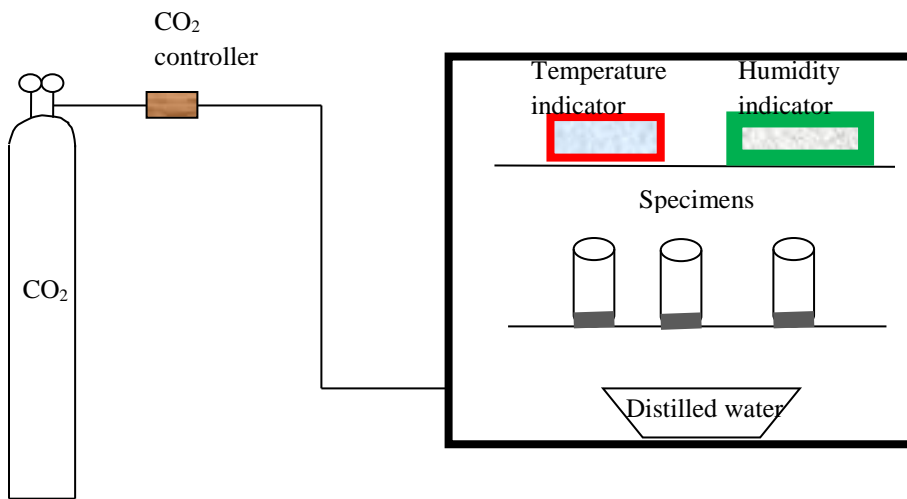


Figure 6.1 Carbonation chamber and test set up

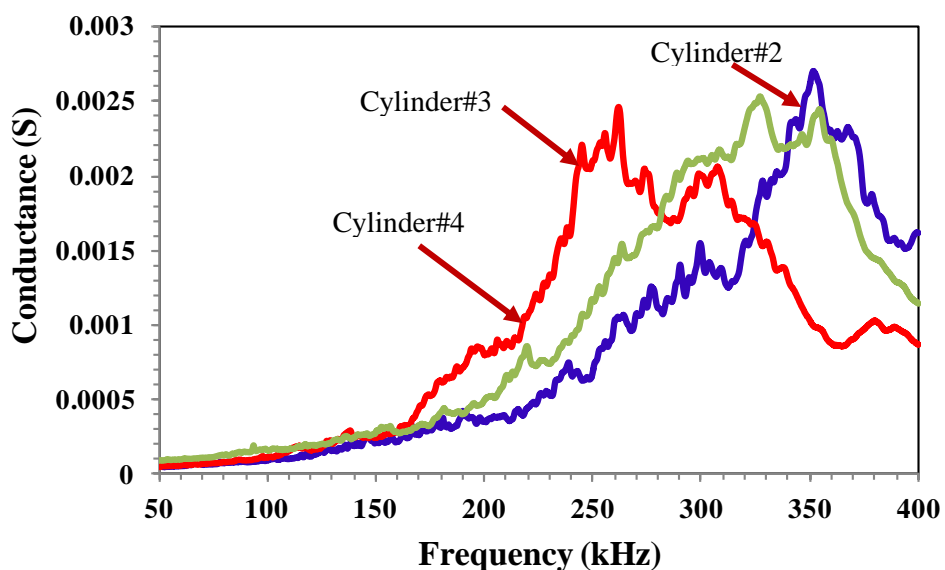


Figure 6.2 Baseline conductance signatures of PZT patch embedded in RC cylindrical specimens

At any stage during the CO₂ exposure, in order to measure the carbonation penetration depth, a slice was cut from the reference specimen and the fracture surface was sprayed with a saturated solution of phenolphthalein indicator in ethanol. At high pH (uncarbonated) the indicator has a bright pink colour. However, below a pH of 8.6 (carbonated material) it becomes colourless. The interface between pink and colourless regions indicates the carbonation front. In the present study, a small slice of 50 mm thick from the bottom was cut from the reference specimen, as shown in Fig. 6.3. Maximum and minimum depth of carbonation was measured and numerically averaged. The carbonation penetration depth was periodically measured using the phenolphthalein method by cutting such slices from the reference specimen, as detailed in Table 6.2.

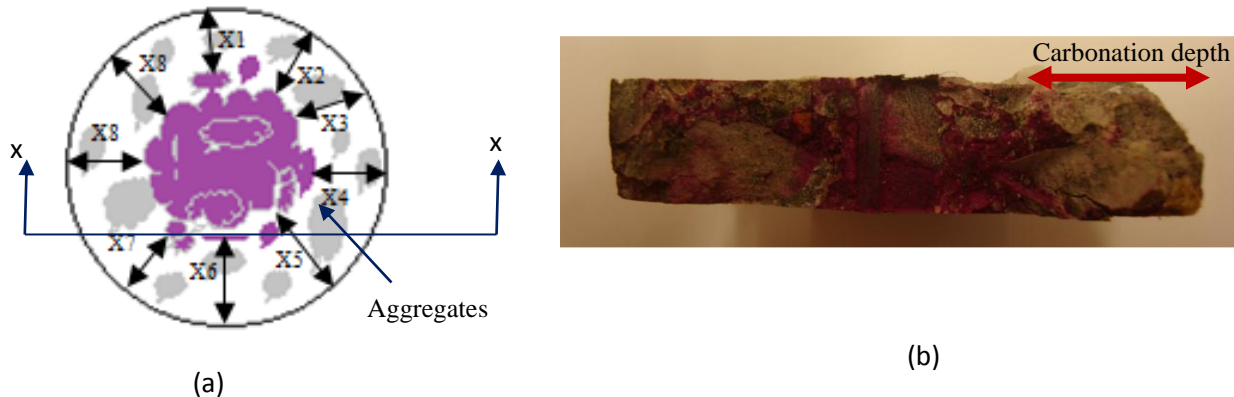


Figure 6.3 Phenolphthalein test (a) Schematic diagram representing the depths of carbonation (b) 5 mm slice sprayed with phenophthalein indicator

Table 6.2 Phenolphthalein test results

No. of days	Carbonation depth (mm)
20	2.5
30	12
40	15

6.3 ANALYSIS OF RESULTS

Fig. 6.4 (a, b and c) shows the conductance spectrum of the bonded PZT patches for the three specimens during the exposure period. It is noteworthy that the specimens were 28 days old and the majority of the hydration processes, which are expected to influence the conductance spectrum, are considered completed. As seen from the figures, the resonance peaks of the conductance signature have changed for all the three specimens with increasing carbonation.

Fig. 6.5 (a, b and c) show the variation of the RMSD index of the three specimens with exposure period.

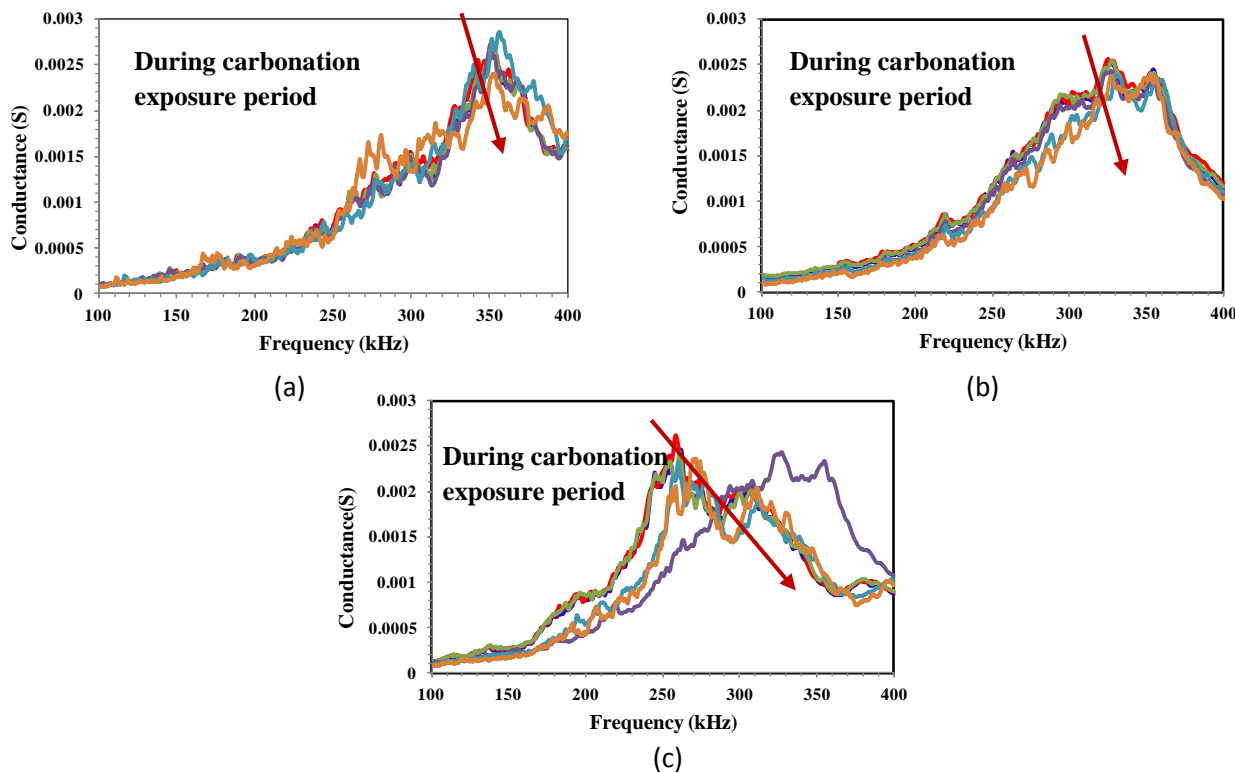


Figure 6.4 Variation of conductance signatures during accelerated corrosion process
 (a) Specimen 1 (b) Specimen 2 (c) Specimen 3

The RMSD values increased during the exposure period, which show that the conductance signatures captured the changes occurring during that period in a good manner.

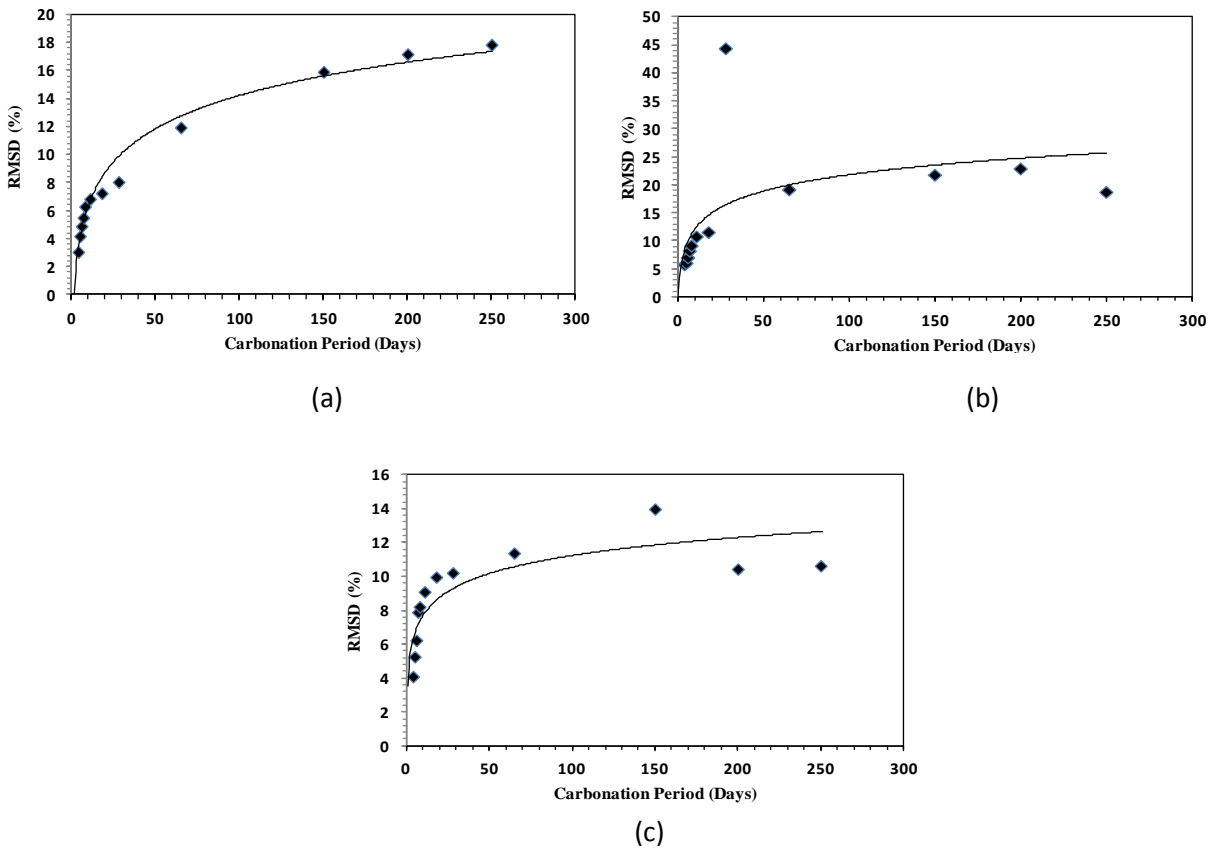


Figure 6.5. Variation of Variation of RMSD index during accelerated corrosion process
 (a) Specimen 1 (b) Specimen 2 (c) Specimen 3

To gain further insight into the corrosion mechanism, equivalent structural parameters were extracted from the impedance spectrum outlined in chapter 3. In the frequency range of 150-250 kHz system behaviour was similar to the one identified in Chapter 4 (for SBPS one). Fig. 6.6 shows the comparison between the experimental plots with the analytical one, based on which the system is identified as parallel spring-damper-mass (k - c - m) combination. Using the already derived equations (Chapter 4), the equivalent stiffness was calculated and plotted. Fig. 6.7 displays the effect of corrosion on the identified ESP.

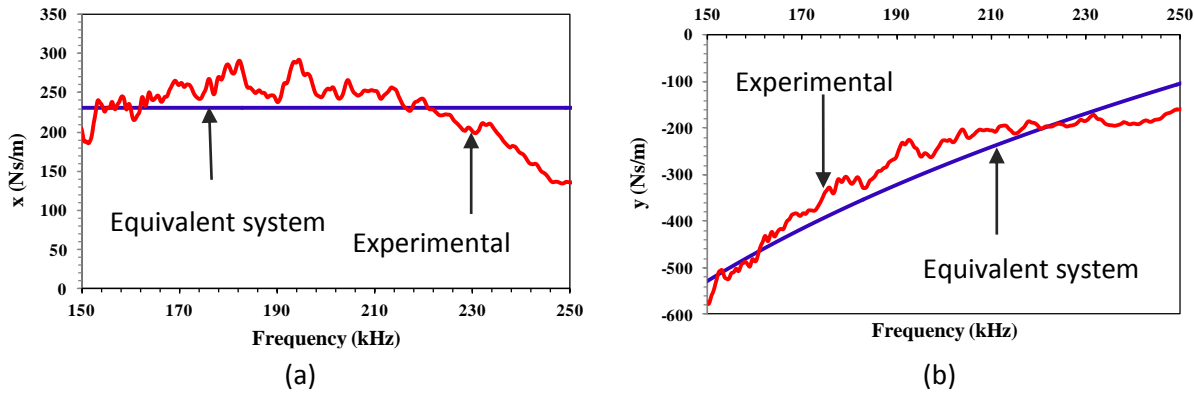


Figure 6.6 Comparison of experimental plots of x and y with those of identified system for typical specimen 1

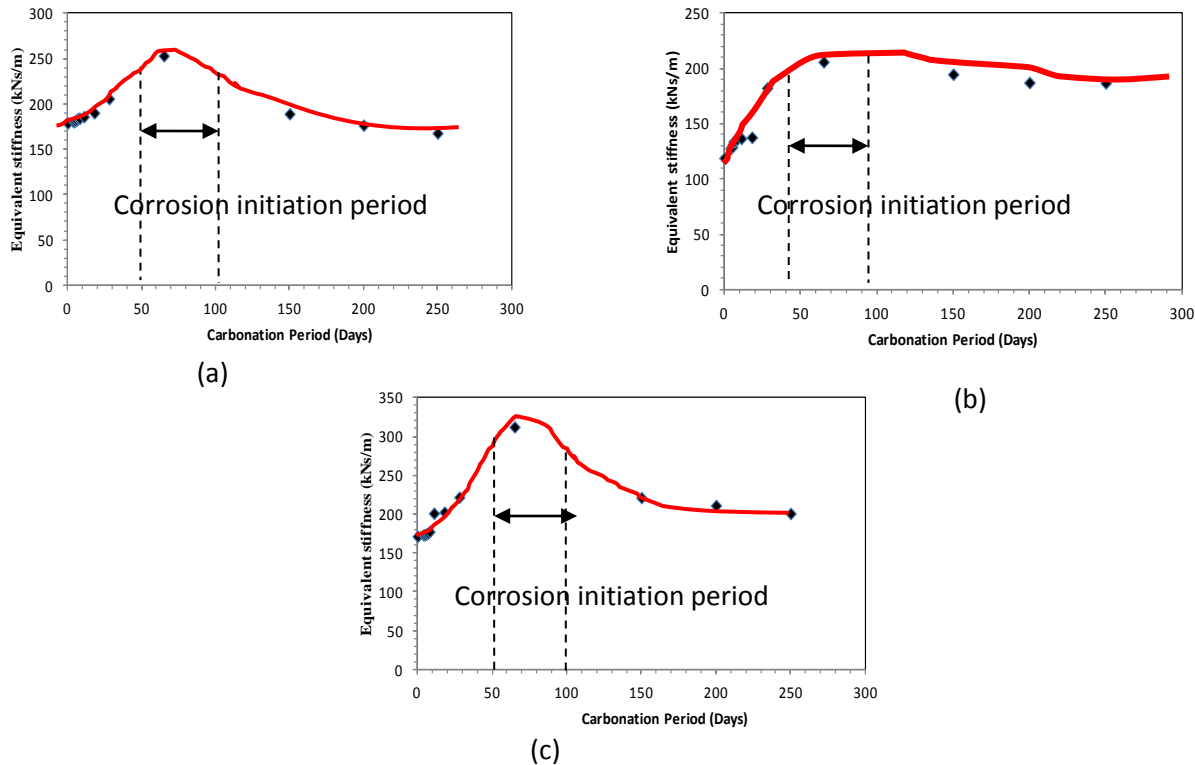


Figure 6.7 Variation of equivalent stiffness during accelerated corrosion process
 (a) Specimen 1 (b) Specimen 2 (c) Specimen 3

The figures show an initial increase in ESP for all the three specimens. This increase is attributed to calcium carbonate formed during carbonation of the cement phase filling the

pores and leading to an increase in stiffness. However, once the carbonation front reached the steel/concrete interface, a reduction in alkalinity and subsequent breaking down of the passive film is expected to trigger corrosion. The greater volume of the corrosion products would induce stresses in the adjacent concrete material leading to the formation of micro cracks and a decrease in ESP values. Hence, the phase where the ESP value tends to decrease is believed to indicate the corrosion initiation period. From these plots, this period works out to be in between 50-90 days for all the specimens. This is confirmed from the phenolphthalein test results. When seen together with Table 5.2, it can be noted that carbonation reached the rebar surface after 20-25, 25-30 and 40 days for Specimens 2, 3 and 4, respectively. Hence, the plateau region of ESP occurred definitely after CO₂ reached the rebar. Further confirmation of this fact is covered in the next section by means of image analysis.

Non dimensional stiffness loss ($\Delta k/k$) was also determined, to differentiate the two phases of corrosion, namely ingress of carbon dioxide through the pores and corrosion initiation. Fig. 6.8 (a, b and c) shows the variation of ($\Delta k/k$) with the exposure period. From the figures it can be observed that for smaller diameter specimen the carbonation initiation had started when the $\Delta k/k$ value reaches 0.3. As the diameter of the specimens increases (thereby increasing the cover to steel) it could be noted that the $\Delta k/k$ values for carbonation initiation have also increased to 0.4 and 0.45 respectively. Hence, this feature of ESP based diagnosis clearly gives it leverage over the conventional statistical diagnostics such as RMSD.

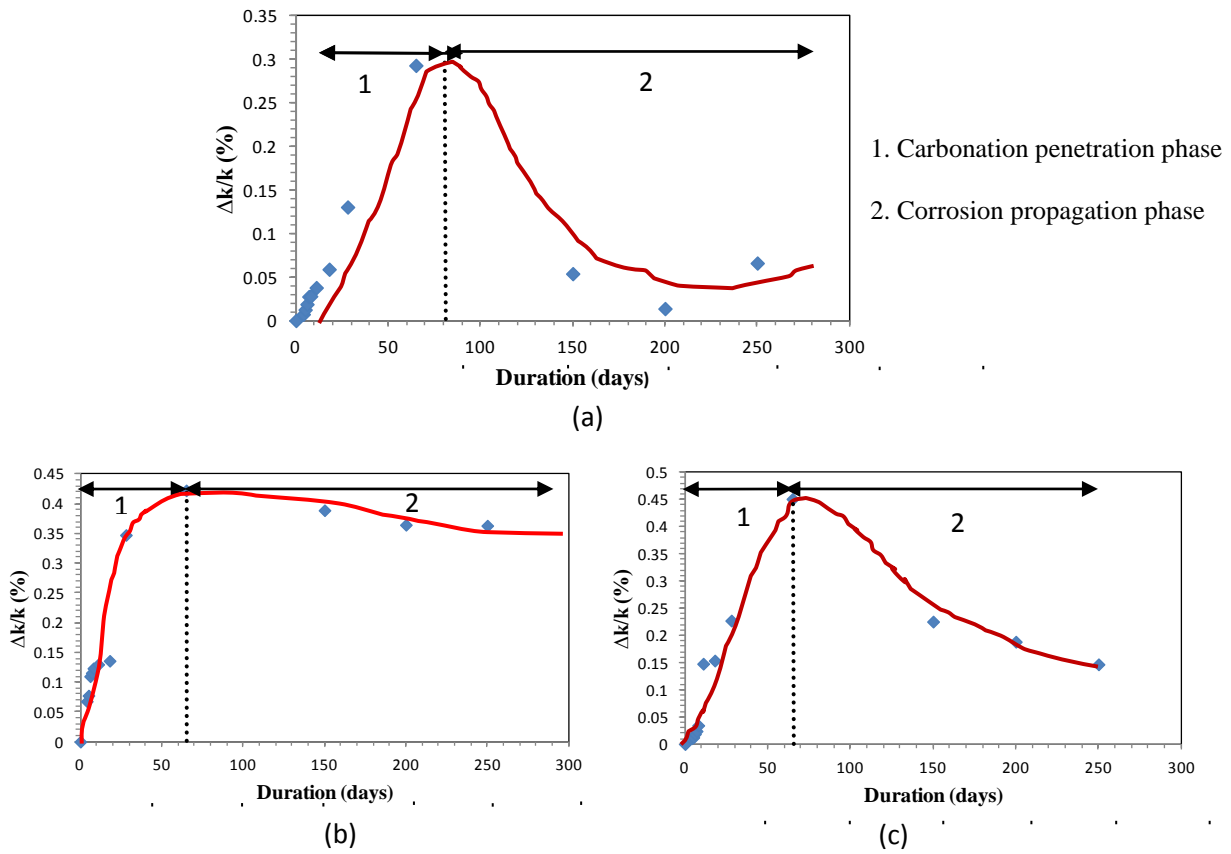


Figure 6.8 Variation of $\Delta k/k$ during accelerated corrosion process
 (a) Specimen 1 (b) Specimen 2 (c) Specimen 3

The equivalent mass parameter (EMP) has been used for determining the rate of corrosion using the model developed in Chapter 4, given as

$$\left(\frac{\Delta m}{m}\right)_{actual} = \Lambda_m \left(\frac{\Delta m}{m}\right)_{PZT} \quad (6.1)$$

where Λ_m is a mass constant equal to 0.54 from findings reported in Chapter 4. The corrosion rates for all the specimens were calculated and tabulated in Table 6.3 after an accelerated carbonation exposure period of 250 days. Compared to chloride induced corrosion in general, this value is not very high and can be pronounced as a low rate of corrosion.

Table 6.3 Corrosion rate values (without considering Λ_m)

Specimen No.	Corrosion rates using PZT identified mass loss after incorporating Λ_m (mm/year)
1	0.332
2	0.676
3	0.135

The important point to be noted for this approach is that both the equivalent stiffness and equivalent mass has been obtained non-destructively, circumventing the measurement of absolute stiffness or mass.

6.4 CORRELATION WITH MICROSCOPIC IMAGE ANALYSIS AND RAMAN ANALYSIS

To verify the nature of changes highlighted by the ESP, complementary analytical techniques including optical microscopy, scanning electron microscopy and Raman spectroscopy were applied to representative cross sections of representative samples. The sections were cut after 250 days from the beginning of the test. In order to produce high quality polished sections and reduce the possibility of breaking the samples, the end of each cylinder was embedded in low-viscosity resin at atmospheric pressure prior to polishing.

The sections were, then, cut perpendicularly to the cylinder axis (parallel to the base) using a diamond impregnated cutting disc, in dry conditions. The surface of each section was subsequently ground using progressively finer silicon carbide papers from 180 to 1200 grit size before polishing with 6, 3 and 1 micron diamond paste. A final polish was achieved using colloidal silica suspension. Optical inspection of the polished sections was carried out

CHAPTER- 6 Monitoring and Assessment of Carbonation Induced Corrosion in RC Structures

using a Leica DM ILM inverted metallurgical microscope equipped with an Infinity 1 digital camera at department of Physics, University of Bath, UK. Images of the sections were acquired using Studio Capture Software version 4.0.1. Visual inspection using the microscope and images of the sections showed several radial cracks evolving from the rebar. This phenomenon is in agreement with the effects of concrete cancer. Fig. 6.9 shows typical cracking in Specimen 2 (2.5cm diameter). Several cracks (black areas) are visible, propagating from the rebar (upper part of the image) towards the external surface (lower part). Cracks often follow the interface between aggregate and cement matrix. The images correlate well with the ESP values as shown in Fig. 6.9. As it can be seen in the SEM image (on the right side) of Fig. 6.9 calcium carbonate crystals filling up the pores due to which the ESP values increased on account of stiffening action. Once the carbonation initiates and steel starts corroding thereby developing cracks on the surface (as shown in the optical image of Fig. 6.9) this resulted in the decrease of equivalent stiffness values. Thus, the ESP identifies the changes occurring during the carbonation induced corrosion correlate well with the imaging analysis.

To investigate these structural changes further, a microstructural analysis of the cement matrix was carried out using a Field Emission Scanning Electron Microscopy (FESEM) JEOL model FE-SEM-6301F. This microscope can image at low accelerating voltages (1-5 KV) and, consequently, it is possible to achieve high magnifications reducing at the same time the charge effect in non-conductive samples. The analysis was performed on a few fragments of cement taken from the same sections. The fragments were attached to the SEM sample stub using double sided carbon sticky tape and were analysed in the as received condition (i.e. without coating with a conductive material).

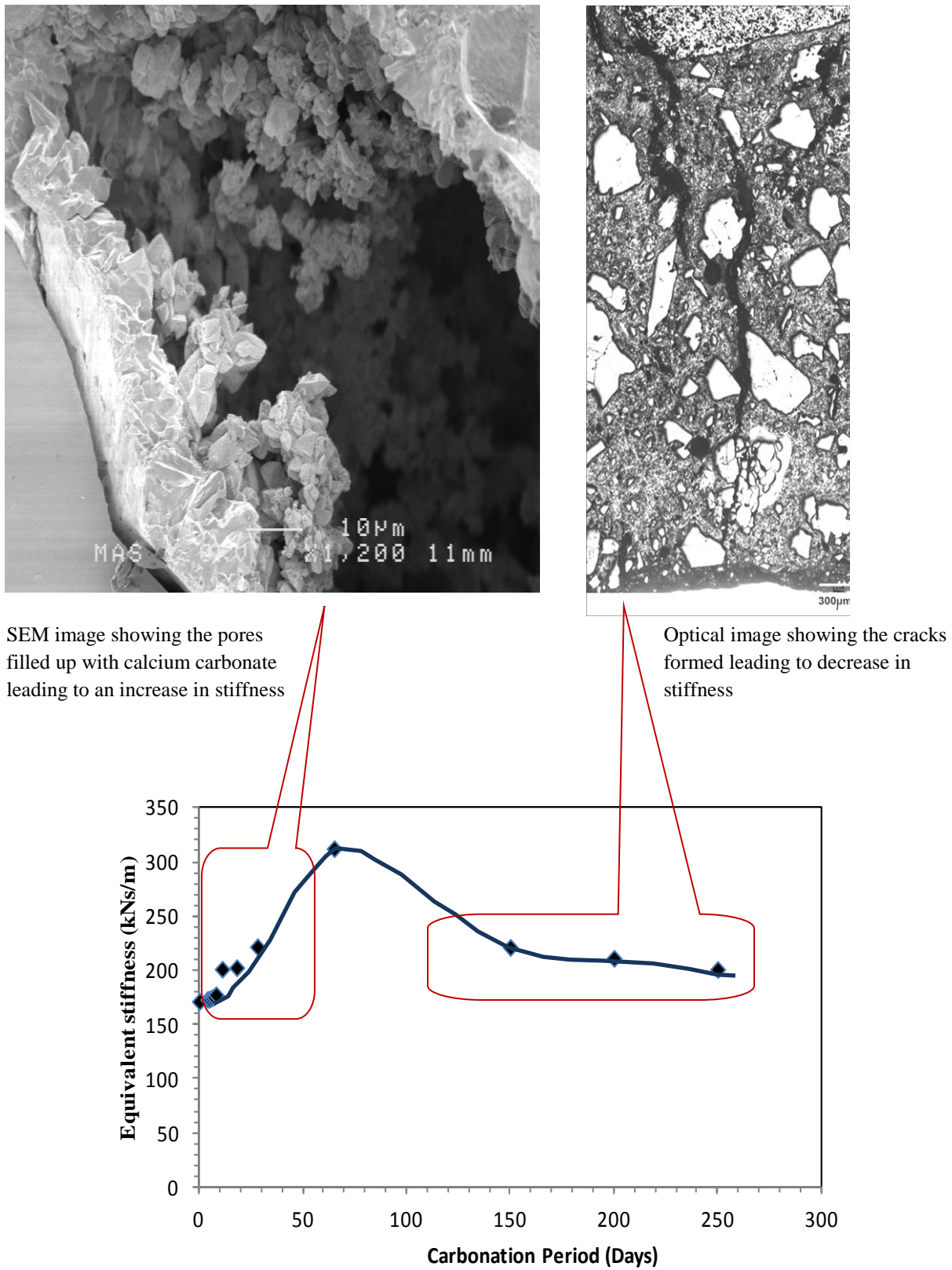


Figure 6.9 Correlation of ESP values with SEM and optical images.

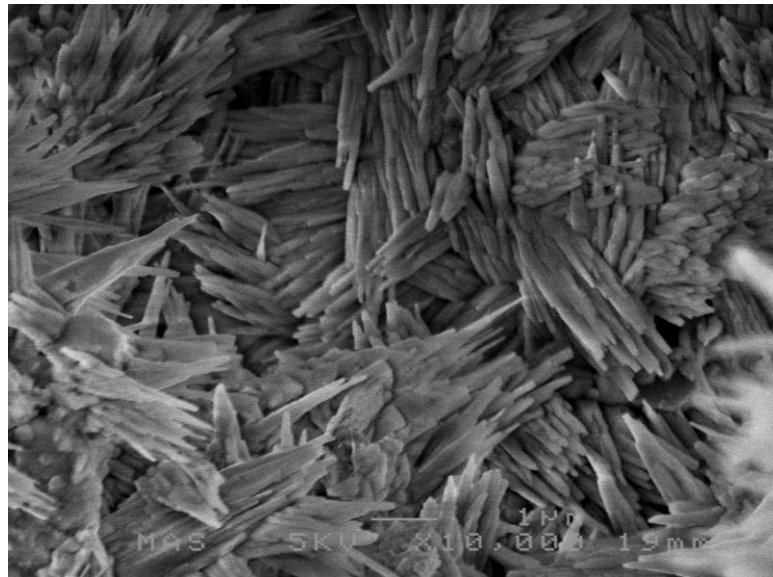


Figure 6.10 SEM image showing fine interlaced silicate needles forming dense structure.

Fig. 6.10 shows typical surface of one of these fragments taken from the specimen 2. The image highlights a tight network of fine interlaced silicate needles (CSH) that form a very dense structure. Crystals of calcium carbonate with scalenohedral habit were identified on the internal surfaces of the pores. This finding is in agreement with the degradation process previously described for the rebar corrosion induced by carbonation.

To verify the nature of the oxides formed on the rebar surface (which, through expansion led to the formation of the cracks identified during the analysis with the optical microscope), analysis was performed using Raman spectroscopy of the metal phase located at the cement/rebar interface (box in Fig. 6.11).

A Renishaw inVia Raman Spectrometer with a laser of wavelength 532 nm (green visible light) was used. The laser was set at 100% of the power; scan was performed between 100 and 3200 cm⁻¹ with only one accumulation and an exposure time of 10 seconds. A WiRE

software version 3.4 developed by Reinshaw was used to set the experiment and acquire the spectra.

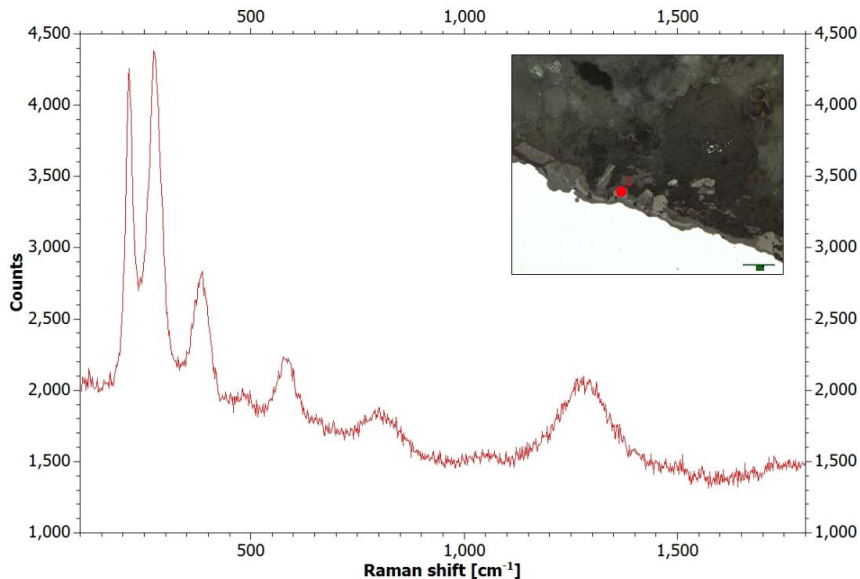


Figure 6.11 Raman spectrum of α -hematite (Fe_2O_3) oxide layer on steel rebar. Inset shows optical image of polished section and location of analysis.

Fig. 6.11 shows one of these spectra with the corresponding location along the interface highlighted by a red dot in the box (upper left corner). Peaks in the spectrum are located at 220, 278, 390, 486, 582, 804, 1058, 1280 cm⁻¹. Oh et al. (1998) attributed the peaks at 220, 278 and 1280 to hematite α - Fe_2O_3 . It is already known, in fact, that depending on the crystallinity and grain size, characteristic doublet at 294/225 cm⁻¹ of this mineral in some cases shifts downward in wave number (Wang et al. 1998). Peaks at 390, 486 and 582 attributed to goethite α - FeOOH (Oh et al., 1998). Both these phases are common in the corrosion products associated with rebar corrosion.

6.5 VALIDATION OF CORROSION RATE PREDICTION MODEL

In the previous section equivalent mass model developed in Chapter 4 through accelerated chloride induced corrosion was applied to determine the rate of corrosion for carbonation induced corrosion. To validate this gravimetric measurement were performed. The specimens were split open and the rebar was removed after 250 days of exposure to enable mass loss measurements. The mass loss of the steel bars was determined after chemically cleaning the corrosion products as described in ASTM G1-03. The initial mass before embedding and final mass after removing the rebar from cylinder was determined for all the three rebars. From the mass loss, the corrosion rate is calculated as described in ASTM G1-03 using the Eq. (4.11). The actual corrosion rates using the mass losses determined are tabulated in Table 5. Upon comparing the actual corrosion rates with the corrosion rates calculated using PZT identified mass loss (see Table 6.4), it was found that using the equivalent mass model, the corrosion rates can be calculated with reasonable accuracy (average error of 11 % only). This circumvents the determination of actual mass loss, which in practice is unfeasible”.

Table 6.4 Corrosion rate values (considering Δ_m)

Specimen	Actual corrosion rates using gravimetric mass loss (mm/year)	Corrosion rates using PZT identified Mass loss after incorporating Δ_m (mm/year)	Percentage error
2	0.059	0.067	12.6
3	0.048	0.052	9.1
4	0.011	0.013	13.4

6.6 CONCLUDING REMARKS

This chapter has presented a new and simple approach for monitoring the process of carbonation induced corrosion in RC structures right from initiation to rebar corrosion based on the ESP extracted out from the admittance signatures of PZT patches surface-bonded to the rebars. The ESP extracted out from the admittance signatures of surface-bonded PZT patch on the rebar is established as the solely required carbonation progression as well as rebar corrosion indicator. ESP correlates very well with the phenolphthalein test results as well as microscopic image analysis in identifying the onset of corrosion. The most promising feature of the proposed approach is that the two main phases in the process, namely carbonation penetration through concrete cover and corrosion initiation are clearly demarcated. The proposed approach is non-destructive in nature and fully autonomous. The empirical correlation derived from the PZT patches can be utilized in carbonation induced corrosion of rebars in real-life RC structures, where they are not exposed for direct visual check.

6.7 ACKNOWLEDGEMENTS

The authors gratefully acknowledge the support provided by UK India Education and Research Initiative (UKIERI) sponsored Project “Interactive Systems and Coatings for a Sustainable Built Environment” in conducting the carbonation experiments at Department of Architecture and Civil Engineering, University of Bath, UK.

CHAPTER- 8

CONCLUSIONS AND RECOMMENDATIONS

8.1 INTRODUCTION

The aim of this research was to extend the application of the EMI technique (using PZT sensors) for corrosion assessment of rebars in RC structures, especially utilizing the equivalent structural parameters for development of corrosion damage model.

The major novelty in the present thesis is that for the first time, such an extensive studies on the application of the equivalent structural parameters for corrosion assessment of rebars in RC structures have been investigated and related empirical corrosion assessment models have been developed. This chapter draws conclusions and gives some ideas about future work that would complement the material presented in this thesis.

8.2 RESEARCH CONCLUSIONS AND CONTRIBUTIONS

The original research contributions of this thesis mainly consist of development of a new corrosion assessment model based on the equivalent structural parameters, for both chloride and carbonation induced corrosion in rebars, thereby circumventing the determination of actual structural parameters, which are either very difficult or impossible. Major research conclusions and contributions can be summarized as follows

1. As a first step, the effect of corrosion on the admittance signature has been studied on bare steel bar specimens with surface bonded PZT patch, subjected to accelerated chloride induced corrosion. The mechanical impedance has been observed to change due to corrosion progression, which is reflected as a change in the conductance

- signatures for all the specimens. With the advancement of corrosion, the slope of the y vs ω^{-1} curve has been found to decrease consistently, which is more consistent than the trend of the RMSD indices which were used earlier to quantify damage.
2. After satisfactory results on the bare steel bar, the experiments have been extended to rebar embedded into concrete i.e., RC specimens. The peaks of the conductance signature for RC specimens have been observed to reduce considerably during the accelerated corrosion process, which is attributed to the increase of damping on account of the formation of corrosion products.
 3. The structural systems have been identified based on the plots of real and imaginary components of mechanical impedance as (i) Bare steel bar specimens: *Kelvin-Voigt* system and series combination of spring, mass and damper (ii) RC specimens: parallel combination of spring, mass and damper; for both types of corrosion: chloride induced and carbonation induced, which showed consistent results.
 4. Compared to the variation of the RMSD index based on the raw conductance signatures, the observed variation in identified equivalent structural parameters ' c ', ' k ' and ' m ' extracted from the impedance spectrum are more consistent and exhibit considerably lesser uncertainty.
 5. The equivalent stiffness model can be directly used in an actual scenario, to provide real time information about level of corrosion induced damage non-destructively and can be a substitute to the conventional electro-chemical techniques. The various phases of corrosion have been identified with the developed model and concluded that a value of $\Delta k/k$ over 0.2 indicates initiation of corrosion and values over 0.4 indicates alarming corrosion level. Similarly, equivalent mass model can be directly

used to determine the corrosion rate, with no requirement of determining the absolute mass of the specimen. On comparing the corrosion rates using the developed mass model and the corrosion rates using conventional gravimetric, it is found that the PZT identified mass loss can easily substitute the actual mass loss determination, thus circumventing the use of actual mass loss, which is in fact practically not feasible.

6. The feasibility of utilizing the embedded sensors has also been investigated and on comparing the surface bonded sensors and embedded sensors, it may be noted that the embedded CVS are able to effectively track the changes occurring during initial stages of corrosion. The surface bonded sensors show higher sensitivity after the corrosion initiation. Hence, they can complement each other for effective corrosion monitoring
7. The equivalent stiffness model developed for chloride induced corrosion is also effective in tracking the changes due to carbonation. The initial stiffening effect caused due to filling of pores of cement paste by calcium carbonate (values of $\Delta k/k$ found to increase during this period) is clearly observed in the plots, which correlate well with the phenolphthalein tests and imaging results.
8. The lab study is an accelerated corrosion process has resulted in the development of a model in few months time which otherwise would have taken several years. Based on this model, a correlation between accelerated corrosion test data and natural corrosion data has been made. It is found that the developed model is effective in identifying the corrosion rate in natural environmental conditions. Even though a reasonable correlation is presented here, more long term investigations are required to ascertain

- the relationship especially for other two phases of corrosion, which however is beyond the scope of present thesis.
9. As an application, the developed models have been utilized to study reinforcement corrosion in FA blended concrete. From the results, it can be concluded that 25% FA replacement is effective in resisting the corrosion.
10. From the experimental investigations, it can be concluded that PZT materials, which belong to the category of “smart materials” can be used for effective corrosion sensor technology. Although the tests reported in this study were carried out on M30 grade concrete and HYSD bars of small size, the dimensionless parameters represented can also be conveniently used for life-sized structures, since the zone of influence of the PZT patches is usually very small in concrete.

This research work attempted to take the EMI based SHM technique, which otherwise is signature based in nature, a step forward by making the method model-related and thus providing quantitative SHM.

8.3 LIMITATIONS

The empirical relations developed as a part of proposed models will depend on the type and size of the PZT patches and type and thickness of the bonding layer. Hence, dimensionless parameters cannot be considered as a universal relationship. Therefore, it is recommended that similar calibration should be first established in the laboratory for the particular concrete-steel-PZT-bond layer combination before using the method in the field.

8.4 RECOMMENDATIONS FOR FUTURE

The following tasks are recommended to be undertaken to continue the research further

1. The present work was carried out on normal strength concrete; the same can be extended to high strength concrete and using different grades of steel.
2. The developed corrosion model can be validated, based on the measurements of corrosion from real life structures for long term effects, spanning at least for ten years, so as to cover the corrosion propagation and cracking phase.
3. The equivalent parameters developed can be compared with analytical results for simple structures.
4. The impedance data can be further correlated with the conventional electro-chemical techniques.
5. Research may focus on Remaining Service life prediction of the RC structure based on the developed models for chloride and carbonation induced corrosion.

The author strongly believes that there is a strong potential in developing the EMI technique using PZT sensors as a NDE technique for corrosion assessment, which can be possibly provide better assessment than the conventional electro-chemical techniques.

PUBLICATIONS BASED ON THIS RESEARCH

INTERNATIONAL JOURNALS

1. **Talakokula, V** and Bhalla, S. (2011), "Detection and Quantification of Rebar Corrosion Using Impedance Method" *International Journal of Earth Sciences and Engineering*, ISSN0974-5904, 4 (6), 889-891.
2. **Talakokula, V.,** Bhalla, S. and Gupta, A. (2014), "Corrosion Assessment of Reinforced Concrete Structures Based on Equivalent Structural Parameters Using Electro-Mechanical Impedance Technique", *Journal of Intelligent Material Systems and Structures*, Volume 25 (4), pp 484-500.
3. **Talakokula, V.,** Bhalla, S. and Gupta, A. (In press), "Comparison of Rebar Corrosion Assessment Capability of Surface Bonded and Embedded Piezo Sensors". *Journal of Intelligent Material Systems and Structure*, DOI: 10.1177/1045389X14554133.
4. **Talakokula, V.,** Bhalla, S., Ball, R. J., Pesce, G. L., Kurchania, R., Bowen, C. R., Paine, K., Bhattacharjee, B. and Gupta, A. (Under Review), "Diagnosis of Carbonation Induced Corrosion Initiation and Progression in RC Structures Using Piezo-Impedance Transducers. *Corrosion Science*.
5. **Talakokula, V.,** Bhalla, S. and Gupta, A. (Under Review), "Monitoring the Early Age Hydration of Concrete Using Equivalent Structural Parameters Identified by PZT Patches via Electromechanical Impedance Technique", *Cement and Concrete Research*.
6. **Talakokula, V.,** Bhalla, S. and Gupta, A. (Under preparation), "Correlation of SEM and EDX Analysis with Impedance Data for Chloride and Carbonation Induced Corrosion in RC Structures".

-
-
7. **Talakokula, V.**, Bhalla, S. and Gupta, A. (Under preparation), “Corrosion Assessment in Fly ash Blended Concrete Structures”.

INTERNATIONAL CONFERENCES

1. **Talakokula. V**, Bhalla. S and Gupta. A, (Accepted) “Detection of Chloride and Carbonation Induced Corrosion in RC Structures Using Piezo Sensors via EMI Technique”, *International Conference on Concrete Solutions 2014*, To be held at Queen’s University, Belfast, September 1-3, 2014.
2. **Talakokula. V**, Bhalla. S and Gupta. A, (2014) “Recent Trends in Reinforcement Corrosion Assessment Using Piezo Sensors via Electro Mechanical Impedance Technique”, *Proceedings of the International Conference on Smart Structures/NDE*, held at Sandiego, California, US, March 9-13, 2014. Sensors and Smart Structures Technologies for Civil, Mechanical, and Aerospace Systems 2014, edited by Jerome P. Lynch, Kon-Well Wang, Hoon Sohn, Proc. of SPIE Vol. 9061, 906139, doi: 10.1117/12.2041654.
3. **Talakokula. V**, Bhalla. S and Gupta. A, (2013) “Detection Of Chloride And Carbonation Induced Corrosion In RC Structures Using Piezo Sensors Via EMI Technique”, *Proceedings of the International Conference on Trends and Challenges in Concrete structures*, Ghaziabad, UP, India, December 19-21, 2013, pp 590-597.
4. **Talakokula, V** and Bhalla, S. (2013), “Carbonation Corrosion Assessment in Reinforcement of Normal and Fly ash Concrete Using Piezo Sensors”, *Proceedings of the International Corrosion Conference and Expo-2013,(CORCON 2013)*, 30 Sep-4 Oct 2013, New Delhi, R23.

-
-
5. **Talakokula, V** and Bhalla, S. (2013), “Experimental Study to Detect Corrosion in RC Structures Using Piezo-Ceramic Sensors”, *Proceedings of the International Conference on Innovations in Concrete Construction*, UKIERI Congress, 5-8, March, Jhalandhar, India, 1454-1461.
 6. **Talakokula, V** and Bhalla, S. (2012), “Early Detection of Corrosion in RC Structures Using EMI Technique”, *Proceedings of the International Corrosion Conference and Expo-2012*, (CORCON 2012), 26-29 Sept, Gao, 2012, R113. (**Awarded best paper**).
 7. **Talakokula, V.**, Bhalla, S., Nitya, J., Mansi, J., Harmohan, S., Sindhu, G. (2012) “Piezo Ceramic Transducers for Reinforcement Corrosion Monitoring in RCC Structures Using Electro-Mechanical Impedance Technique”, *Proceedings of the International Conference on Recent Trends in Advanced Materials*, 20-22 Feb, VIT University, Vellore, 2012. 124-129 (**Awarded as best poster**).
 8. **Talakokula, V** and Bhalla, S. (2011), “Detection and Quantification of Rebar Corrosion Using Impedance Method” *Proceedings of International conference on Advances in Civil Engineering*, ACE-2011, 21-23 October, KLU, Vijayawada, 2011, 889-891.
 9. **Talakokula, V** and Bhalla, S. (2010), “Review of Impedance Based Structural Health Monitoring”, *Proceedings of the 6th international conference on Vibration engineering and Technology of Machines*, 13-15 December, IIT Delhi 2010, 550-557.

OTHER PRESENTATIONS/WORKSHOPS

1. Corrosion Assessment of RC Structures Using Piezo Sensors, Technical lecture organized by Indian Association of Structural Engineers at Indian Habitat Centre, 31st October 2013.

-
-
2. Rebar Corrosion Assessment in RC Structures using Piezo-Transducers at Workshop on Experimental Structural Dynamics, Structural Health Monitoring and Non-Destructive Evaluation Using Smart Materials, IETE, New Delhi, 26th October 2013.
 3. Development of New Corrosion Assessment Technique Based on Piezo-Transducers during National Science Day, IIT Delhi.
 4. Detection of Chloride and Carbonation Induced Corrosion in RC Structures Using Piezo Sensors via EMI Technique at International Workshop on Interactive Systems, Nanosolar Photovoltaics and Coatings for a Sustainable Built Environment, MANIT Bhopal, 10-11, JANUARY,2013.

REFERENCES

1. ACI Committee 226.3 R. (1987), “Use of Fly Ash in Concrete”, *ACI Materials Journal*, 84, 381–409.
2. Agilent Technologies. (2012) www.Home.agilent.com.
3. Ahmad, S. and Bhattacharjee, B. (1995), “A Simple Arrangement and Procedure For In-Situ Measurement of Corrosion Rate of Rebar Embedded in Concrete”, *Corrosion Science*, 37(5), 781–91.
4. Alonso, C., Andrade, M., Izquierdo, X. R., Nóvoa, M. C. and Pérez. (1998), “Effect of Protective Oxide Scales in the Macrogalvanic Behaviour of Concrete Reinforcements”, *Corrosion Science*, 40, 1379-1389.
5. Ampadu, K. O., Toril, K. and Kawamura, M. (1999), “Beneficial Effect of Fly Ash on Chloride Diffusivity of Hardened Cement Pastes”, *Cement and Concrete Research*, 29, 585–90.
6. Annamdas, V. G. M. and Soh, C. K. (2006), “Embedded Piezoelectric Ceramic Transducers in Sandwiched Beams”, *Smart Materials and Structures*, 15(2), 538-545.
7. Annamdas, V. G. M., Yang, Y. W. and Soh, C. K. (2010), “Impedance Based Concrete Monitoring Using Embedded PZT Sensors”, *International Journal of Civil and Structural Engineering*, 1(3), 414-424.
8. Annamdas, V. G. M. and Yang, Y. W. (2012), “Practical Implementation of Piezo-Impedance Sensors in Monitoring of Excavation Support Structures”, *Structural Control and Health Monitoring*, 19, 231–245.
9. Annamdas, V. M. and Radhika, M. A. (2013), “Electromechanical Impedance of Piezoelectric Transducers for Monitoring Metallic and Non-Metallic Structures: A

Review of Wired, Wireless and Energy-Harvesting Methods”, *Journal of Intelligent Material Systems and Structures*, 24 (9), 1021-1042.

10. Andrade, C. and Alonso, C. (1996), “Corrosion Rate Monitoring in the Laboratory and on Site”, *Construction and Building Materials*, 10 (5), 315–328.
11. Andrade, C. Alonso, J. Gulikers, R. Polder, R. Cigna, O. Vennesland, M. Salta, A. Raharinaivo, B. Elsener. (2004), “Electrochemical Techniques for Measuring Metallic Corrosion” Test Methods for On-Site Corrosion Rate Measurement of Steel Reinforcement in Concrete by Means of the Polarization Resistance Method”, *Materials and Structures*, 37, 623–624.
12. ASTM C876-91 (1999), “Standard Test Method for Half-Cell Potentials of Uncoated Reinforcing Steel in Concrete”, *West Conshohocken*, PA.
13. ASTM C618-12a (2006), “Standard Specification for Coal Fly Ash and Raw or Calcined Natural Pozzolana for Use in Concrete”, *West Conshohocken*, PA.
14. ASTM G I -03 (2012) “Standard Practice for Preparing, Cleaning and Evaluating Corrosion Test Specimens”, *West Conshohocken*, PA.
15. ASTM G193-12D (2012), “Standard Terminology and Acronyms Relating to Corrosion”, *ASTM International*, *West Conshohocken*, PA.
16. Atis, C. D. (2002), “Accelerated Carbonation and Testing of Concrete Made With Fly Ash”, *Construction and Building Materials*, 17, 147-152.
17. Baptista, F. G., Filho, J. V. and Inman, D. J. (2010), “Influence of Excitation Signal on Impedance-Based Structural Health Monitoring”, *Journal of Intelligent Material Systems and Structures*, 21 (14), 1409-1416.

-
-
18. Baptista, F. G., Filho, J. V. and Inman, D. J. (2012), “Real-Time Multi-Sensors Measurement System With Temperature Effects Compensation for Impedance-Based Structural Health Monitoring”, *Structural Health Monitoring*, 11 (2), 173-186
19. Bai, J., Sabir, B. B., Wild, S. and Kinuthia, J. M. (2000), “Strength Development in Concrete Incorporating PFA and Metakaolin”, *Magazine of Concrete Research*, 52, 153-62.
20. Bakker. R. (1988), “Corrosion of Steel in Concrete”, *RILEM report 60-CSC*, Chapman and Hall, London, 22.
21. Behera, J.P., Sarangi, B., Nayak, B.D. and Ray, H. S. (2000), “Investigations on the Development of Blended Cements Using Activated Fly Ash”, *Indian Concrete Journal*, 74, 260–269
22. Bedekar, V., Inman, D. and Priya, S. (2008), “Detection of Corrosion Using Impedance Spectroscopy”, *Ferroelectrics letter section 35*, 7-16.
23. Bhalla. (2001), “Smart System Based Automated Heath Monitoring of Structures”, *MEngg Thesis, School of Civil and Environmental Engineering, Nanyang Technological University, Singapore*.
24. Bhalla, S. and Soh, C. K. (2003), “Structural Impedance Based Damage Diagnosis by Piezo-Transducers”, *Earthquake Engineering and Structural Dynamics*, 32 (12), 1897-1916.
25. Bhalla. (2004), “A Mechanical Impedance Approach for Structural Identification, Health Monitoring and Non-Destructive Evaluation Using Piezo-Impedance Transducers”, *PhD Thesis, School of Civil and Environmental Engineering, Nanyang Technological University, Singapore*.

-
-
26. Bhalla, S. and Soh C. K. (2004a), “Structural Health Monitoring by Piezo-Impedance Transducers. Part I Modelling”, *Journal of Aerospace Engineering, ASCE*, 17(4), 154-165.
27. Bhalla, S. and Soh, C. K. (2004b), “Structural Health Monitoring by Piezo-Impedance Transducer. Part II Application”, *Journal of Aerospace Engineering, ASCE*, 17(4), 166-171.
28. Bhalla, S., Yang, Y. W., Zhao, J. and Soh, C. K. (2005), “Structural Health Monitoring of Underground Facilities-Technological Issues and Challenges”, *Tunnelling and Underground Space Technology*, 20 (5), 487-500.
29. Bhalla, S. and Gupta, A. (2007), “A Novel Vibration Sensor for Concrete Structures”, Invention Disclosure Dt. 26th Feb 2007 (FT/IRR/CE/SB/2007/0570), Foundation for Innovation Technology and Transfer (FITT), IIT Delhi, Patent No: 1011/DEL/2011.
30. Bhalla, S., Gupta, S., Bansal, S. and Garg, A. (2009), “Ultra Low Cost Adaptation of Electro-mechanical Impedance for Structural Health Monitoring”, *Journal of Intelligent Material System and Structure*, 20, 991-999
31. Bhalla, S., Vittal, A. P. R. and Veljkovic, M. (2012), “Piezo-Impedance Transducers for Residual Fatigue Life Assessment of Bolted Steel Joints”, *Journal of Structural Health Monitoring*, 11(6), 733-750.
32. Bhalla, S. and Moharana, S. (2013), “A Refined Shear Lag Model for Adhesively Bonded Piezo-Impedance Transducers”, *Journal of Intelligent Material System and Structures*, 24 (1), 33-48.
33. Broomfield, J. P., Rodriguez, J., Ortega, L. M. and Garcia, A.M. (1993). “Corrosion Rate Measurement and Life Prediction for Reinforced Concrete Structures’.

34. Broomfield, J. P. (2007), “Corrosion of Steel in Concrete, Understanding, Investigation and Repair”, Second edition, *Taylor and Francis*.
35. Cady, P. D. and Weyers, R. E. (1983), ‘Chloride Penetration and the Deterioration of Concrete Bridge Decks”, *Cement, Concrete and Aggregates*, 5 (2), 81-87.
36. Cherrier, O., Selva, P., Budinger, V. P., Lachaud, F. and Morlier, J. (2013), “Damage Localization Map Using Electromechanical Impedance Spectrums and Inverse Distance Weighting Interpolation: Experimental Validation on Thin Composite Structures”, *Structural Health Monitoring*, 12 (4), 311-324.
37. Chen, Y., Wen, Y. and Li, P. (2004), “Characterizations of Dissipation Factors in Piezoelectric Ceramic Discs under Stress and Temperature,” *Journal of Information Acquisition*, 1(4), 213–219.
38. Claisse, P., Elsayad, H. and Ganjian, E. (1997). “Permeability and Pore Volume of Carbonated Concrete” European concerted action, *Final report, Brussels*.
39. Cook. G. (2001), “An Introduction to Piezoelectric Motors”, *EDO Electro-Ceramic Product Magazine*, Sensors.
40. Concrete Technology. (2013), retrieved 23 August www.concrete technology.org
41. Darek, B. (2012), “A Framework for Stochastic Finite Element Analysis of Reinforced Concrete Beams Affected by Reinforcement Corrosion”, *PhD Thesis, Department of Civil Engineering, University of Ottawa, Canada*.
42. Dehwah, H. A. F., Maslehuddin, M. and Austin, S. A. (2002), “Long-Term Effect of Sulphate Ions and Associated Cation Type on Chloride Induced Reinforcement

-
-
- Corrosion in Portland Cement Concretes”, *Cement and Concrete Composites*, 24, 17-25.
43. Elsener. B., Andrade. C., Gulikers. J., Polder. R. and Raupach. M. (2003), “Half-cell Potential Measurements - Potential Mapping on Reinforced Concrete Structures”, *Materials and Structures*, 36 (7), 461-471.
44. Esteban, J. (1996), “Analysis of the Sensing Region of a PZT Actuator-Sensor”, *PhD. Dissertation, Department of Mechanical Engineering, Virginia Polytechnic Institute and State University*, Blacksburg, VA.
45. Erdogdu, S., Kondratova I. L. and Bremner, T. W. (2004), “Determination of Chloride Diffusion Coefficient of Concrete Using Open Circuit Potential Measurements”, *Cement and Concrete Research*, 34 (4), 603–609.
46. Feliu. S., Gonzalez. J. A., Andrade. C. and Feliu. V. (1988), “On-Site Determination of the Polarization Resistance in a Reinforced Concrete Beam”, *NACE Corrosion*, 44, 761-765.
47. Feliu. S., González. J. A., Feliu. S (Jr). and Andrade. C. (1989), “Relationship Between Conductivity of Concrete and Corrosion of Reinforcing Bars”, *Corrosion Science*, 24, 195-198.
48. Feliu. S., González. J. A., Feliu. S (Jr). and Andrade. C. (1990), “Confinement of the Electrical Signal for In Situ Measurement of Polarization Resistance in Reinforced Concrete”, *American Concrete Institute Material*, 87 (5), 457-460.
49. Feliu. S., Gonzalez. J. A. and Andrade. C. (1994), “Errors in the On-site Measurements of Rebar Corrosion Rates Arising from Signal Un Confinement”, *American Concrete Institute*, SP (151), 183-196.

-
-
50. Financial Express. (2012), <http://www.financialexpress.com>. Oct 10, 2012.
51. Flis, J., Pickering, H. W. and Osseo-Asare, K. (1995), "Assessment of Data from Three Electrochemical Instruments for Evaluation of Reinforcement Corrosion Rates in Concrete Bridge Components," *Corrosion*, 51 (8), 602–609.
52. Feliu, S., González. J. A., Andrade. C. and Feliu S (Jr). (1998), "Equivalent Circuit for Modelling the Steel-Concrete Interface. II. Complications in Applying the Stern-Geary Equation to Corrosion Rate Determinations", *Corrosion Science*, 40(6), 995-1006.
53. Francois, R. and Arliguie, G. (1999), "Effect of Microcracking and Cracking on the Development of Corrosion in Reinforced Concrete Members", *Magazine of Concrete Research*, 51 (2), 143–150.
54. Fuhr, P. L. and Huston, D. R. (1998), "Corrosion Detection in Reinforced Concrete Roadways and Bridges via Embedded Fiber Optic Sensor", *Smart Materials and Structures*, 7, 217-228.
55. Fraay, A. L. A., Bijen, J. M. and Haan, Y. M. D. (1989), "The Reaction of Fly Ash in Concrete a Critical Examination", *Cement and Concrete Research*, 19(2), 235-246.
56. Gao, J., Wu, J., Li, J. and Zhao, X. (2011), "Monitoring of Corrosion in Reinforced Concrete Structure using Bragg Grating Sensing", *NDT &E International*, 44, 202-205.
57. Ghaz. M. P., Lagor. O. B. and Ghoda. P. (2009), "Quantitative Interpretation of Half-Cell Potential Measurements in Concrete Structures", *Journal of Materials in Civil Engineering, ASCE*, 21(9), 467-475.

-
-
58. Giurgiutiu, V. and Rogers, C. A. (1998), "Recent Advancements in the Electro-Mechanical (E/M) Impedance Method for Structural Health Monitoring and NDE", *Proceedings of SPIE Conference on Smart Structures and Integrated Systems*, SanDiego, California, March, SPIE, 3329, 536-547.
59. Giurgiutiu, V., Reynolds, A. and Rogers, C. A. (1999), "Experimental Investigation of E/M Impedance Health Monitoring for Spot-Welded Structural Joints", *Journal of Intelligent Material Systems and Structures*, 10(10), 802-812.
60. Gu, G. P., Carter, P., Beaudoin, J. J. and Arnott, M. (1996), "Validation of Half-Cell Potential Data From Bridge Decks", *Construction Repair*, 10, (3), 18-20
61. .Gu, G. P., Beaudoin, J. J. and Ramachandran, V. S. (2001), "Techniques for Corrosion Investigation in Reinforced Concrete", *Handbook of Analytical Techniques in Corrosion Science and Technology*, Noyes Publications, New Jersey, 441-504.
62. Gonzalez, J. A., Molina, A., Escudero, M. L. and Andrade, C. (1985), "Errors in the Electrochemical Evaluation of Very Small Corrosion Rates—I. Polarization Resistance Method Applied to Corrosion of Steel in Concrete", *Corrosion Science*, 25(10), 917-930.
63. Gonzalez, J. A., Feliu, S., Andrade, C. and Rodriguez, I. (1991), "On-Site Detection of Corrosion in Reinforced Concrete Structures", *Materials and Structures*, 24(5), 346-350.
64. Grantham, M. G., Herts, B. and J. Broomfield. (1997), "The Use of Linear Polarization Corrosion Rate Measurements in Aiding Rehabilitation Options for the Deck Slabs of A Reinforced Concrete Underground Car Park", *Construction and Building Materials*, 11(4), 215–224.

-
-
65. Grattan, S. K. T., Basheer, P. A. M., Taylor, S. E., Zhao, W., Sun, T. and Grattan, K. T. V. (2007), “Fibre Bragg Grating Sensors for Reinforcement Corrosion Monitoring in Civil Engineering Structures”, *American Journal of Physics*, 76, 12-18.
66. Grattan, S. K. T., Basheer, P. A. M., Taylor, S. E., Zhao, W., Sun, T. and Grattan, K. T. V. (2009), “Monitoring of Corrosion in Structural Reinforcing Bars: Performance Comparison Using In Situ Fiber-Optic and Electric Wire Strain Gauge Systems”, *IEEE Sensor Journal*, 9, 1484-1502.
67. Glass, G. K. and Buenfeld, N. R. (1997), “The Presentation of the Chloride Threshold Level for Corrosion of Steel in Concrete”, *Corrosion Science*, 39, 1001–1013.
68. Ha, T. H., Muralidharan, S., Bae, J. H., Ha, Y. C., Lee, H. G., Park, K. W. and Kim, D. K. (2007), “Accelerated Short-Term Techniques to Evaluate the Corrosion Performance of Steel in Fly Ash Blended Concrete”, *Building and Environment*, 42, 78-85.
69. Hansson, C. M. (1984), “Comments on Electrochemical Measurements of the Rate of Corrosion of Steel in Concrete”, *Cement and concrete research*, 14(4), 574-584.
70. Hansson., Jaffer, S. J., Poursea, A. (2007), “Corrosion of Reinforcing Bars in Concrete”, *Portland Cement Association*, Skokie, Illinois, USA.
71. Hari, P. K., Wahab, M. A. and Lian, K. (2012), “The Effects of Embedded Piezoelectric Fiber Composite Sensors on the Structural Integrity of Glass-Fiber-Epoxy Composite Laminate”, *Smart materials and Structures*, 21 (1), 150-160.
72. Hey, F., Bhalla, S. and Soh, C. K. (2006), “Optimized Parallel Interrogation and Protection of Piezo-Transducers in Electro-Mechanical Impedance Technique”, *Journal of Intelligent Material Systems and Structures*, 17(6), 457-468.

-
-
73. Hixon, E. L. (1988), "Mechanical Impedance Shock and Vibration Handbook", edited by C. M. Harris, 3rd edition, *Mc Graw Hill Book Co*, New York.
74. Hoar, T. P. (1967), "The Production and Breakdown of the Passivity of Metals", *Corrosion Science*, 7(6), 34-355.
75. Hussain, S. E., Rasheeduzzafar, A., Musallam, A. Al. and Gahtani A. S. Al (1995), "Factors Affecting Threshold Chloride for Reinforcement Corrosion in Concrete", *Cement and Concrete Research*, 25(7):1543-1555.
76. Ikeda, T. (1990), "Fundamentals of Piezoelectricity", *Oxford University Press*, Oxford.
77. IS: 383-1970 Indian Standard Specification for Coarse and Fine Aggregates From Natural Sources for Concrete, *Bureau of Indian Standards*, New Delhi.
78. IS 1786-1985 Indian Standard Specification for High Strength Deformed Steel Bars and Wires for Concrete Reinforcement, *Bureau of Indian Standards*, New Delhi.
79. IS: 456-2000 Indian Standard Plain and Reinforced Concrete-Code of Practice, *Bureau of Indian Standards*, New Delhi.
80. Kamada, T., Fujita, T., Hatayama, T., Arikabe, T., Murai, N., Aizawa, S. and Tohyama, K. (1997), "Active Vibration Control of Frame Structures with Smart Structures Using Piezoelectric Actuators (Vibration Control by Control of Bending Moments of Columns)", *Smart Materials and Structures*, 6, 448-456.
81. Kang, K. T., Chun, H. J., Son, J. H., Byun, J. H., Um, M. H. and Lee, S. K. (2010), "Study of Composite Plate Damages Using Embedded PZT Sensor with Various Centre Frequency", *International Journal of Modern Physics B*, 24 (15).

-
-
82. Kim, D. J., Lee, C. and Park, S. (2011), "Development of Active Sensing-Based Real-Time Concrete Strength Estimation Model", *18th International Conference on Composite Materials*, ICC Jeju, Korea.
83. Lalande, F., Childs, B., Chaudhry, Z. and Rogers, C. A. (1996), "High Frequency Impedance Analysis for NDE of Complex Precision Parts", *Conference on Smart Structures and Materials, Proceedings of SPIE* 2717:237-245.
84. Liang, C., Sun, F. P. and Rogers, C. A. (1994), "Coupled Electro-Mechanical Analysis of Adaptive Material Systems- Determination of the Actuator Power Consumption and System Energy Transfer", *Journal of Intelligent Material Systems and Structures*, 5, 12-20.
85. Lim Y. Y., Bhalla, S. and Soh, C. K. (2006), "Structural Identification and Damage Diagnosis Using Self-Sensing Piezo-Impedance Transducers," *Smart Materials and Structures*, 15(4), 987-995.
86. Lim, Y. Y. and Soh, C. K. (2012), "Effect of Varying Axial Load Under Fixed Boundary Condition on Admittance Signatures of Electromechanical Impedance Technique", *Journal of Intelligent Material Systems and Structures*, 23 (7), 815-826.
87. Mansfield, F. (1981), "Recording and Analysis of AC Impedance Data for Corrosion Studies", *Corrosion*, 37 (5), 301-307.
88. Maheswaran, T. and Sanjayan, J. G. (2004). "A Semi-Closed-Form Solution for Chloride Diffusion in Concrete with Time-Varying Parameters", *Magazine of Concrete Research*, 56 (6), 359–366.
89. Mangat, P. S. and Gurusamy, K. (1987), "Chloride Diffusion in Steel Fibre Reinforced Concrete", *Cement and Concrete Research*, 17, 385–96.

-
-
90. Manning, W. J., Plummer, A. R. and Levesley, M. C. (2000), "Vibration Control of a Flexible Beam with Integrated Actuators and Sensors", *Smart Materials and Structures*, 9(6), 932-939.
91. Milliard, S. G., Law. D., Bungey. J. H. and Cairns. J. (2001), "Environmental Influences on Linear Polarisation Corrosion Rate Measurement in Reinforced Concrete", *NDT & E international*, 34 (6), 409-417.
92. Moreno, M., Morris, W., Alvarez, M. G. and Duffo, G. S. (2004), "Corrosion of Reinforcing Steel in Simulated Concrete Pore Solutions: Effect of Carbonation and Chloride Content", *Corrosion Science*, 42(11): 2681-2699.
93. Montemor, M. F., Simoes, A. M. P., Salta, M. M. and Ferreira, M. G. S. (1993), "The Assessment of the Electrochemical Behaviour of Fly Ash Containing Concrete by Impedance Spectroscopy", *Corrosion Science*, 35(5), 1571-1578.
94. Montemor, M. F., Simoes, A. M. P. and Ferreira, M. G. S. (1998), "Analytical Characterization of the Passive Film Formed on Steel in Solutions Simulating the Concrete Interstitial Electrolyte", *Corrosion*, 54(5), 347–53.
95. Montemor, M. F. Simoes, A. M. P. and Salta, M. M. (2000), "Effect of Fly Ash on Concrete Reinforcement Corrosion Studied By EIS", *Cement and Concrete Composites*, 22, 175-185.
96. Montemor, M. F, Simoes, A. M. P. and Ferreira, M. G. S (2003), "Chloride Induced Corrosion on Reinforcing Steel: From the Fundamentals to the Monitoring Technique. *Cement and Concrete Composites*, 25,491-502.

-
-
97. Naik, T. R., Singh, S. S. and Hussain, M. W. (1994), "Permeability of Concrete Containing Large Amounts of Fly Ash", *Cement and Concrete Research*, 24, 913–922.
98. Nakamura. E., Watanabe. H., Koga. H., Nakamura, M. and Ikawa. K. (2008), "Half-Cell Potential Measurements to Assess Corrosion Risk of Reinforcement Steels in A P_c Bridge", *SACoMaTiS 2008, International RILEM Conference*, 1-2 Sept, Varenna, Como Lake, Italy.
99. Neto, R. F. N., Steffen, V., Rade, D. A., Gallo, C. A. and Palimino, L. V. (2011), "A Low-Cost Electromechanical Impedance-Based SHM Architecture for Multiplexed Piezoceramic Actuators", *Structural Health Monitoring*, 10 (4), 391-402.
100. Nguyen, C. H., Pietrzko, S. and Buetikofe, R. (2004), "The Influence of Temperature and Bonding Thickness on the Actuation of A Cantilever Beam by PZT Patches", *Smart Materials and Structures*, 13(4), 851-861.
101. Oh, B. H., Janf, S. Y. and Shin, Y. S. (2003), "Experimental Investigation of the Threshold Chloride Concentration for Corrosion Initiation in Reinforced Concrete Structures", *Magazine of concrete Research*, 55, 117-124.
102. Oh, S. J., Cook, D.C., Townsend, H.E. (1998), "Characterization of Iron Oxides Commonly Formed as Corrosion Products on Steel", *Hyperfine Interactions*, 112(1-4), 59-66
103. Parrott, L. J. (1987), "A Review of Carbonation in Reinforced Concrete", *British Cement Association*, contract report for the Building Research Establishment, C/I-0987.

-
-
104. Page, C. L., Short. N. R. and Holden. W. R. (1986), "The Influence of Different Cements on Chloride-Induced Corrosion of Reinforcing Steel", *Cement and concrete research*, 16(1), 79-86.
105. Page, C. L. (1988), "Basic Principles of Corrosion" Schiessl P. (editor), *Corrosion of steel in concrete*, Chapman and Hall, London.
106. Page, C. L., Ngala. V. T. and Page, M. M. (2000), "Corrosion Inhibitors in Concrete Repair Systems", *Magazine of Concrete Research*, 52, 25-37.
107. Panigrahi, R., Bhalla, S. and Gupta, A. (2008), "A Cost-Effective Variant of Electromechanical Impedance Technique for Structural Health Monitoring", *Experimental Techniques*, 34(2), 25-29.
108. Park, G., Kabeya, K., Cudney, H. H. and Inman, D. J. (1999), "Impedance-Based Structural Health Monitoring for Temperature Varying Applications", *JSME International Journal*, 42(2), 249-258.
109. Park, G., Cudney, H. H. and Inman, D. J. (2000a), "Impedance-based Health Monitoring of Civil Structure Components", *Journal of Infrastructure and Systems, ASCE*, 6(4), 153-160.
110. Park, G., Cudney, H. H. and Inman, D. J. (2000b), "An Integrated Health Monitoring Technique Using Structural Impedance Sensors", *Journal of Intelligent Material System and Structures*, 11, 448-455.
111. Park, G., Inman, D. J., Farrar, C. R. (2003a), "Recent Studies in Piezoelectric Impedance-Based Structural health Monitoring", *Proceedings of 4th International Workshop on Structural Health Monitoring*, edited by F. K. Chang, September 15-

-
-
- 17, Stanford University, Stanford, California, DES Tech Publications, Inc., Lancaster, PA, 1423-1430.
112. Park, G., Sohn, H., Farrar, C. R. and Inman, D. J. (2003b), "Overview of Piezoelectric Impedance-Based Health Monitoring and Path Forward", *The Shock and Vibration Digest*, 35(5), 451-463.
113. Park, S., Yun, C. B., Roh, Y. and Lee, J. J. (2005), "Health Monitoring of Steel Structures Using Impedance of Thickness Modes at PZT Patches", *Smart Structures and Systems*, 1(4), 339–53.
114. Park, S., Yun, C. B., Roh, Y., Lee, J.J. (2006), "PZT-Based Active Damage Detection Techniques for Steel Bridge Components", *Smart Structures and Systems*, (4), 957–66.
115. Park, S., Benjamin, L. G., Inman, J. and Yun, C. B. (2007), "MFC-Based Structural Health Monitoring Using a Miniaturized Impedance Measuring Chip for Corrosion Detection", *Research in Non-destructive Evaluation* 18:139-150.
116. Park, S. and Park, S. K. (2010), "Quantitative Corrosion Monitoring Using Wireless Electromechanical Impedance Measurements", *Research in Non Destructive Evaluation*, 21, 184-192.
117. Paya, J., Monzo, J., Borrachero, M. V. and Peris-Mora, E. (1995), "Mechanical Treatment of Fly Ashes—Part-I: Physicochemical Characterization of Ground Fly Ashes", *Cement and Concrete Research*, 25, 1469–1479.
118. Paya, J., Monzo, J., Borrachero, M. V., Peris-Mora, E., Gonzalez, Z. and Lope, E. (1996), "Mechanical Treatment of Fly Ashes—Part-II: Particle Morphologies in

-
-
- Ground Fly Ashes (GFA) and Workability of GFA-Cement Mortars”, *Cement and Concrete Research*, 26, 225–235.
119. Peairs, D.M., Park, G. and Inman, D. J. (2004), “Improving Accessibility of the Impedance-Based Structural Health Monitoring Method”, *Journal of Intelligent Material Systems and Structures*, 15(2), 129–139.
120. PI Ceramic, “Product Information Catalogue”, *Lindenstraße, Germany*, 2012
www.piceramic.de.
121. Pradhan, B. (2007), “Performance of TMT and CTD Steel Bars, OPC and Blended Cements against Chloride Induced Rebar Corrosion in Concrete”, *PhD Thesis, Department of Civil Engineering, IIT Delhi*.
122. Pradhan, B. and Bhattacharjee, B. (2009), “Performance Evaluation of Rebar in Chloride Contaminated Concrete by Corrosion Rate”, *Construction and Building Materials*, 23, 2346-2356.
123. Providakis, C. P., Liarakos, E. V. and Kampianakis, E. (2013), “Non-destructive Wireless Monitoring of Early-Age Concrete Strength Gain Using an Innovative Electro-mechanical Impedance Sensing System”, *Smart Materials and Research*, 932568
124. Preece, C. M., Gronvold, F. O. and Frolund, T. (1983), “Corrosion of Reinforcement in Concrete”, *construction*, Halstel, London, UK.
125. Poupard, O., Hostis, V. L., Catinaud, S. and Petre-Lazar, I. (2006), “Corrosion Damage Diagnosis of a Reinforced Concrete Beam After 40 Years Natural Exposure in Marine Environment”, *Cement and Concrete Research*, 36(3), 504-520.

-
-
126. Qin, L., Lu, Y. and Li, Z. (2010), "Embedded Cement-Based Piezoelectric Sensors for Acoustic Emission Detection in Concrete", *Journal of Materials in Civil Engineering*, 22(12), 1323-1327.
127. Qingjun, D., Jian, G., Shuguang, H., Jiaying, S. and Bingnan, S. (2009), "Different Effects of Fly Ash and Slag on Anti-Rebar Corrosion Ability of Concrete with Chloride ion", *Journal of Natural Sciences*, 14(4), 355-361.
128. Quinn, W. Kelly, G. and Barrett, J. (2012), "Development of an Embedded Wireless Sensing System for the Monitoring of Concrete", *Structural Health Monitoring*, 11 (4), 381-392.
129. Rathod, V. T, Mahapatra, D. R. (2011), "Ultrasonic Lamb Wave Based Monitoring of Corrosion Type of Damage in Plate Using A Circular Array of Piezoelectric Transducers", *NDT &E International*, 44, 628-636.
130. Rengaswamy, N. S., Chandrasekaran, S., Chandrasekaran, V., Balasubramanian, T. M. and Rajagopalan, K. S. (1981), "Corrosion Behaviour of Steel Reinforcement in Different Pozzolona Cement Concretes-Part-I-Laboratory Investigation", *Journal of the Electrochemical Society of India*, 30, 155–62.
131. Rengaswamy, N. S. (1996), "Effect of Fly Ash on Steel Reinforcement", *The Indian and Eastern Engineer*, 52, 437.
132. Rickli, J. L., Camelio, J. A. (2008), "Damage Detection in Assembly Fixtures Using Non-Destructive Electromechanical Impedance Sensors and Multivariate Statistics", *The International Journal of Advanced Manufacturing Technology*, 42(9-10), 1005-1015.

-
-
133. Samman, M. M. and Biswas, M. (1994a), "Vibration Testing for Non-Destructive Evaluation of Bridges. I: Theory", *Journal of Structural Engineering*, ASCE, 120 (1), 269-289.
134. Samman, M. M. and Biswas, M. (1994b), "Vibration Testing for Non-Destructive Evaluation of Bridges. II: Results", *Journal of Structural Engineering*, ASCE, 120 (1), 290-306.
135. Salta, M. M. (1994), "Corrosion and Corrosion Protection of Steel in Concrete", *International Conference*, University of Sheffield, UK.
136. Saraswathy, V. and Song, H. W. (2006), "Electrochemical Studies on the Corrosion Performance of Steel Embedded in Activated Fly Ash Blended Concrete", *Electrochimica Acta*, 51, 4601-4611.
137. Sakr. K. (2005), "Effect of Cement Type on the Corrosion of Reinforcing Steel Bars Exposed to Acidic Media Using Electrochemical Techniques", *Cement and Concrete Research*, 35, 1820–1826.
138. Schulz, M. J., Sundaresan, M. J., McMichael, J., Clayton, D., Sadler, R. and Nagel, B. (2003), "Piezoelectric Materials at Elevated Temperature", *Journal of Intelligent Material. Systems and Structures*, 14, 693–704.
139. Scientech Technology. (2011), retrieved 20 August from, <http://www.scientech.bz>
140. Sehgal. A., Kho, Y. Y., Osseo-Asare, K. and Pickering. H. W. (1992), "Comparison of Various Corrosion Rate Measuring Devices for Determining the Corrosion Rate of Steel-In-Concrete Systems", *Corrosion*, 48, 871-880.

-
-
141. Shanker, R., Bhalla, S. and Gupta, A. (2010), “Integration of Electro-Mechanical Impedance and Global Dynamic Technique for Improved Structural health Monitoring”, *Journal of Intelligent Material Systems and Structures*, 21(2), 285-295.
142. Shanker, R., Bhalla, S. and Gupta, A. (2011), “Dual Use of PZT Patches as Sensors in Global Dynamic and Local EMI Techniques for Structural Health Monitoring”, *Intelligent Material System and Structures*, 22, 1841-1856.
143. Sirohi, J. and Chopra, I. (2000a), “Fundamental Behaviour of Piezoceramic Sheet Actuators”, *Journal of Intelligent Material Systems and Structures*, 11(1), 47-61.
144. Sirohi, J. and Chopra, I. (2000b), “Fundamental Understanding of Piezoelectric Strain Sensors”, *Journal of Intelligent Material Systems and Structures*, 11(4), 246-257.
145. Simmers, G. E. (2005), “Impedance-Based Structural Health Monitoring to Detect Corrosion”, *MS Thesis, Department of Mechanical Engineering, Blacksburg, Virginia*.
146. Siddique, R. and Khan, M. I. (2011), “Supplementary Cementing Materials”, *Springer Heidelberg Dordrecht London New York*.
147. Soh, C. K., Tseng, K. K. H., Bhalla, S. and Gupta, A. (2000), “Performance of Smart Piezoceramic Patches in Health Monitoring of a RC Bridge”, *Smart Materials and Structures*, 9(4), 533-542.
148. Soh C. K and Bhalla S. (2005), “Calibration of Piezo-Impedance Transducers for Strength Prediction and Damage Assessment of Concrete”, *Smart Materials and Structures*, 14 (4), 671-684.

-
-
149. Song, G., Qiao, P. Z., Binienda, W. K. and Zou, G. P. (2002), "Active Vibration Damping of Composite Beam Using Smart Sensors and Actuators", *Journal of Aerospace Engineering, ASCE*, 15(3), 97-103.
150. Stern, M. and Geary, A. L. (1957), "Electrochemical polarization. I. A theoretical analysis of the shape of polarization curves", *Journal of Electrochemical society*, 104, 56-63.
151. Stratful, R. F. (1957), "The Corrosion of Steel in A Reinforced Concrete Bridge", *Corrosion*, 13, 43-48.
152. Sun, F. P., Chaudhry. Z., Rogers. C. A., Majmundar, M. and Liang, C. (1995), "Automated Real-Time Structure Health Monitoring Via Signature Pattern Recognition" *Proceedings, SPIE Conference on Smart Structures and Materials, San Diego, CA*, February 27–March 1, Vol. 2443, 236–247.
153. Thomas, M. D. A. and Matthews, J. D. (1992), "The Permeability of Fly ash Concrete", *Materials and Structures*, 25, 388-396.
154. Thomas, M. (1996), "Chloride Thresholds in Marine Concrete", *Cement and Concrete Research*, 26, 513–519.
155. Thomas, D. and Welter, J. (2004), "Corrosion Damage Detection with Piezoelectric Wafer Active Sensors", *SPIE's 11th Annual International Symposium on Smart Structures and Materials and 9th Annual International Symposium on NDE for Health Monitoring and Diagnostics*, 14-18 March 2004, San Diego, CA: 5394-2.
156. Trejo, D. and Monteiro, P. J. (2005), "Corrosion Performance of Conventional ASTM A615 and Low-Alloy ASTM A706 Reinforcing Bars Embedded in Concrete

-
-
- and Exposed to Chloride Environments”, *Cement and Concrete Research*, 35, 562–571.
157. Tuutti, K. (1982), “Corrosion of Steel in Concrete”, *CBI research report no 4.82*, Swedish *Cement and Concrete Research Institute*, Stockholm, Sweden.
158. Vedalakshmi, R., Rajagopal, K. and Palanisamy. (2008), “Enhanced Corrosion Resistance of Rebar Embedded in Fly ash Added Concrete: Role of ‘K’ factor”, *Indian Journal of Chemical Technology*, 15, 375-382.
159. Wang, A., Haskin, L. A. and Jolliff, B. L. (1998), “Characterization of Mineral Products of Oxidation and Hydration by Laser Raman Spectroscopy - Implications for In Situ Petrologic Investigation on the Surface of Mars”, *Lunar and Planetary Institute Science Conference Abstracts*, 29, 1819.
160. Wu, F. and Chang, F. K. (2006a). “Debond Detection Using Embedded Piezoelectric Elements in Reinforced Concrete Structure –Part I: Experiment”, *Structural Health Monitoring*, 5(1):5-15
161. Wu, F. and Chang, F. K. (2006b). “Debond Detection Using Embedded Piezoelectric Elements in Reinforced Concrete Structure –Part II: Analysis And Algorithm”, *Structural Health Monitoring*, 5(1):17-28.
162. Xu, B. and Giurgiutiu, V. (2005), “A Low-Cost and Field Portable Electromechanical (E/M) Impedance Analyzer for Active Structural Health Monitoring”, *Proceedings of 5th International Workshop on Structural Health Monitoring, Stanford University*, September 15–17.

-
-
163. Xu, B. and Jiang, F. (2012), "Concrete-Steel Composite Girder Bolt Loosening Monitoring Using Electromechanical Impedance Measurements", *Earth and Space*, 629-634.
164. Yan, W., Wang, J., Chen, W. Q. and Li, W. C. (2011), "Electromechanical Impedance Response of A Cracked Functionally Graded Beam With Imperfectly Bonded Piezoelectric Wafers", *Journal of Intelligent Material Systems and Structures*, 22(16), 1899-1912.
165. Yang, Y., Lim, Y. Y. and Soh, C. K. (2008), "Practical Issue Related to the Application of the Electro-Mechanical Impedance Technique in Structural Civil Health Monitoring of the Structures: II. Numerical Verification", *Smart Material and Structures*, 17(3), 1-12.
166. Yang, J., Zhu, H., Yu, J. and Wand, D. (2013), "Experimental Study on Monitoring Steel Beam Local Corrosion Based on EMI Technique", *Applied Mechanics and Materials*, 273, 623-627.
167. Zheng, Z. P., Sun, X. N. and Lei, Y. (2009), "Monitoring Corrosion of Reinforcement in Concrete Structures via Fiber Grating Sensors", *Frontiers of Mechanical Engineering China*, 4, 316-319.
168. Zheng, Z., Sun, X. and Lie, Y. (2010), "Monitoring Corrosion of Reinforcement in Concrete Structures Via Fiber Bragg Grating Sensors", *Frontier Mechanical Engineering, China*, 4 (3), 316-319.
169. Zhou, S., Liang, C. and Rogers, C. A. (1995), "Integration and Design of Piezoceramic Elements in Intelligent Structures", *Journal of Intelligent Material Systems and Structures*, 6 (6), 733-743.

-
-
170. Zhou, S. W., Liang, C. and Rogers, C. A.(1996), “An Impedance- Based System Modelling Approach for induced Strain Actuator-Driven Structures”, *Journal of Vibration and Acoustic , ASME*, 118(3), 323-331.
171. Zvica, V. (2001), “Possibility of Improvement of Potentiodynamic Method for Monitoring Corrosion Rate of Steel Reinforcement in Concrete”, *Bulletin of Materials Science*, 24 (5), 555–558.